

JCU ePrints

This file is part of the following reference:

New, Brian (2006) *Controls of copper and gold distribution in the Kucing Liar deposit, Ertsberg mining district, West Papua, Indonesia.*
PhD thesis, James Cook University.

Access to this file is available from:

<http://eprints.jcu.edu.au/2083>



5 Ore mineral distribution and metal zoning

Chapter 2 identified two primary forms of copper mineralisation; one dominated by chalcopyrite associated with skarn and magnetite-tremolite alteration and a second dominated by covellite associated with extensive quartz alteration accompanying leaching and muscovite-talc alteration of skarn and aluminosilicate rocks. While other copper-bearing minerals, namely enargite, bornite, nukundamite, digenite and chalcocite were identified, they do not occur in quantities that could be recorded alongside chalcopyrite and covellite. In addition to copper, visible molybdenite was also identified. No visible gold or gold-bearing minerals were identified, although assay data indicate that gold, as well as other trace metals are also enriched to varying degrees. PT Freeport Indonesia has established that the quantities of copper and gold contained within Kucing Liar are economically significant (see Chapter 1). The aim of this chapter is to determine the characteristics of copper and gold mineralisation in Kucing Liar with the goal of establishing the primary controls on ore deposition. The methods followed to completely portray the distribution of mineralisation are:

1. Graphical analysis of the relationships between minerals and metals
2. Modelling the spatial distribution of copper, gold and trace metals

A 13 metal assay suite was made available by Freeport Indonesia and these samples correlate with mineralogical-lithological logging data (Appendix V). Three-dimensional contours of the metal assays were constructed and are presented here in sections. The quantitative mineral database introduced in Chapter 4 is used here to constrain the metal analyses in terms of alteration and mineralisation assemblages. From these data the primary characteristics of Kucing Liar mineralisation, including the number of mineralising episodes and their metallogenic signatures can be determined.

5.1 MINERALISATION POPULATIONS AND SPATIAL DISTRIBUTIONS

The results are grouped into two sections which document firstly the large-scale distributions of mineral and metal relationships are analysed in relation to the structural setting determined in Chapter 4 followed by a more detailed examination of the data by reviewing the relationships between metals within distinct mineral associations.

5.1.1 Spatial models of ore mineral and metal distributions

Spatial models include downhole correlations, 3-dimensional wireframe objects as well as average abundances within elevation ranges in order to determine the large-scale zoning patterns of Kucing Liar. Three-dimensional models of metal distribution have been developed using Leapfrog™ (Zaparo) software, which generates iso-surfaces for a specific grade range(s) of a variable to develop a 3D contour. A selection of grade ranges has been selected for each metal. The critical sections presented here are derived from 3-dimensional wireframes that cover the entire mineralised zone and thus represent all data rather than data projected locally on the individual section planes.

Metal distributions relative to the structural setting

Local controls on mineralisation are illustrated by the nature of element dispersion pattern about the primary recognisable structures such as the Idenberg Fault Zone and the major lithostratigraphic contacts. Copper and gold occur in narrow high-grade zones within broader zones of low-level metal concentrations (Figure 5-1). Broad zones of greater than 1% Cu and 1g/t Au extend for 100-300m within single drill holes, including short sections (5-10m) of much higher grades up to 5% Cu and 5g/t Au (Figure 5-1b and c). The upper limit of mineralisation is in the middle of the Waripi limestone and is generally an abrupt transition from zero metal content, where a sandstone layer has been recognised in the sequence (see Chapter 2), while the lower boundary of copper-gold mineralisation is gradational over hundreds of metres. High-grade intervals (>2%Cu and/or >2g/tAu) up to 25m wide occur locally in these broad low-grade zones.

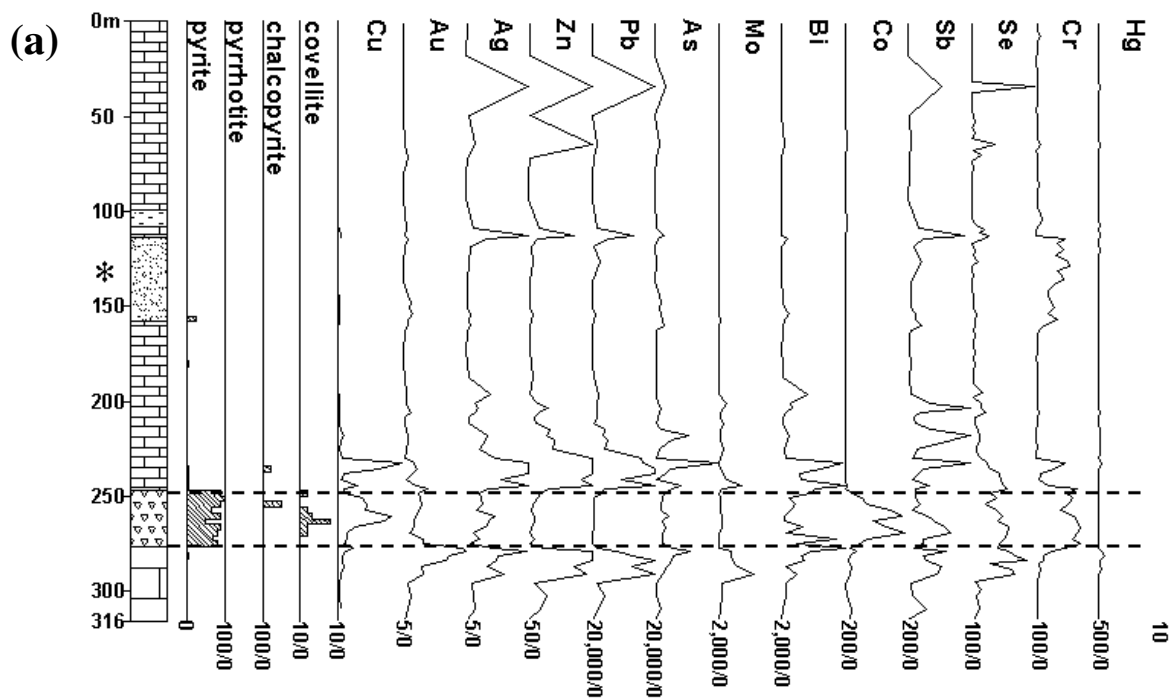
Grade distributions are commonly symmetrical though an example of systematic grade increase within the Idenberg Fault Zone is present in KL32-04 from 250-300m (Figure 5-1c).

In general, the higher copper and gold grades are coincident although there is some separation at finer scale (Figure 5-1). Lithological control on copper-gold mineralisation is demonstrated by high grades associated with the upper and lower contacts of the Ekmai limestone (Figure 5-1b). Intersections of undisturbed stratigraphy as illustrated in KL32-05 reveal narrow zones (5-10m) of high-grades concentrated at the Ekmai limestone contact surrounded by gradually decreasing lower grades. A discrete zone of mineralisation, recognised in core samples, is often present within the upper Waripi sandstone member (see KL32-05, Figure 5-1b). The very close association of high copper and gold grades and the position of the Idenberg Fault Zone demonstrate the primary control of this feature on mineralisation. Deeper intersections of the Idenberg Fault Zone, as illustrated in KL32-05, are not significantly mineralised. Copper-gold enrichment is generally symmetrical about the position of the controlling feature, though an example of asymmetric copper and gold distribution occurs in the interval from 250-300m in KL32-04 where grade progressively increases with depth at the interpreted position of the Waripi-Ekmai limestone contact (Figure 5-1c).

Sphalerite and galena are concentrated in zones directly above the main mineralised zone predominantly within unaltered Waripi limestone. Silver is closely associated with the lead and zinc enrichment. At around ~275m depth in KL32-01 (Figure 5-1a), Ag, Zn and Pb occur as a halo about the Idenberg Fault Zone where they are also associated with elevated gold that is not directly related to copper mineralisation. Ag, Zn and Pb also occur in the main orebody but their distribution is erratic. Cu, Au, Ag, Zn and Pb grades correlate closely in the Idenberg Fault Zone in a section of KL32-04 beginning at 450m, although a different association of Cu, Au, Ag, Co and Se without Zn or Pb is also present from 475m in the same structural zone (Figure 5-1c).

Figure 5-1 Downhole distribution of metal concentrations

Three structural settings are used to illustrate copper-gold enrichment patterns, including an intersection of the Idenberg Fault Zone within the upper Waripi limestone (a), an example of an intersection of relatively undisturbed stratigraphy truncated at depth by a narrow fault zone (b), and finally a complicated section of the Idenberg Fault Zone involving truncation of the Ekmai limestone (c). Dashed lines mark the upper and lower boundaries of unrecognised lithologies that are interpreted to represent fault zones. An asterisk is used to identify the location of the upper Waripi sandstone member, which is used to establish the total vertical offset. Ellipses are drawn around specific metal associations which are referred to in the text.

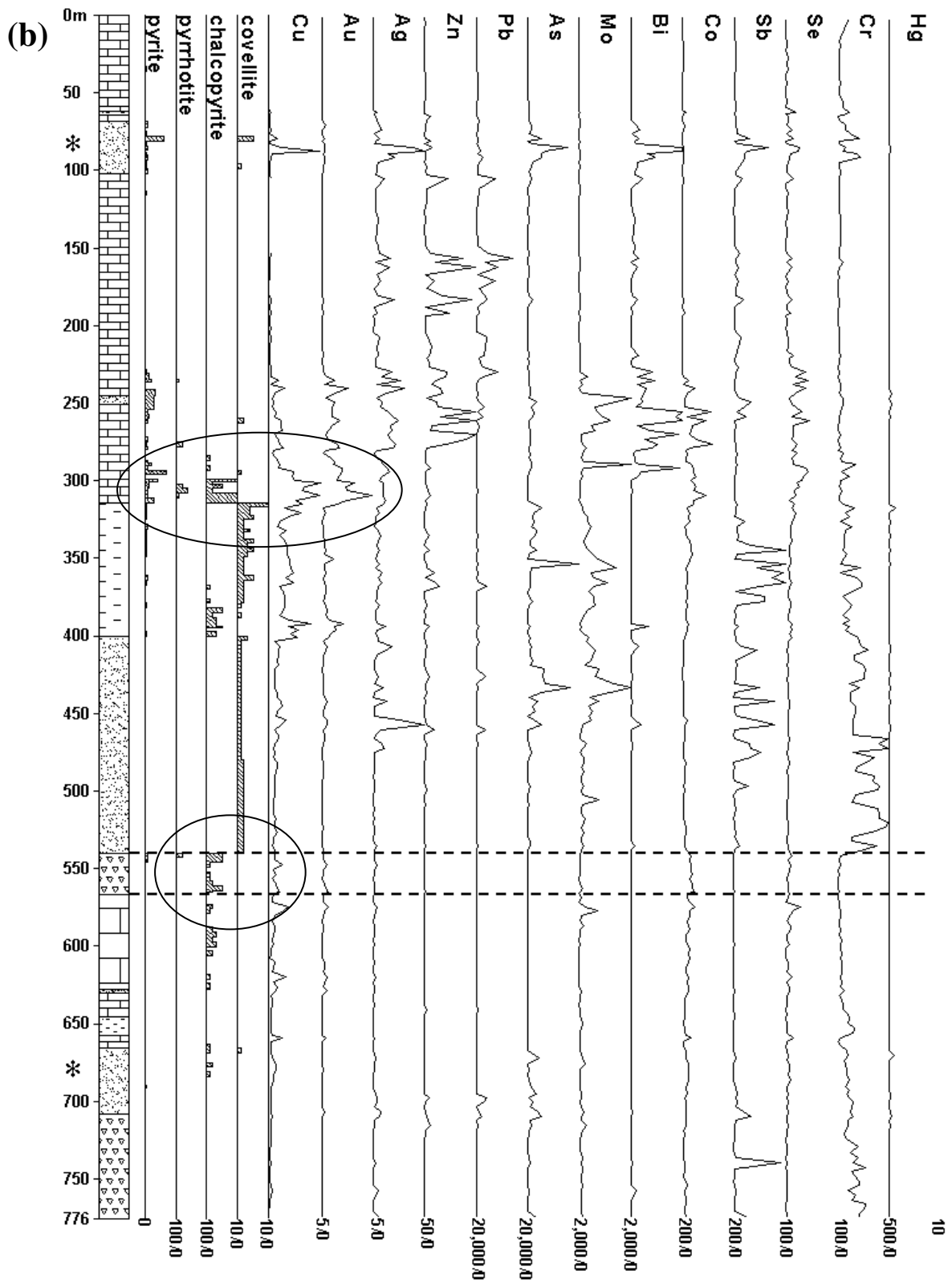


KL32-01 Idenberg Fault in relatively unaltered hosts

LITHOLOGY LEGEND

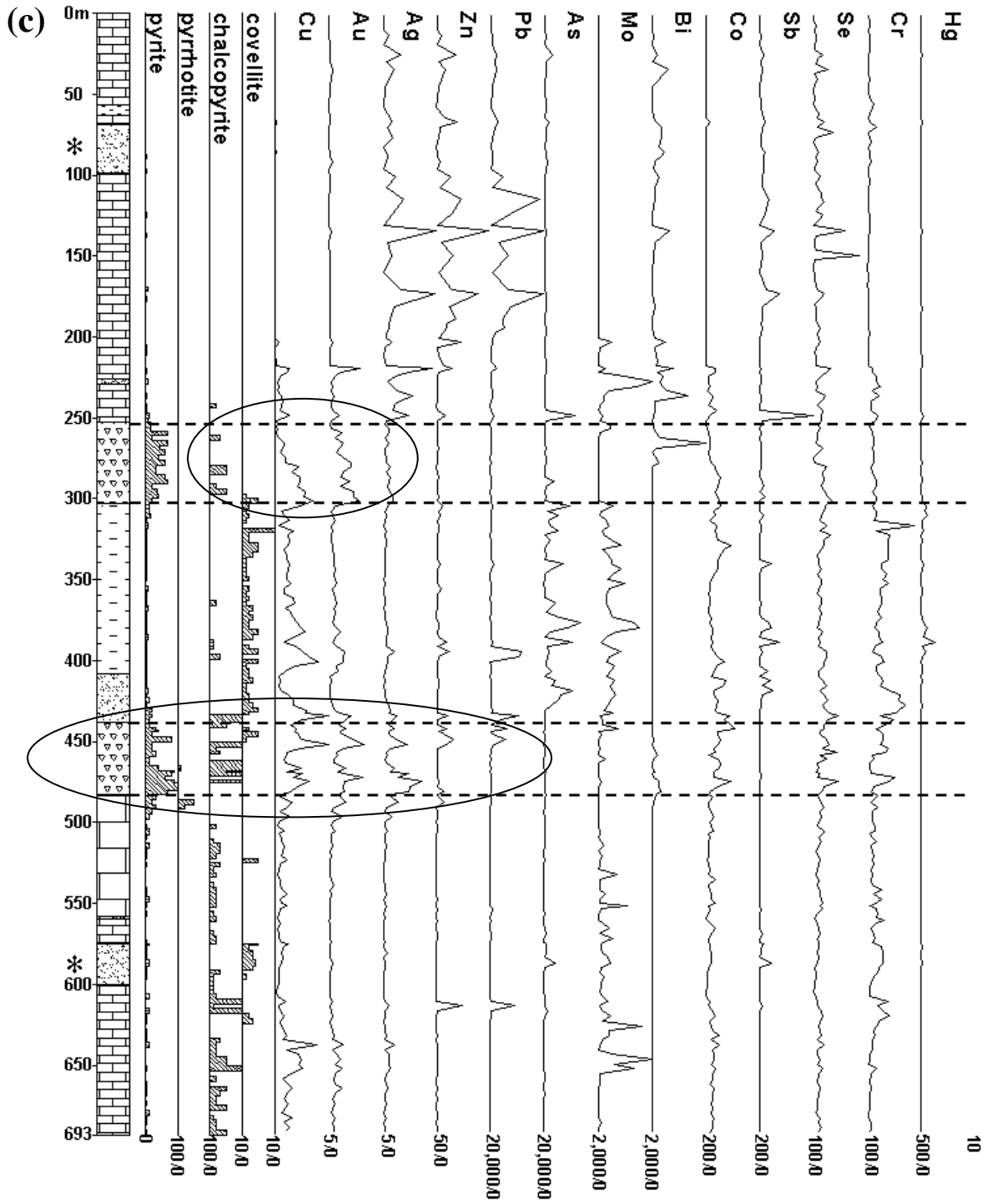
-  Faumai Limestone
-  Waripi Limestone
-  Sandstone
-  Shale
-  Fault breccia
-  Upper Waripi marker

Figure 5-1 cont.



KL32-05 Simple faulted stratigraphic sequence

Figure 5-1 cont.



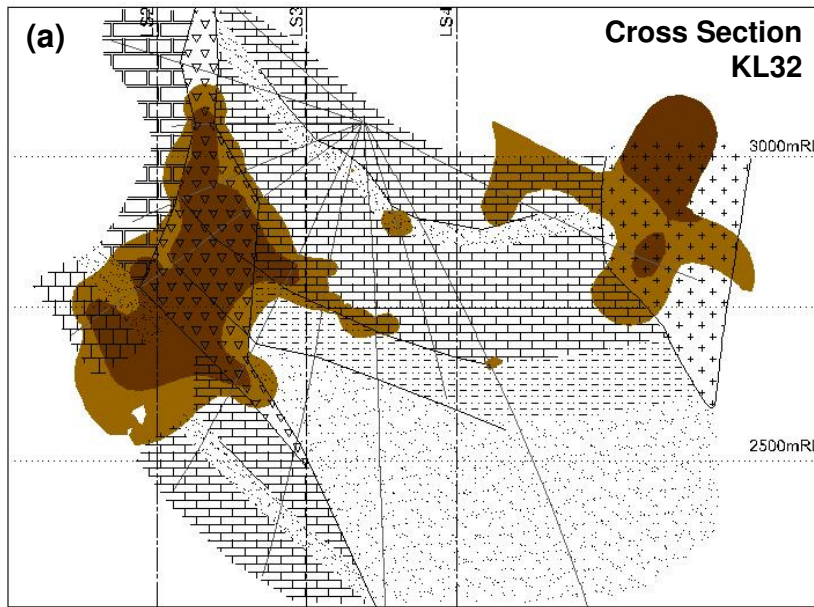
KL32-04 Complex fault and offset stratigraphy

Large-scale patterns of ore mineral and metal enrichment

The ore minerals pyrite, chalcopyrite and covellite are the only sulphides modelled, as they exist in high enough concentrations to enable data continuity between cross sections. These models indicate that pyrite is strongly restricted to the primary offset in the Idenberg Fault Zone and the Ekmai Limestone contact where it is adjacent (Figure 5-2). The distribution of chalcopyrite indicates strong partitioning along the upper Ekmai Limestone contact as well as a distinct connection between mineralisation in Kucing Liar and the Grasberg Igneous Complex (Figure 5-3). Meanwhile, covellite is strongly partitioned into the Idenberg Fault Zone offset as well as the main body of the Ekmai Limestone (Figure 5-4). The distribution of ore sulphides points to a zoning pattern of covellite-chalcopyrite centred on the Idenberg Fault Zone.

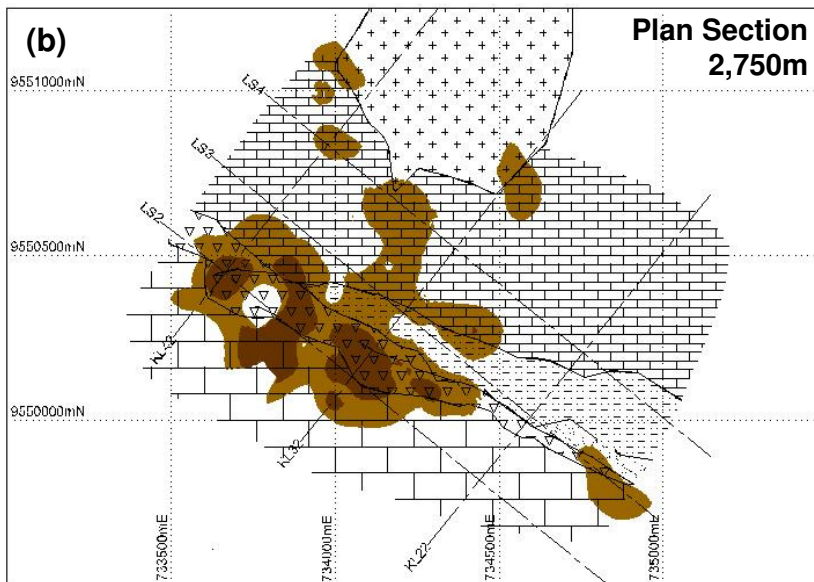
Spatial models of metal grade ranges show that metals are concentrated into major structural features, in particular the zone of offset within the Idenberg Fault Zone (IFZ) and along the lower Waripi limestone and upper and lower contacts of the Ekmai limestone where these are adjacent to the fault (Figure 5-5 to Figure 5-11). Grade patterns are symmetrical about central highly mineralised zones and there are no apparent truncations of grade continuity. Contacts between the Ekmai Limestone (Kkel) and Waripi Limestone (Tngw) adjacent to the Idenberg Fault Zone were the major conduits for metal-bearing solutions. Mineralisation is characterised by a core of copper and gold, which is surrounded by a composite halo of proximal silver and distal zinc-lead. Ag-Zn-Pb mineralisation in the halo is most concentrated at the hinge mark, which is coincident with the Idenberg Fault Zone, where there is also concentrated gold, arsenic and antimony.

Figure 5-2 Spatial distribution and structural controls of pyrite alteration



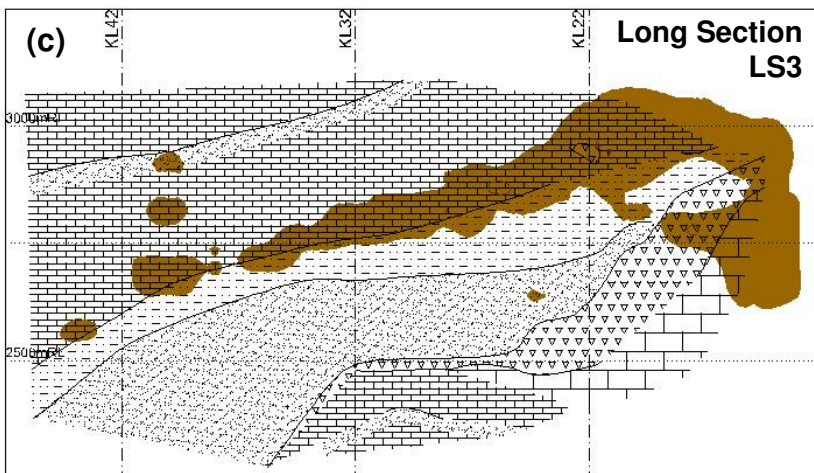
Sections of the distributions of pyrite demonstrate the strong influence of the IFZ and the adjacent Ekmai Limestone (Kkel) contact. It also indicates that intense pyrite alteration occurs within the GIC at the same elevation as Kucing Liar.

(a) A cross section through station KL32 shows intensity of pyrite in the IFZ offset as well as the extensions along the Kkel and low IFZ contacts.



(b) A plan section through 2,750m shows the most intense pyrite alteration is opposite the GIC. The section shows that pyrite is not laterally continuous across the deposit.

(c) A long section perpendicular to cross sections demonstrates that pyrite does extend along strike within the low Waripi Limestone where it is adjacent to the IFZ. The intensity of pyrite within stratigraphic layering will be dependent on the distance from the IFZ. See (a) & (b) for location.



(c) A long section perpendicular to cross sections demonstrates that pyrite does extend along strike within the low Waripi Limestone where it is adjacent to the IFZ. The intensity of pyrite within stratigraphic layering will be dependent on the distance from the IFZ. See (a) & (b) for location.

>5% pyrite
 >10% pyrite

Figure 5-3 Spatial distribution and structural controls of chalcopyrite

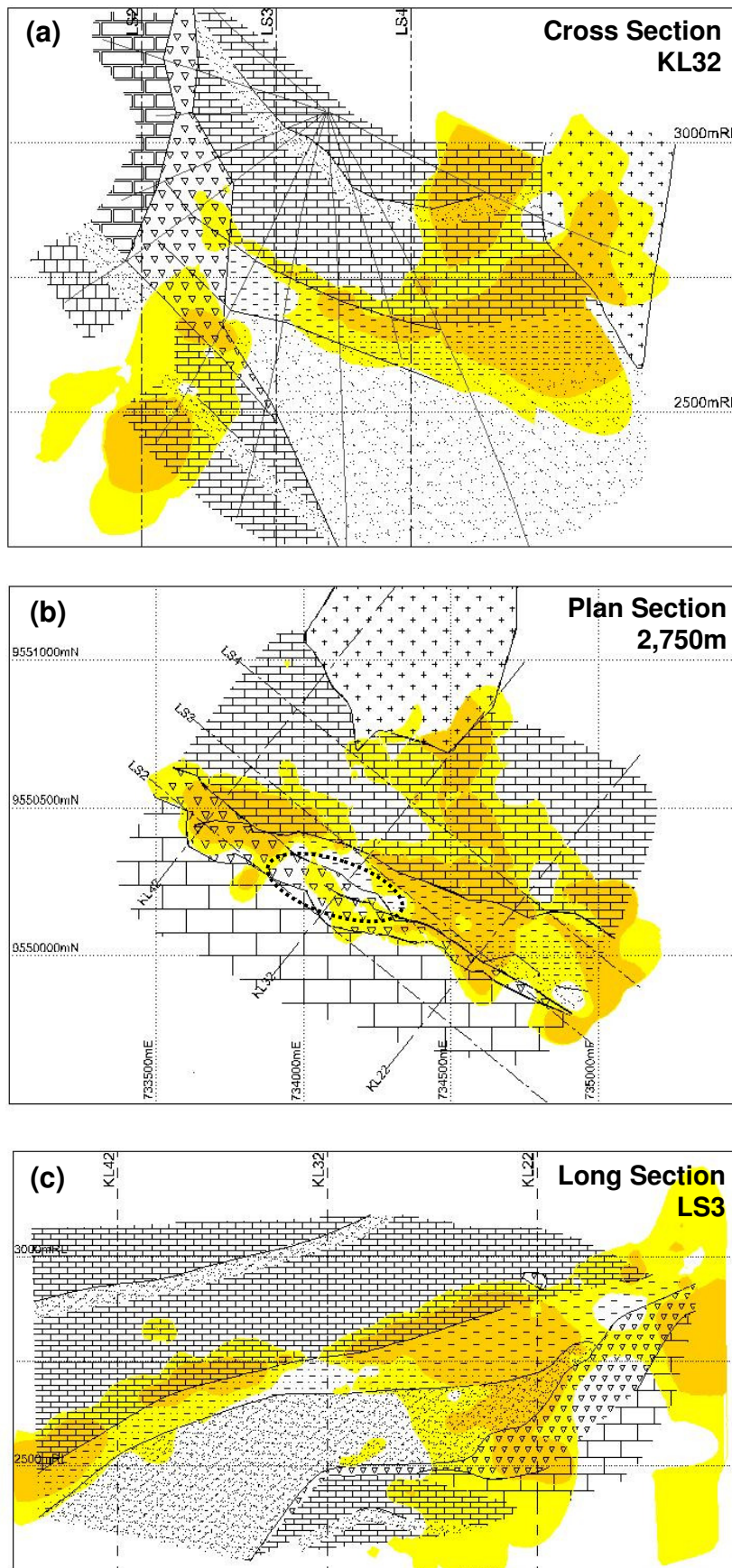
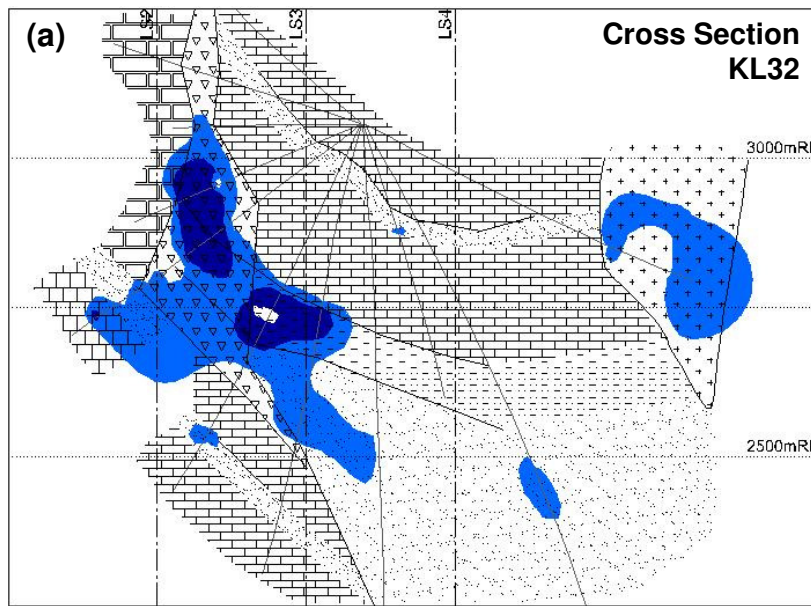
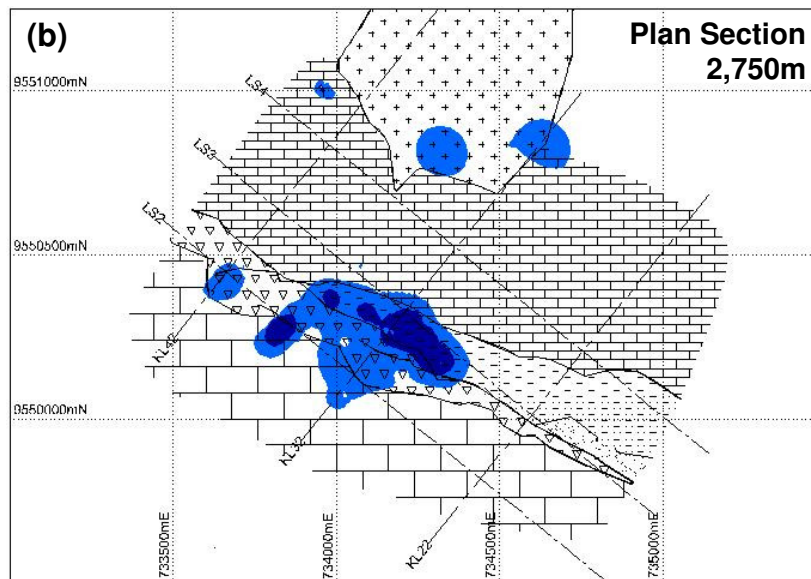


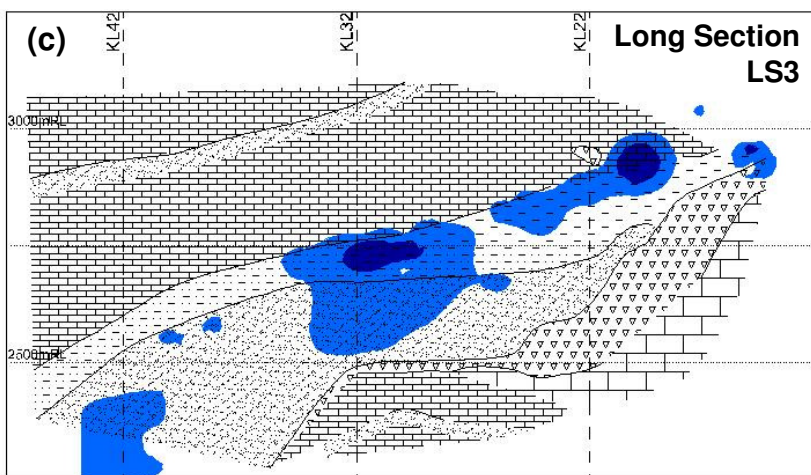
Figure 5-4 Spatial distribution and structural controls of covellite



Sections of covellite concentration models overlain on drilling traces and the lithological model described in Chapter 2. The Grasberg contact was provided by Freeport geologists. Ornamentation is same as lithological models in Chapter 4. (a) A cross section through station KL32 indicates two zones of intense covellite mineralisation within the



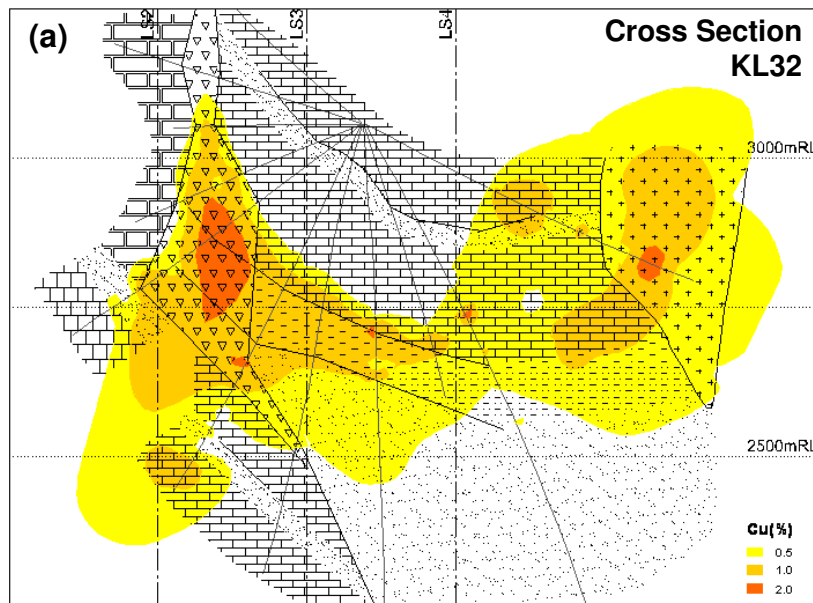
IFZ offset and within the Kkel adjacent to the IFZ. Low intensity covellite mineralisation occurs in the footwall of the IFZ along layering in the vicinity of sandstone. Note a zone of weak covellite mineralisation occurs within the GIC. (b) A plan section through 2,750m shows that covellite is also restricted along strike and appears as a core to the chalcopyrite



distributions in Figure 5-3. (c) A long section perpendicular to cross sections reinforces the concept of covellite occupying a core position relative to chalcopyrite. See (a) & (b) for location.

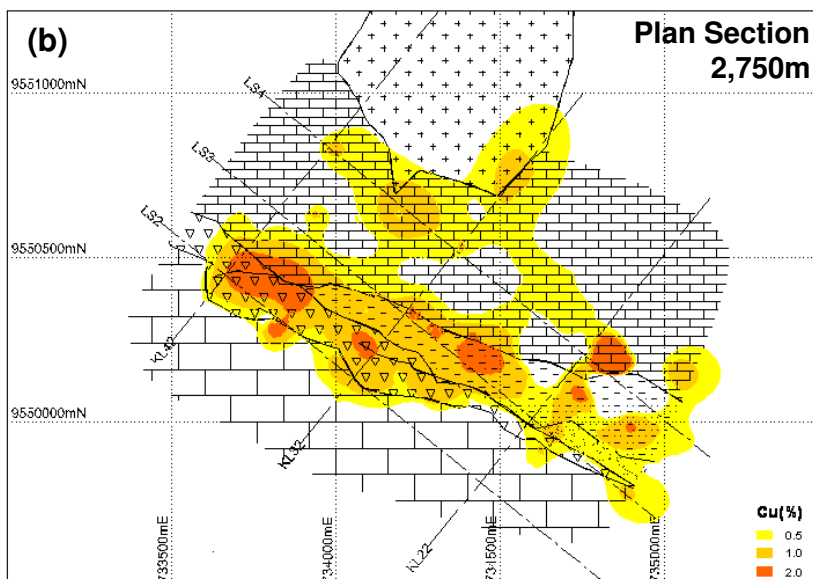
>1% covellite
 >2% covellite

Figure 5-5 Spatial distribution and structural controls of copper

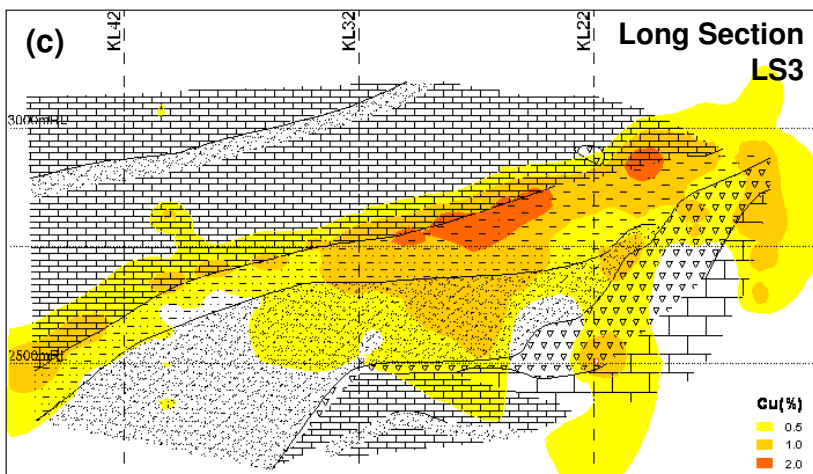


Sections of copper concentration models overlain on drilling traces and the lithological model described in Chapter 4. The Grasberg contact was provided by Freeport geologists

(a) A cross section through station KL32. The concentration of copper in the Idenberg Fault Zone and Ekmai limestone is clear. The models indicate some overlap of Cu grade between Kucing Liar and the GIC. Data is scarce in the GIC and contours of Cu-concentration in that area are poorly constrained.

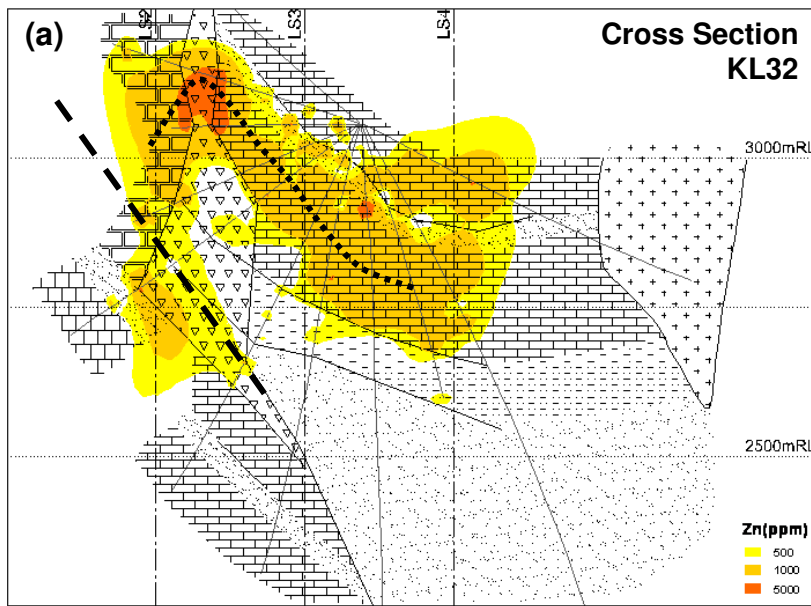


(b) A plan section through 2,750m indicates Kucing Liar Cu-mineralisation sits in the IFZ directly across from the GIC, which has a separate grade annulus about it.



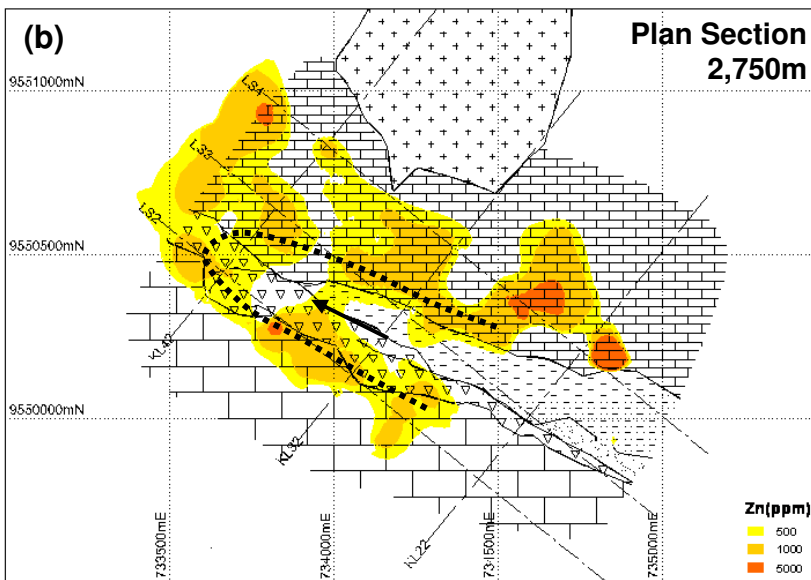
(c) A long section perpendicular to cross sections shows the strong control on Cu-grade by the Kkel-Tngw contact as well as the lateral extent of mineralisation. See (a) & (b) for location.

Figure 5-6 Spatial distribution and structural controls of zinc

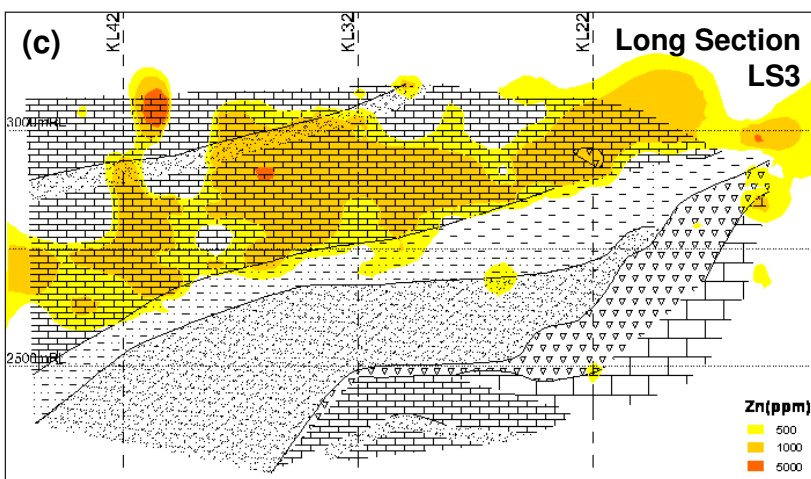


Sections of zinc concentration models overlain on drilling traces and the lithological model described in Chapter 4. The Grasberg contact was provided by Freeport geologists

(a) A cross section through station KL32 clearly shows the zinc mineralisation as a halo around the core copper-gold zone centred on, and continuous about, the Idenberg Fault Zone. The halo appears asymmetric and may be offset, as indicated by the dashed line. However, data is scarce to the left (southwest) of the IFZ.

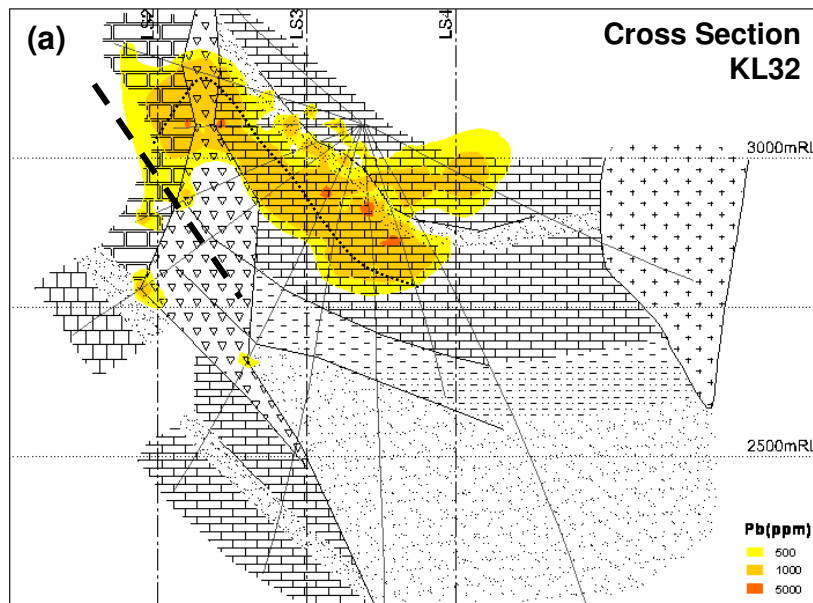


(b) A plan section through 2,750m suggests that the zinc halo plunges northwest, as indicated by the dotted line and arrow.



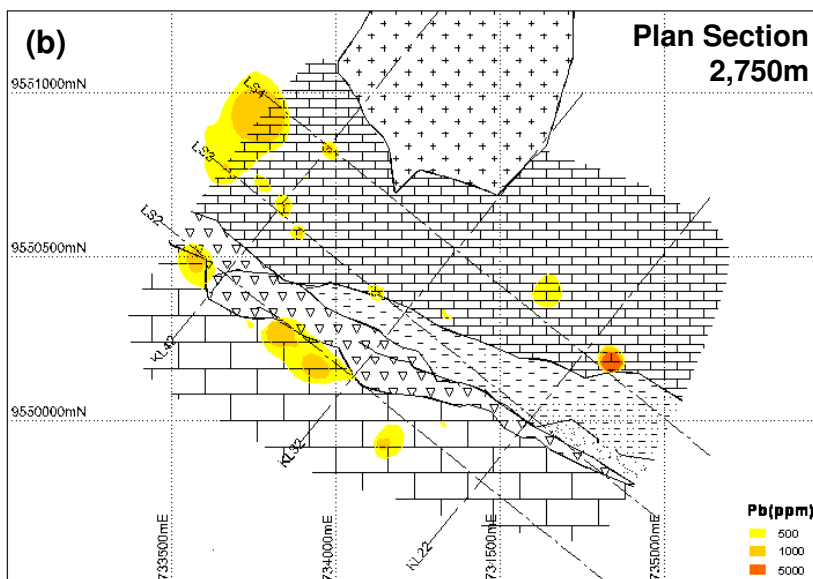
(c) A long section perpendicular to cross sections demonstrates the extent of low-grade zinc mineralisation within the Waripi Limestone as well as its continuity. See (a) & (b) for location.

Figure 5-7 Spatial distribution and structural controls of lead

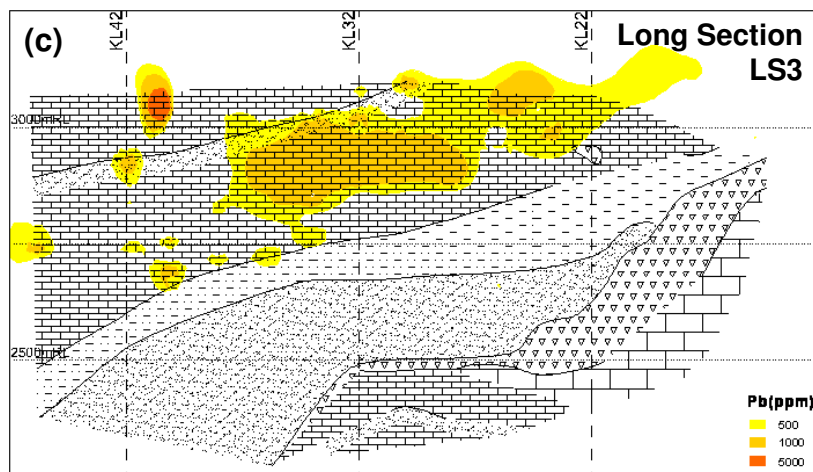


Sections of lead concentration models overlain on drilling traces and the lithological model described in Chapter 2. The Grasberg contact was provided by Freeport geologists. The distribution of Pb closely resembles that of Zn.

(a) A cross section through station KL32 highlights the same halo-like nature of Pb though it is not as concentrated as Zn. Again the halo appears asymmetric but the Pb-halo is continuous across the IFZ. There are indications that the zone of Pb-mineralisation has been truncated at the southwest side of the IFZ (dashed line).

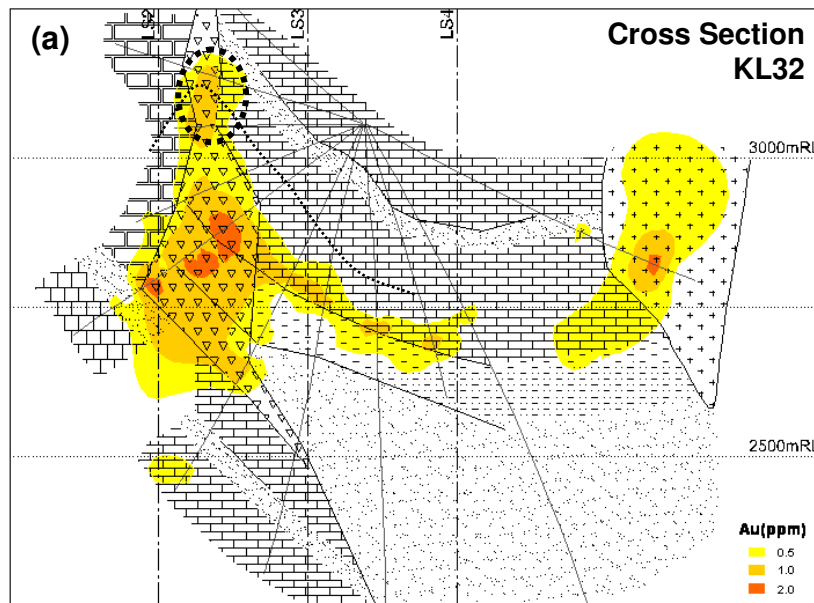


(b) A plan section through 2,750m shows that Pb does not extend down to elevations where zinc is prevalent

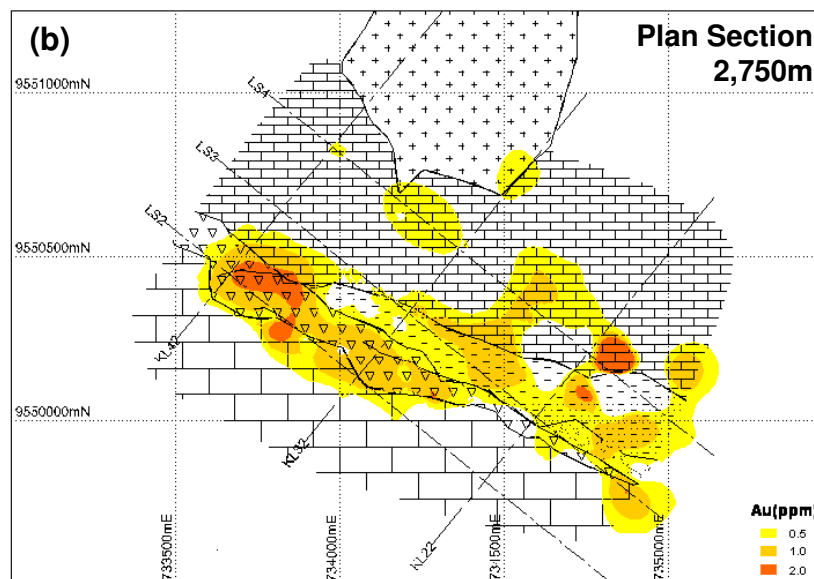


(c) A long section perpendicular to cross sections shows the same association of Pb-mineralisation within the upper Waripi limestone unit. See (a) & (b) for location.

Figure 5-8 Spatial distribution and structural controls of gold



(a) A cross section through station KL32 shows the strong control of Au within an offset in the IFZ. The effect of the Kkel-Tngw contact is also clear. A small concentration of gold (dotted circle) at the Zn-halo hinge mark (dotted line) is independent of Cu.



(c) A long section perpendicular to cross sections shows that Au-mineralisation extends the length of drilling within the lower Waripi Limestone and strongest at the eastern end of the deposit. See (a) & (b) for location of sections.

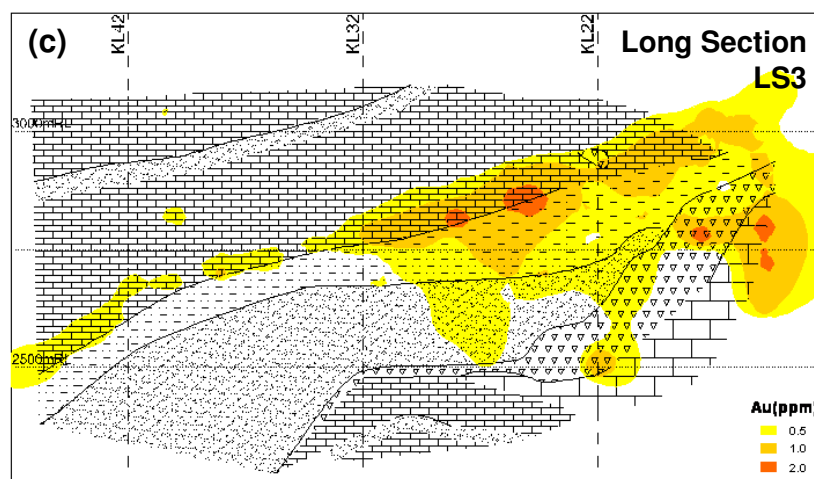
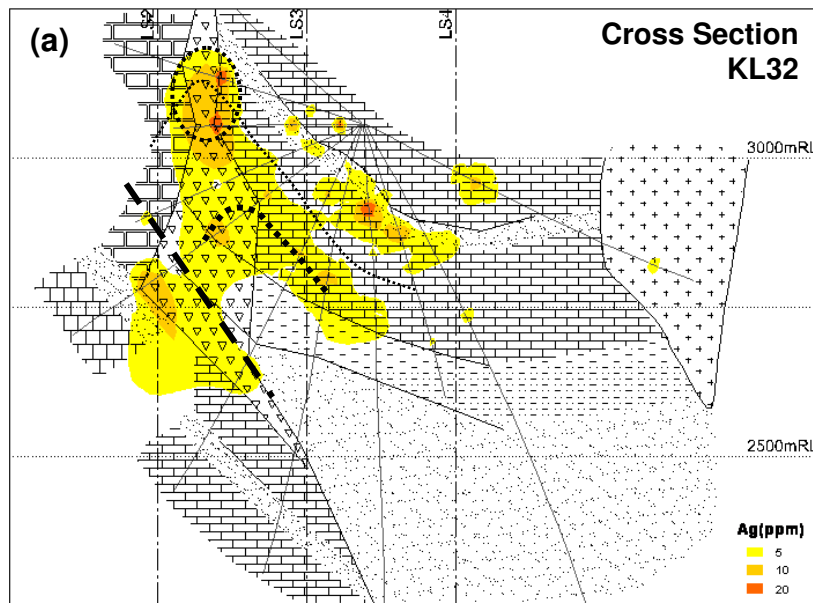
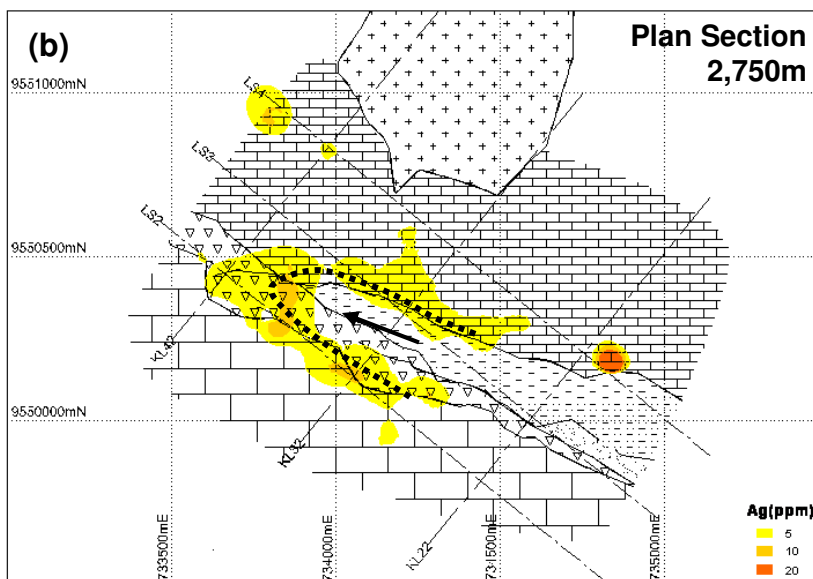


Figure 5-9 Spatial distribution and structural controls of silver

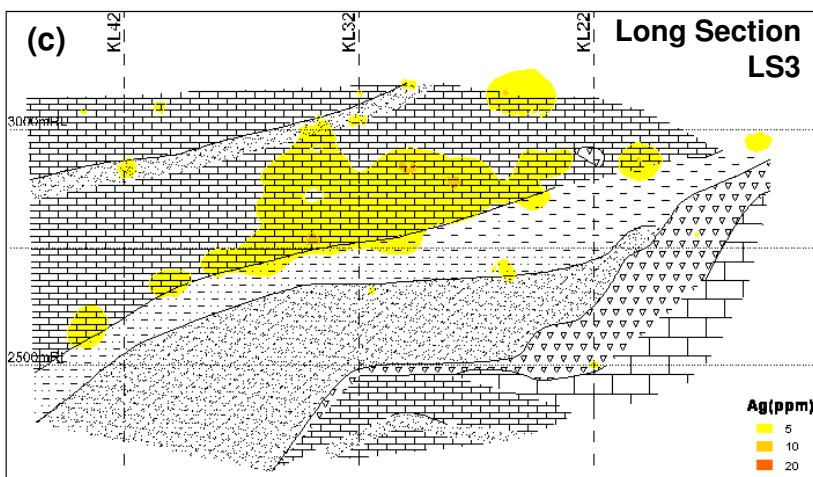


Sections of Ag concentrations are overlain on drilling traces and the lithological model described in Chapter 2. The Grasberg contact was provided by Freeport geologists. Silver concentrations share characteristics with Zn-Pb as well as Au.

(a) A cross section through station KL32 shows the same halo-like structure (bold dotted line) for Ag concentrations inboard of the Zn-Pb halo (light dotted line). The same suggestion offset at the left of the IFZ is marked (dashed line).

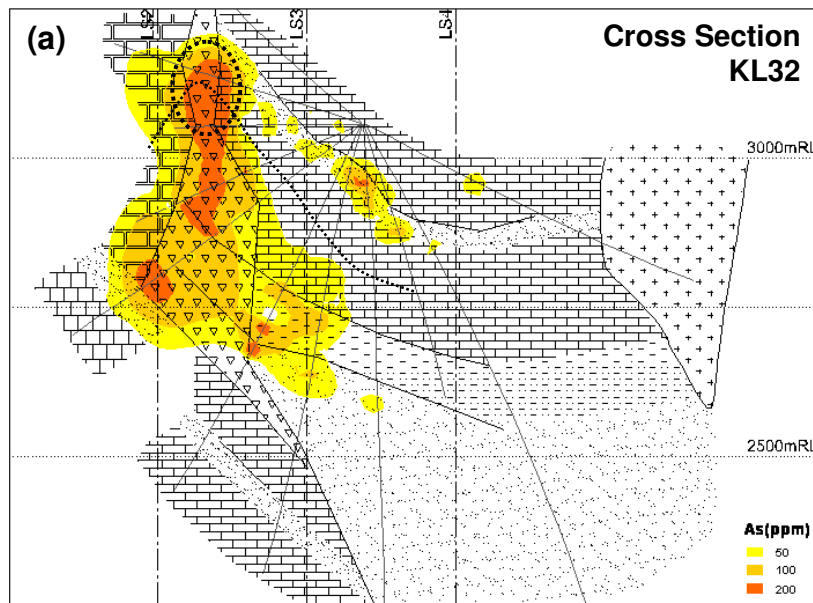


(b) A plan section through 2,750m shows the clearly defined annulus of Ag-mineralisation. The plunging attitude of mineralisation is made clear by dotted line and arrow.



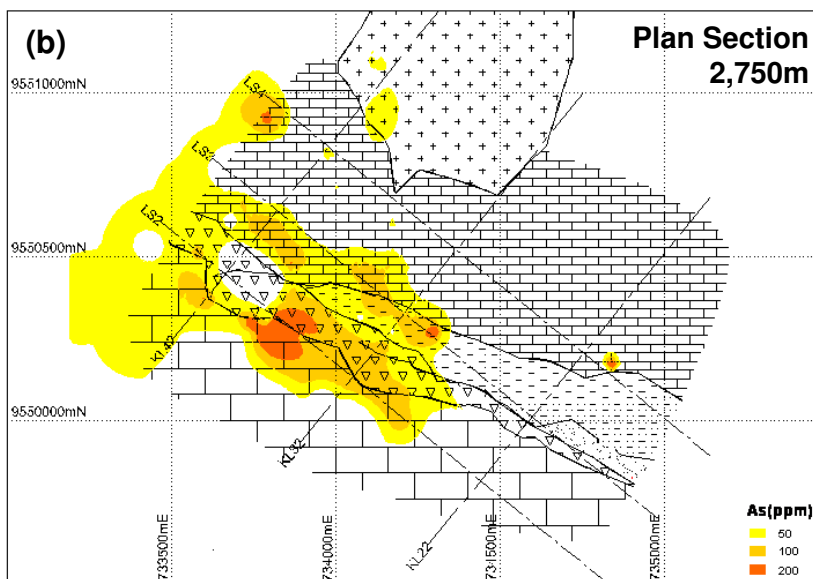
(c) A long section perpendicular to cross sections indicates that elevated silver is concentrated in the lower rather than upper Waripi limestone. See (a) & (b) for location.

Figure 5-10 Spatial distribution and structural controls of arsenic

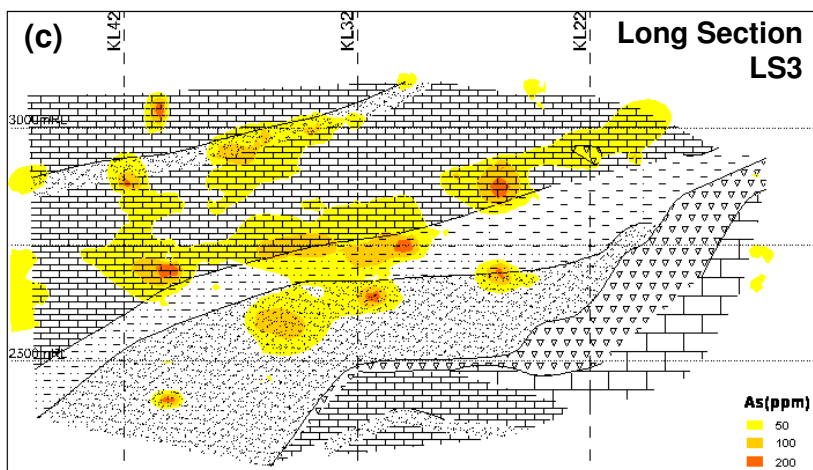


Sections of As concentrations overlain on drilling traces and the lithological model described in Chapter 2. The Grasberg contact was provided by Freeport geologists

(a) A cross section through station KL32 indicates the high elevation of As concentrations in the middle of the deposit. The circle of Au-Ag-Zn-Pb mineralisation in the Zn-Pb halo hinge has been added for comparison.

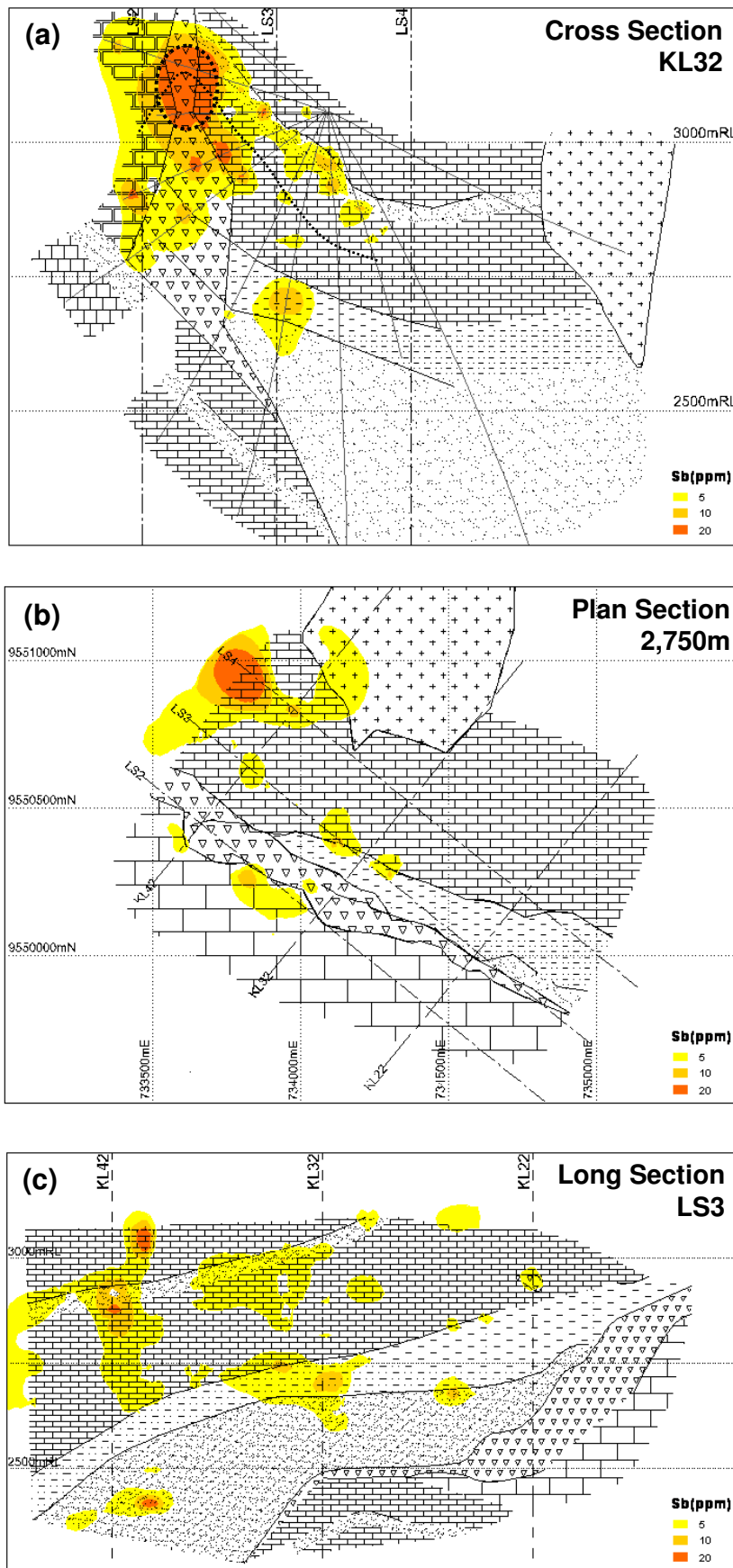


(b) A plan section through 2,750m shows that As occurs at deeper levels to the northwest end of the deposit, indicating a plunge in mineralisation zoning.



(c) A long section perpendicular to cross sections shows the concentration of As along the base of the Waripi Limestone not apparent in the cross and plan sections. However, unlike copper and gold, As is concentrated above the lower contact, close to the upper skarn contact (Chapter 4). See (a) & (b) for location.

Figure 5-11 Spatial distribution and structural controls of antimony



Elevation patterns of metals and ore minerals

Average grades for specific elevation intervals have been generated by compositing all drilling data into 20m elevation windows and plotting metal and mineral abundances against these elevations. Copper and gold are strongly correlated for much of the elevation range of Kucing Liar mineralisation except near the top of the system where gold enrichment extends beyond that of copper enrichment (Figure 5-12). Peak of gold grade (2,800m) is 100m above that for maximum copper grade (2,700m). The decrease in grade from 2,800m to 3,000m occurs over a much smaller interval (200m) than that for increasing grades from 2,200m to 2,700m. Vertical zoning patterns indicate that Cu-Au-Zn correlate in the lower half of the system while high but erratic gold higher in the system is related to equally erratic concentrations of Ag-Zn-Pb and As-Sb (Figure 5-13). Comparisons of mineralogy to metal assays demonstrate variable assemblages involving ore sulphides and gold concentrations (Figure 5-14). Elevation zoning data also demonstrate the veracity of data as the total copper concentrations closely match the average chalcopyrite + covellite abundances (Figure 5-15).

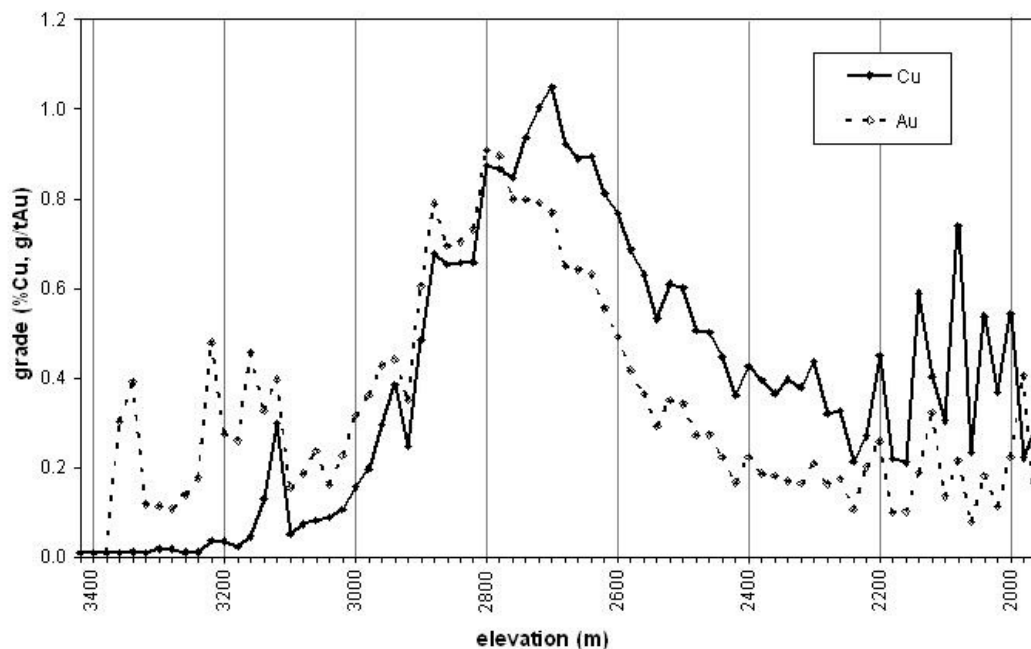


Figure 5-12 Variation of average copper and gold grades relative to elevation

Chapters 1 and 4 have demonstrated that there is no appreciable post-mineralisation tilting of stratigraphy that would affect analysis of elevation zoning in Kucing Liar.

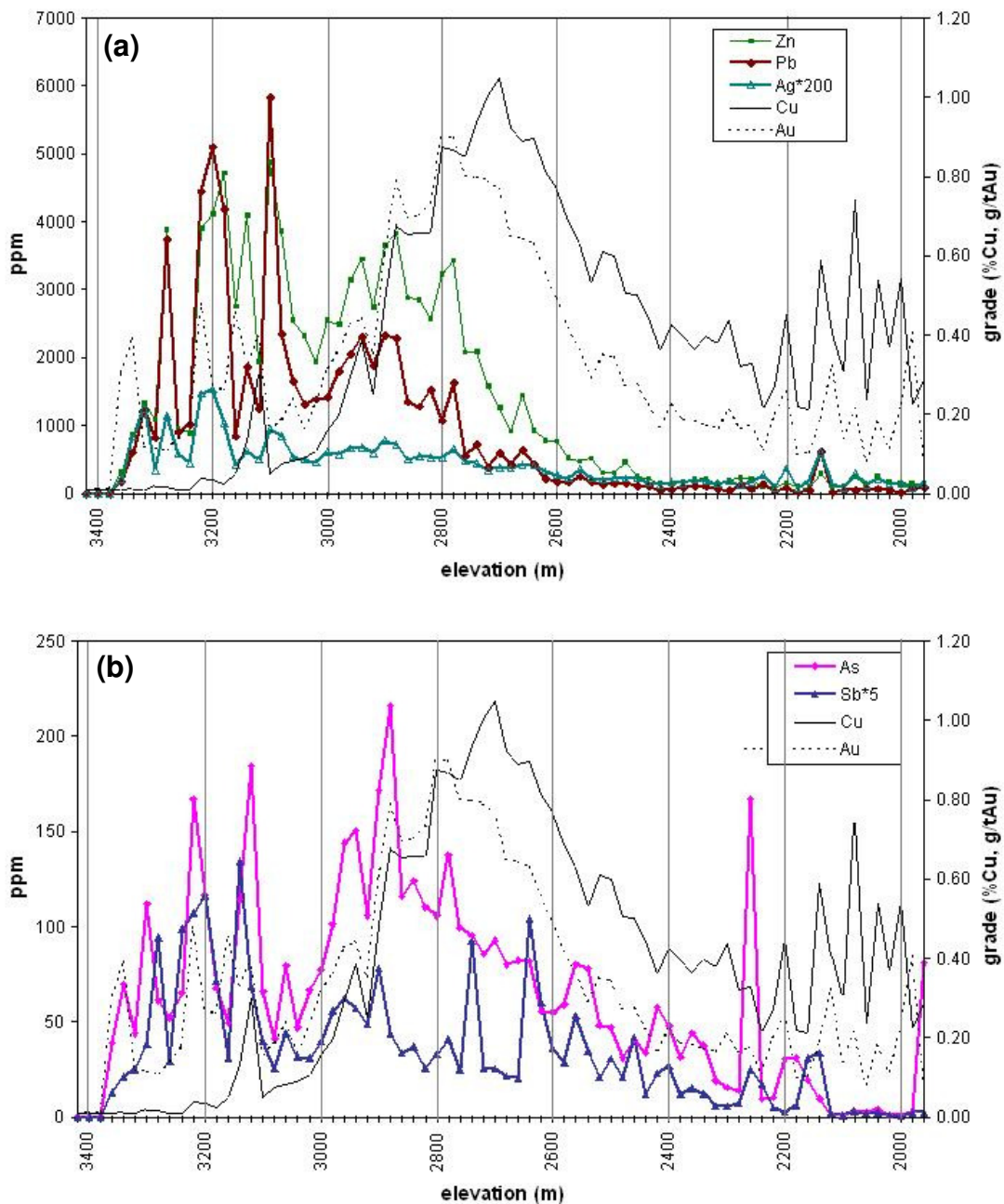


Figure 5-13 Elevation variations of Ag-Zn-Pb and As-Sb relative to Cu-Au

(a) Zinc and lead are plotted along with copper and gold to demonstrate the relationship between base metal mineralisation patterns. Although zinc and lead maxima are at higher elevations than copper and gold, the pattern of increasing grade is very similar for Pb-Zn as for Cu. An erratic zone of high Zn-Pb-Ag grades lies above 3,000m where it is associated with Cu-poor gold mineralisation. (b) A plot of As and Sb demonstrates a similar pattern of erratic high concentration above 3,000m elevation. The plot shows that As is dominant over Sb and closely correlated to Au between 2,800-3,000m, while Sb is relatively more enriched above 3,000m.

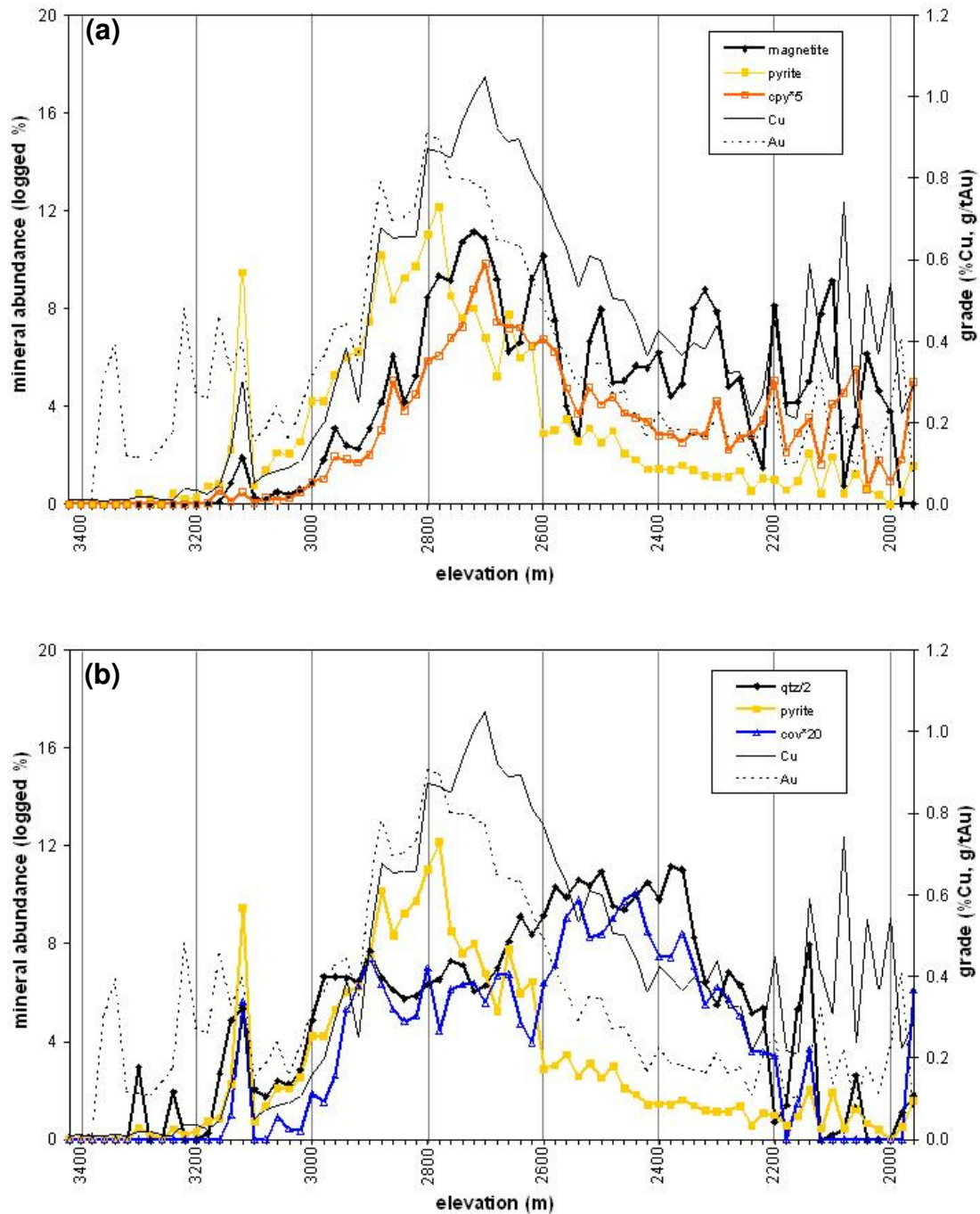


Figure 5-14 Characteristics of chalcopyrite and covellite-bearing ore relative to elevation

These two charts show the elevations variations of copper and gold relative to the main ore-bearing assemblages, namely (a) magnetite \pm chalcopyrite \pm pyrite and (b) quartz \pm covellite \pm pyrite. The two graphs show that magnetite and pyrite have unique maxima and that pyrite may accompany either chalcopyrite or covellite ore. The data show a clear correlation between magnetite and chalcopyrite and between quartz (as alteration) and covellite. The data also show that covellite is more closely associated with pyrite rather than quartz at higher elevations. The plot of pyrite and gold demonstrates that they have maximum concentrations at the same elevations, but that they are unrelated at the highest elevations in the deposit.

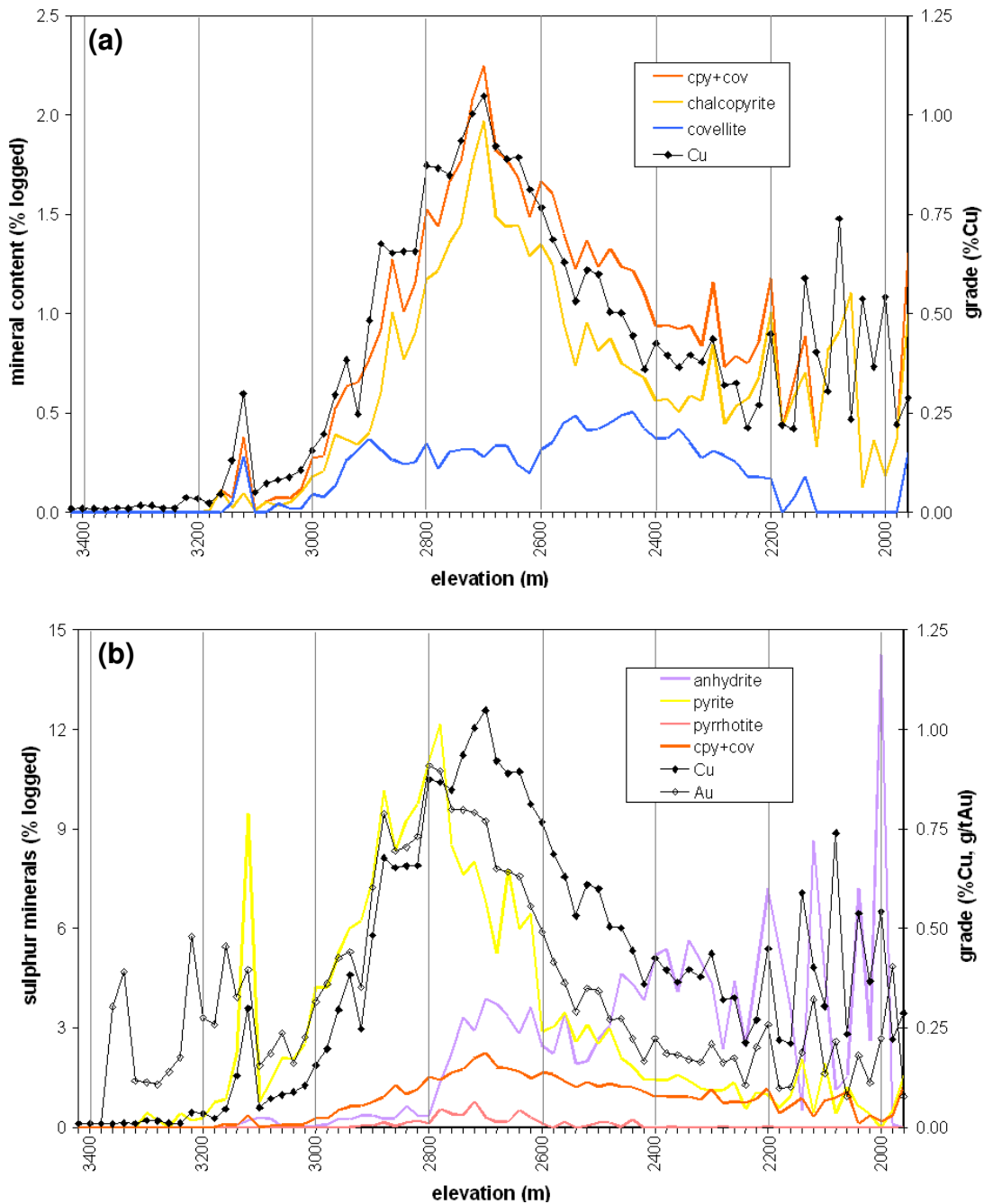


Figure 5-15 Distribution of copper, gold and sulphur phases relative to elevation

(a) A plot of average copper grades for each elevation in combination with chalcopyrite and covellite abundances demonstrates the dominant effect of chalcopyrite on grade. It also demonstrates no apparent elevation effect on covellite distribution. The sum of logged chalcopyrite and covellite matches almost exactly the pattern of copper distribution. (b) A plot of copper and gold grades alongside abundances of sulphur-bearing minerals demonstrates the very close relationship between gold and pyrite, in particular the coincidence of their maxima. The vertical zonation of anhydrite is also made clear, having an antipathetic distribution with pyrite. Mineralogical abundances have been calculated from the average abundance of each mineral type for each elevation range.

5.1.2 Inter-element associations

This section will examine the nature of Kucing Liar mineralisation in terms of the mineral forms and the associated metal suite. Variable copper and gold enrichment and the ratio of the two elements define at least two populations in the assay data. Copper and gold grades reach maximum values of approximately 10%Cu and 10g/tAu respectively and can be divided into two broad categories, a copper-rich (>0.1%) group and a copper-poor group (Figure 5-16). Both groups exhibit a similar range for gold grades, but in the copper-rich group gold grades co-vary with the copper grades, forming a single trend in grade, while for the copper-poor group there is no relationship between copper and gold grades. The co-varying population has a ratio roughly approximating $2\text{Cu}=10,000\text{Au}$, though there is a large scatter of gold grades for a specific copper grade (e.g. at 1% Cu there is a range from 0.2g/t Au to 2g/t Au). It appears that $(\text{Au} \times 10,000)/\text{Cu}$ is higher in higher grade samples, as demonstrated by the trend of covarying data points (Figure 5-16a). As the data are divided into two populations, the analysis of ore deposition will focus of high Cu (>0.1%) and low Cu (<0.1%) varieties.

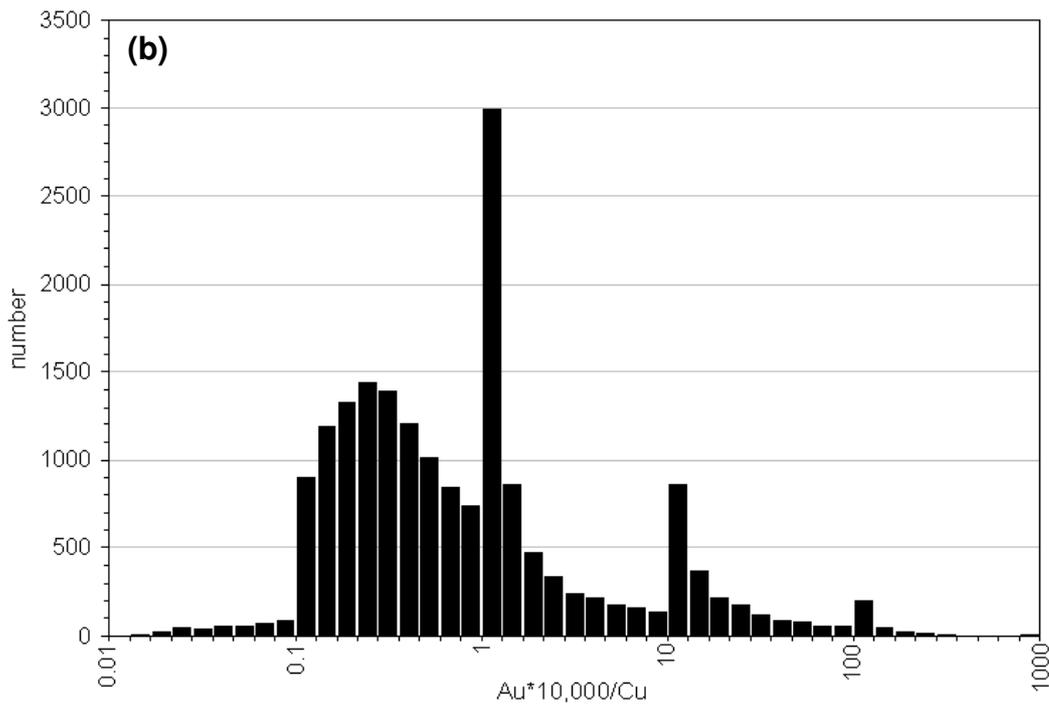
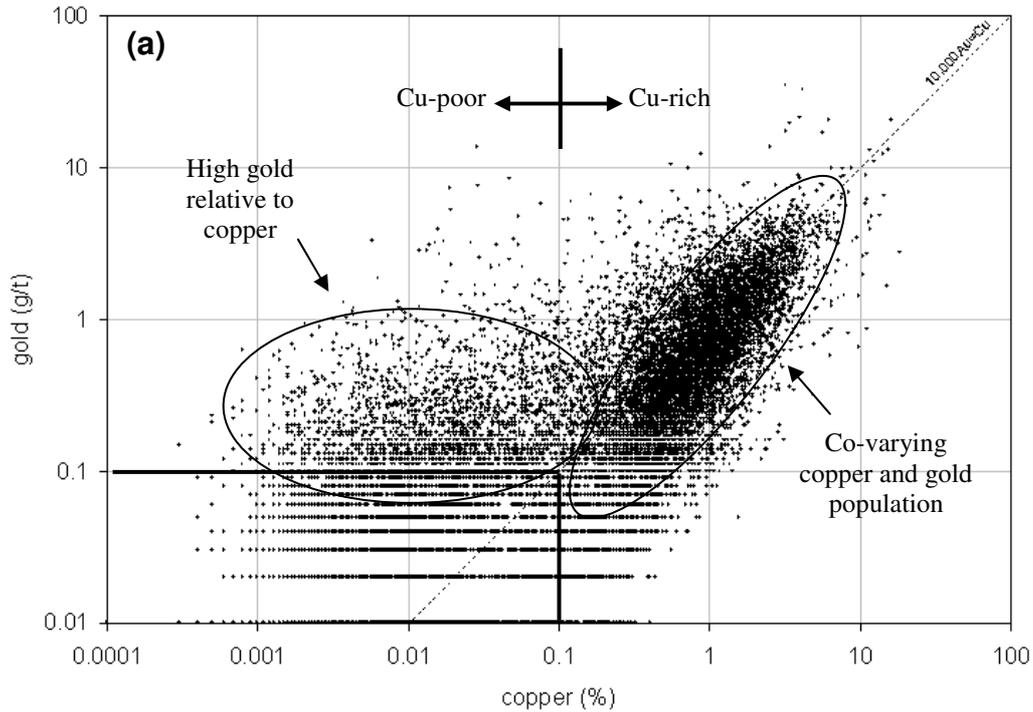


Figure 5-16 Global relationship of copper and gold

(a) Copper-gold plot for all assays ($n=27,290$) illustrating two populations of copper-rich ($>0.1\%$ Cu) and copper-poor ($<0.1\%$ Cu) samples. An ellipse drawn to represent broad trend of the data is steeper than $Au*10000=Cu$ line, indicating that the Au:Cu ratio is not constant (b) Frequency histogram of $Au*10,000/Cu$ with low-grade samples ($<0.1\%$ Cu or $<0.1\text{g/t}$ Au) extracted ($n=18,351$). The co-varying copper-gold population identified in (a) is apparent in (b) by the symmetrical distribution gold-copper ratios between 0.1 and 1 ($Au*10,000/Cu$).

Copper-gold relationships

The two main copper minerals, chalcopyrite and covellite are, in general, mutually exclusive (Chapter 3). As such, each sample interval has been characterised as either chalcopyrite- or covellite-bearing. The average grades of copper and gold for each type of mineralisation (Table 5-1) demonstrate that chalcopyrite-bearing intervals contain roughly ~1.0% more copper than covellite-bearing ones, but more importantly that the average gold grade of chalcopyrite-bearing intervals is almost twice that of those bearing covellite. There is also a third population of samples that contain no visibly identified copper-bearing sulphide. Analysis of the grade data from this group confirms that some of these intervals must have contained copper-bearing sulphides that were not identified (Figure 5-17). As a single sample was used to represent an average of 3m lengths (Appendix V), weak or sporadically-developed mineralisation may not have been represented. Furthermore, sample quality (grainsize and oxidation) may also have obscured copper minerals and overrepresentation of the “no sulphide” group (oxidation is a result of sample storage). The average copper and gold grades of the various alteration mineral assemblages indicate that the more significant ore deposition was closely related to magnetite and pyrite alteration while the remainder of the assemblages are relatively uniformly mineralised (Figure 5-18). These data also indicate that most alteration assemblages except galena-sphalerite the gold-copper ratio $Au \cdot 10,000 / Cu$ is greater than 1.

Data with low (<0.1% Cu) copper concentrations have uncorrelated gold-copper values and may represent a distinct style of gold-dominant mineralisation. This form of gold enrichment is present in most assemblages except magnetite, biotite, tremolite-actinolite and anhydrite but it is a significant component of quartz and calcite \pm magnetite alteration (Figure 5-19). Galena-sphalerite is distinct from other mineral assemblages in relation to low-Cu styles of mineralisation as it is the only assemblage dominated by this style.

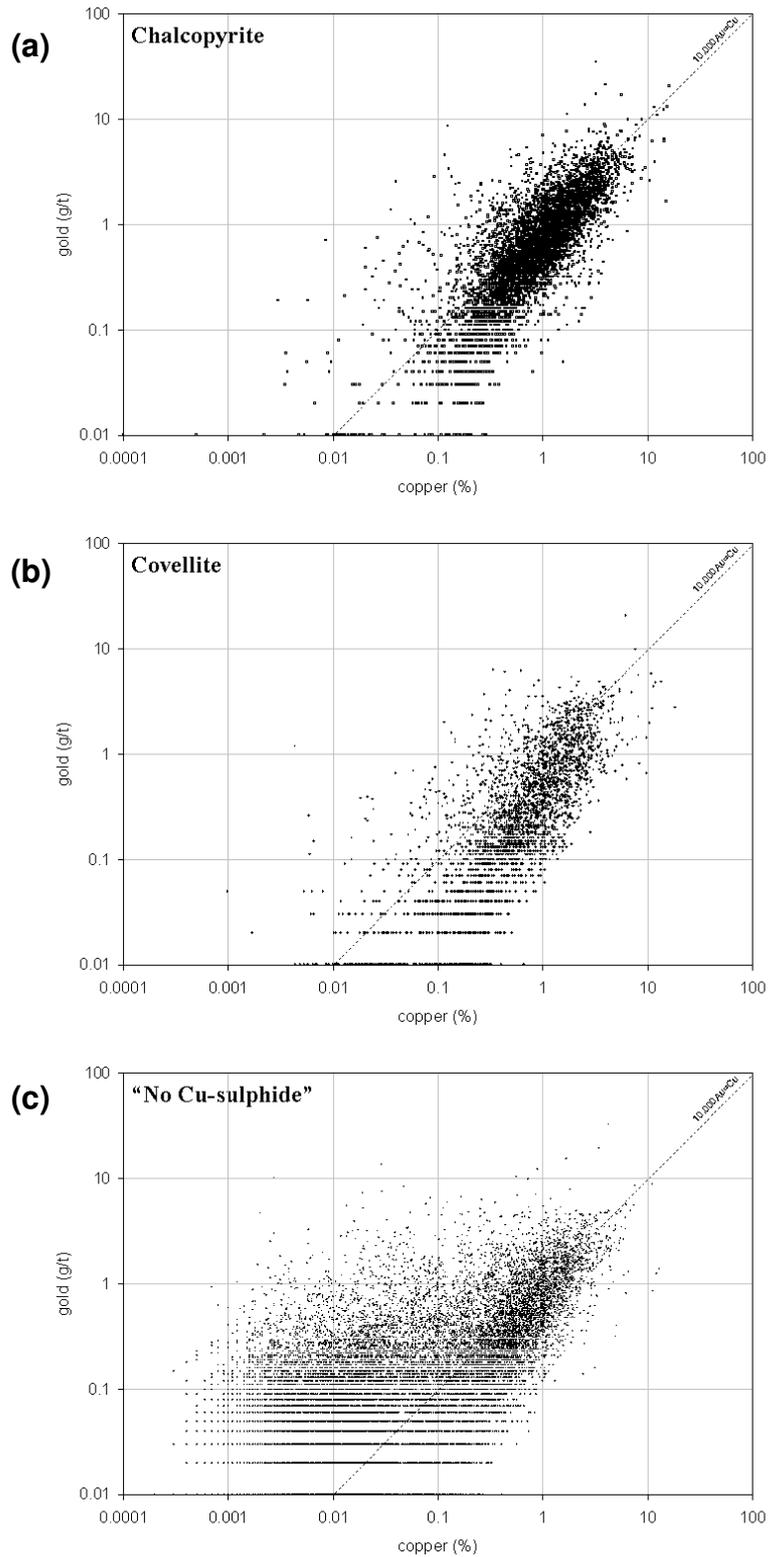


Figure 5-17 Copper and gold distributions in assay populations classified by logged copper sulphide species

The large number of samples in the "no Cu-sulphide" that have similar grade relationships to chalcopyrite and covellite distributions are believed to contain sulphide that has not been recognised. Linear regressions are, $Au(g/t) = 0.78 Cu(\%)$ and $Au(g/t) = 0.52 Cu(\%)$ for chalcopyrite- and covellite-bearing assay intervals respectively.

Table 5-1 Average grade of mineralisation in different mineral associations

	Cu (%)		Au (g/t)		number
	Av.	Std. Dev.	Av.	Std. Dev.	
Chalcopyrite	1.18	1.2	0.99	1.29	5,910
Covellite	0.99	1.1	0.59	0.87	2,868
No sulphide logged	0.42	0.67	0.56	0.89	9,666

Averages are calculated from all samples that are >0.1g/t Au or >0.1% Cu. The presence of chalcopyrite or covellite in a sample interval is usually accompanied by pervasive alteration. Low levels of copper and gold in the "No sulphide logged" (NSL) group confirm the existence of low grade or sporadic mineralisation in this sample population. Samples where no sulphide is observed and logged can be derived from sporadic mineralisation which is not preserved in the skeletal core sample collection, or from oxidation of sulphide minerals.

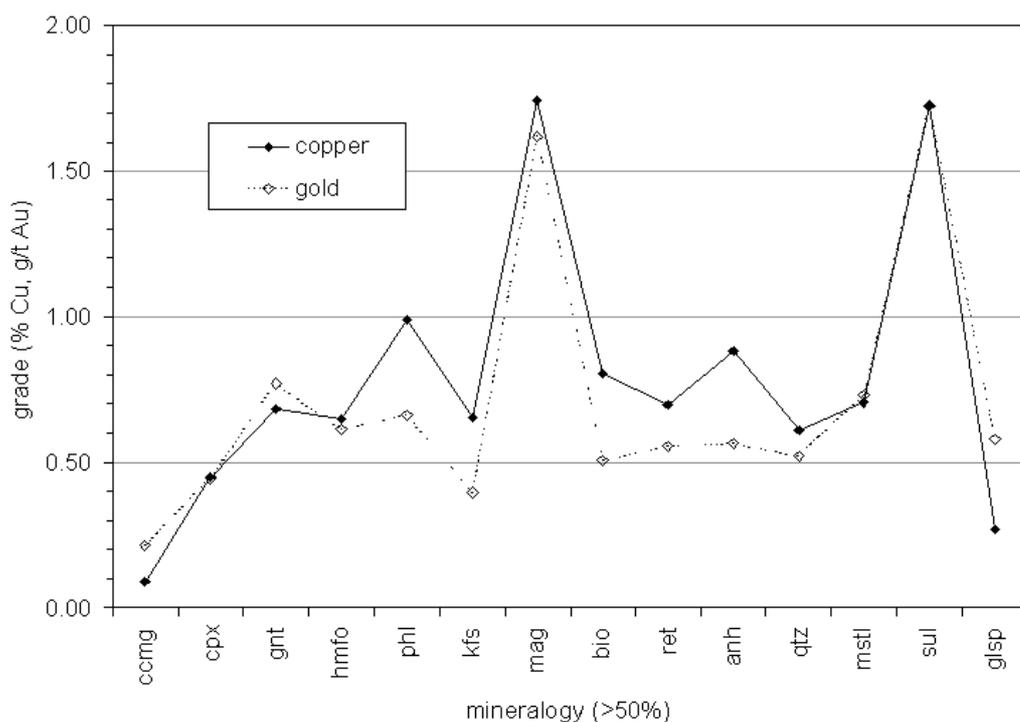
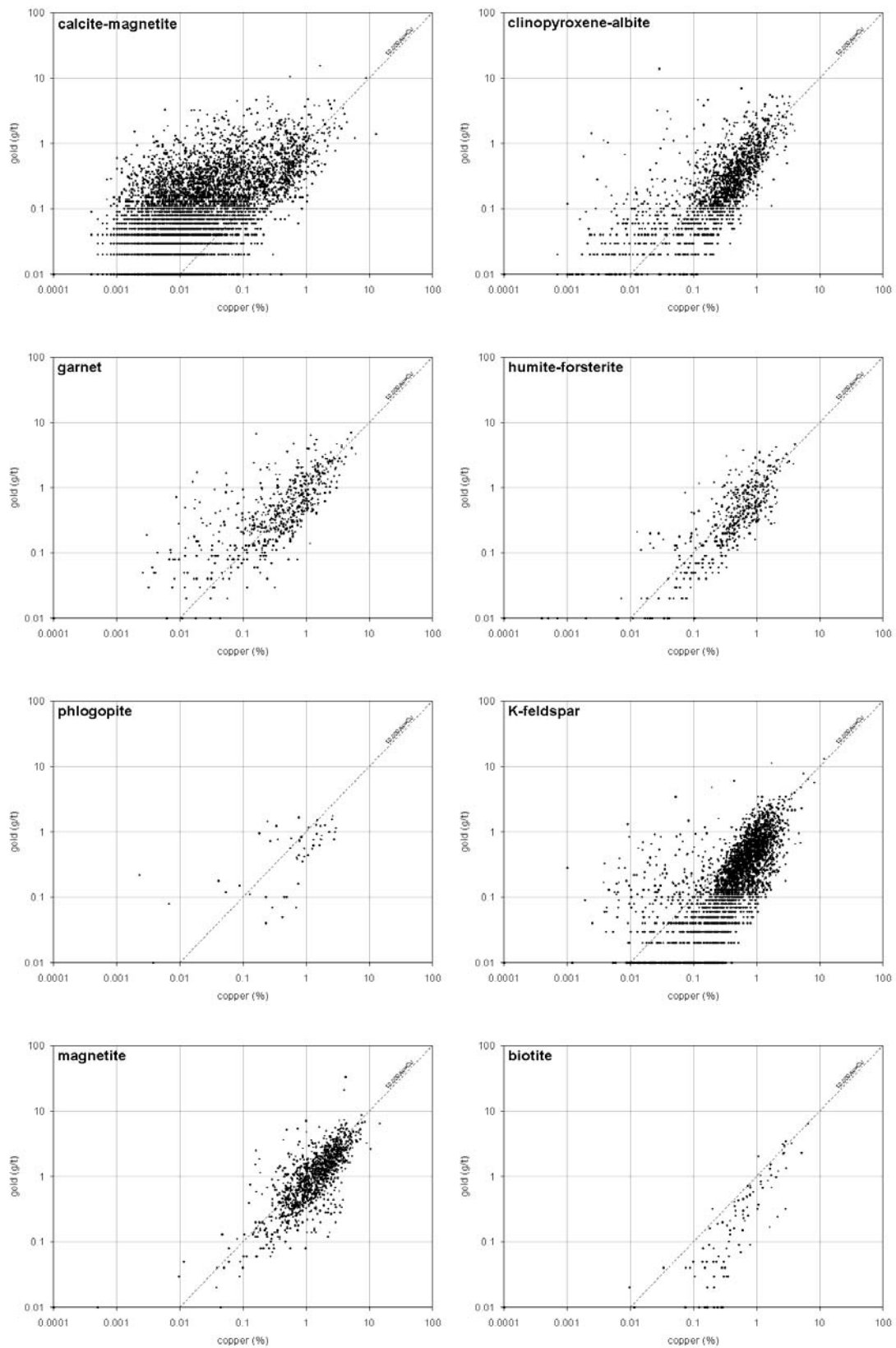


Figure 5-18 Cu-Au grades of assay intervals dominated by various paragenetic associations

Averages values have been extracted from samples containing >50% of the alteration. (anh=anhydrite, bio=biotite, ccmg=calcite ± magnetite, cpx=clinopyroxene, glsp=galena-sphalerite, gnt=garnet, hmfo=humite-forsterite, kfs=K-feldspar, mag=magnetite, msti=muscovite/talc, phl=phlogopite, qtz=quartz alteration, sul= pyrite+pyrrhotite, trsp=tremolite-serpentine).

Figure 5-19 Copper and gold grade distributions in populations classified by dominant paragenetic stage in assay interval



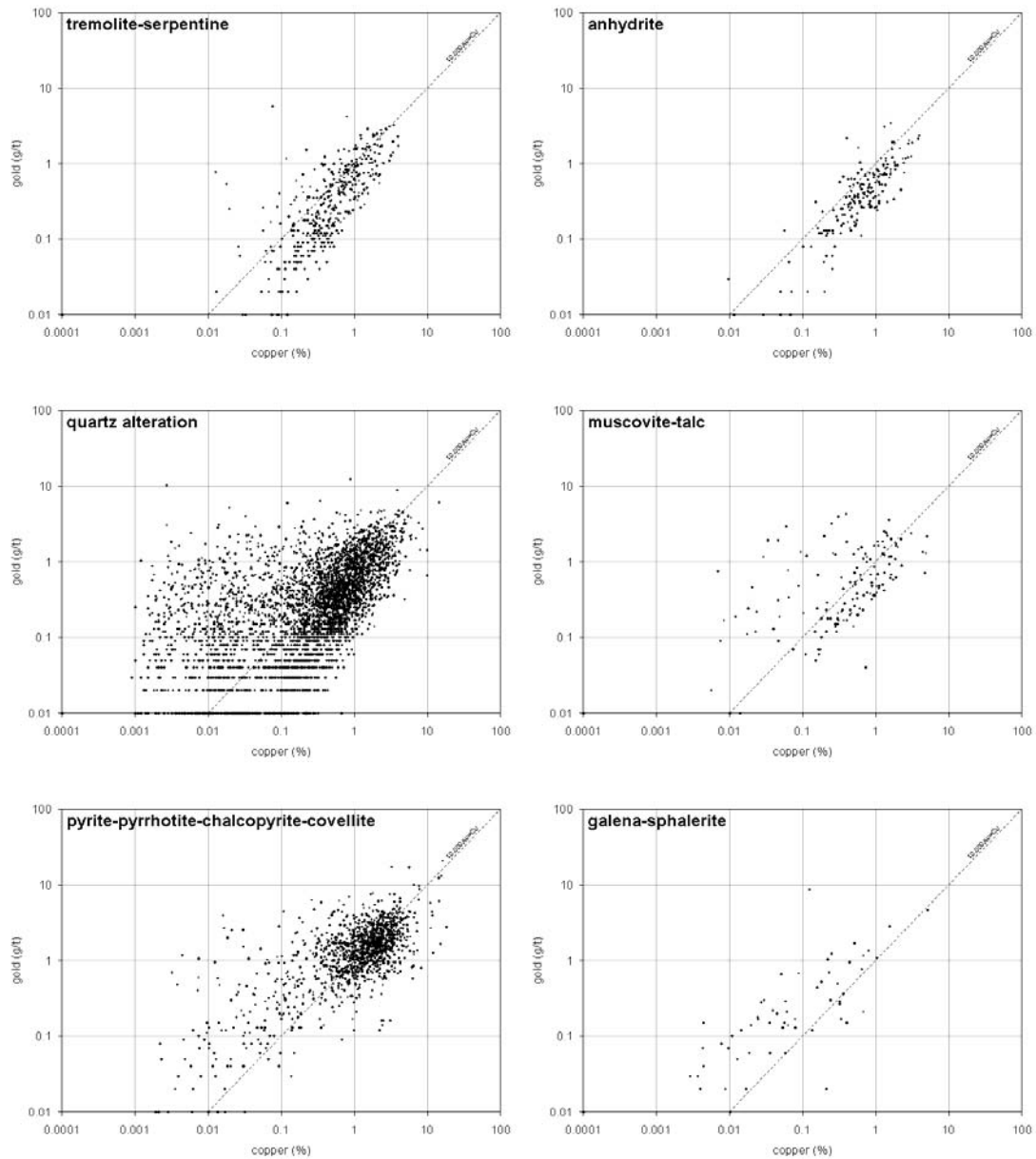


Figure 5-19 (cont.)

Each population includes assay intervals that contain more than >50% of the mineral(s) specified, normalised to 100% of total alteration. A line of $10,000\text{Au}=\text{Cu}$ is included in each plot to distinguish gold-rich and copper-rich samples. Only data from calcite \pm magnetite and the two sulphide associations plot predominantly on the gold-rich side of the graph. Garnet and pyrite-dominated intervals correlate very closely with the $10,000\text{Au}=\text{Cu}$ line, while humite-forsterite, magnetite and anhydrite have non-linear correlation of Cu-Au as indicated by a slightly steeper trend of the data than $y=x$. K-feldspar, biotite, tremolite-serpentine and quartz alteration all have steepest data trends indicating varying gold-copper ratios.

Trace metal relationships

The aim of this section is to identify the element suites that are related to high-Cu, low-Cu, chalcopyrite and covellite-dominant populations. The previous section demonstrated the relationships between copper and gold and showed that there were populations with distinct copper-gold correlations that could be identified in the dataset. Further comparisons were made between copper and gold and the remainder of the elements in the assay suite (Figure 5-20 and Figure 5-21, respectively). It is clear that the copper-rich and copper-poor segregation also holds for other metals. All metals except Co show Cu partitioned into low and high concentration groups. Further data analysis indicates that only As-Sb have very weak correlations with Au for the copper-poor mineralisation (Figure 5-21). Comparisons of average concentrations of the various metals in the different mineralisation groups defined above indicate the basic metal partitioning. Copper-rich mineralisation is enriched relative to copper-poor mineralisation in Au, Co, Mo and Cr, which only has higher average concentrations of Zn and Pb (Table 5-2). In the copper-rich ore, chalcopyrite ore is more enriched in Au, Zn and Co than covellite-bearing ore, which has higher concentrations of As, Sb, Mo and Cr.

The copper-rich population has independent Cu-Au-(Co) and Ag-Pb-Zn-Bi-(Se-Hg) associations while copper-poor mineralisation has As-Au-(Sb-Hg) and Pb-Zn-Ag-(Sb-Se) associations (Figure 5-22). The chalcopyrite-dominant population has Cu-Au-Co and Ag-Pb-Zn-(Se-Sb) where Sb is associated with precious metal and base metal mineralisation. The brackets indicate lower correlation coefficients. Chalcopyrite-dominant ores are characterised by Cu-Au-(Co) with weak associations of Ag-Pb-Se-Hg-Bi-(Zn) while covellite-dominant ores are defined by associations of Cu-Au-(Co-Se), Ag-Pb-Zn-Bi-(Hg) and As-Sb-Hg-(Ag). Mercury is associated with base metal mineralisation in high-Cu populations but is associated with Au-As in the low-Cu population. This indicates that the primary copper association is Cu-Au-Co while base metal mineralisation is an association of Zn-Pb-Ag plus Bi-Sb-Se. A third association defined in the copper-poor population is Au-As-(Sb-Hg).

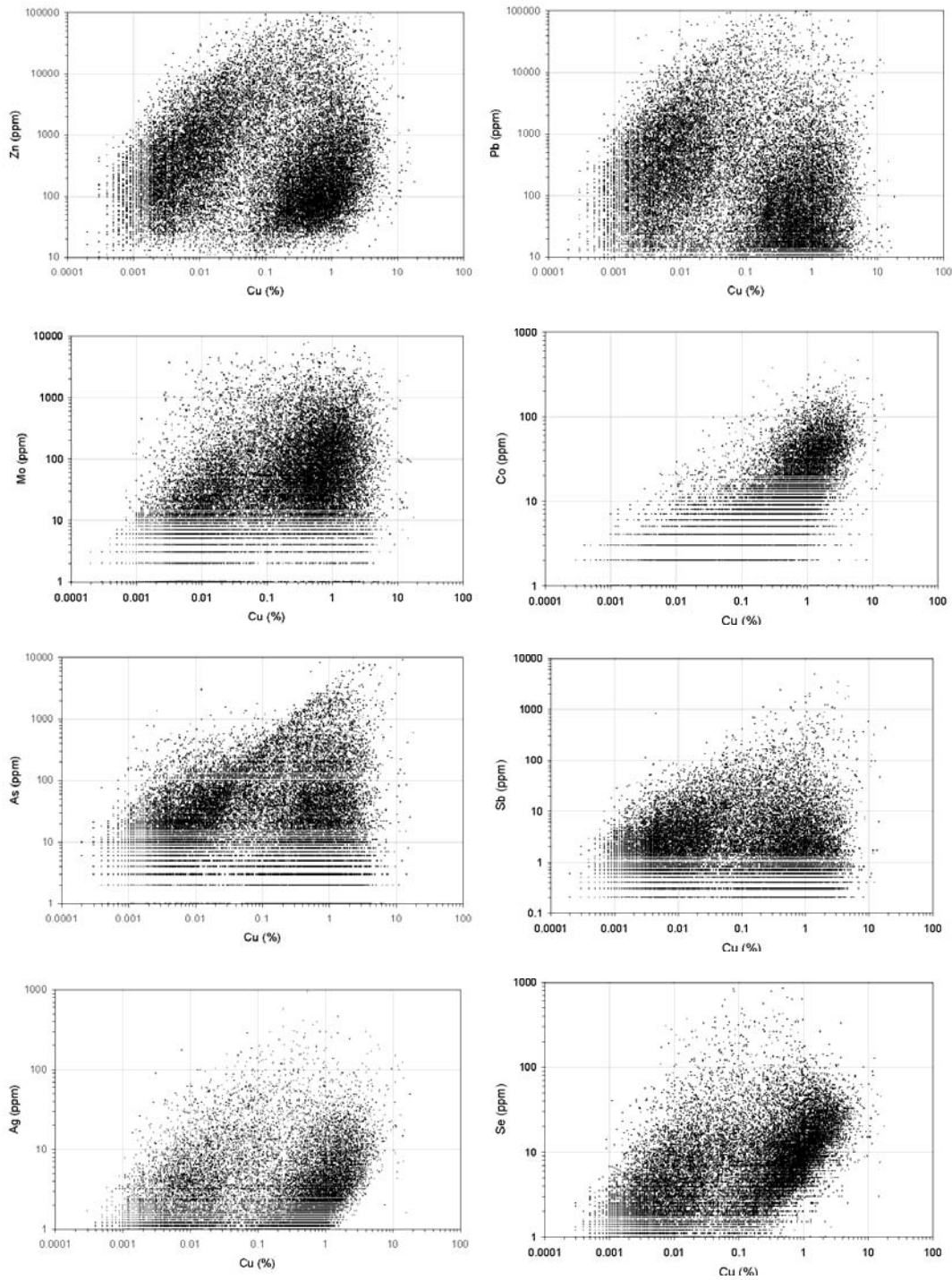


Figure 5-20 Minor element variations with respect to copper

The plots illustrate bimodal distributions of the ratios of copper to other elements. The graphs show that all of the metals except cobalt are divided into high and low copper groups the same as for gold. They also indicate that the average metal grade in low-copper populations is higher for Zn, Pb, and Sb and higher in the high-copper population for Mo, Ag, and Se (see Table 5-2).

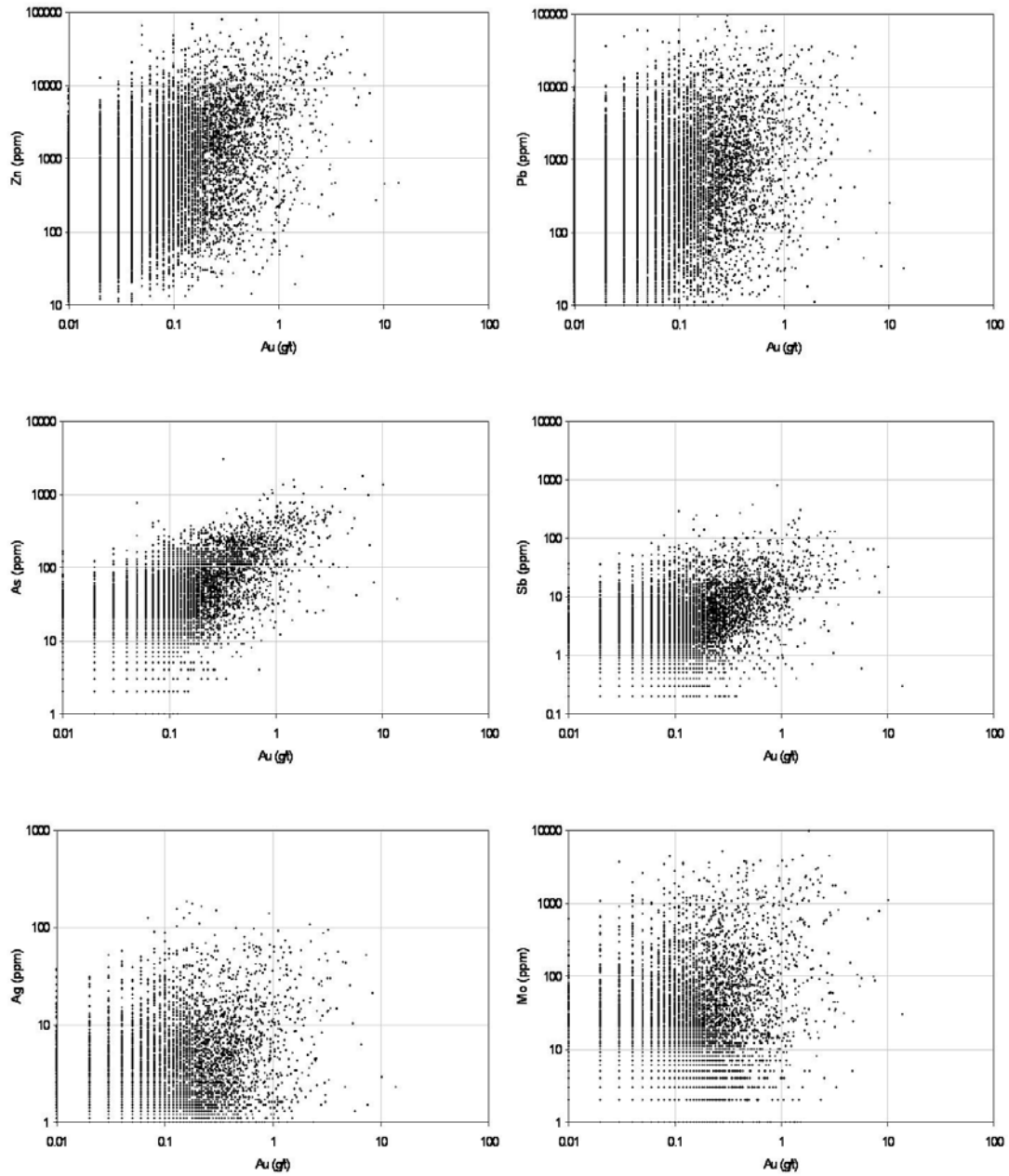


Figure 5-21 Minor element variations of the low-Cu ore sample population with respect to gold
This sample population is derived from the samples that are below 0.1%Cu. The data shows that there are no significant relationships with other metals although As and Sb do form roughly coherent trends with Au.

Table 5-2 Average metal concentrations in assay intervals classified by copper species present

	Total N=26940	High-Cu N=14698	Low-Cu N=3744	Cpy N=5975	Cov N=3177
Cu (%)	0.52	0.94	0.02	1.16	0.93
Au	0.49	0.79	0.35	0.98	0.55
Ag	5.0	6.4	6.55	4.4	5.2
Zn	2,139	2,591	3,464	1,441	902
Pb	1,208	1,106	2,591	425	483
As	94.2	136.3	97	62.9	196.7
Mo	128.5	184.4	136.7	166.8	231.0
Bi	11.3	15.3	12.7	8.9	9.1
Co	13.3	22.5	3.1	26.1	19.1
Sb	8.4	11.1	11.0	3.3	19.9
Se	12.1	16.2	14.7	13.0	13.3
Cr	64.4	85.9	44.2	71.7	142.9
Hg	0.10	0.13	0.20	0.06	0.15
Au/Cu	8.24	0.84	37.43	1.04	0.86

	Cu	Au	Ag	Zn	Pb	As	Mo	Bi	Co	Sb	Se	Cr	Hg
Cu	1.00												
Au	0.60	1.00											
Ag	0.15	0.16	1.00										
Zn	-0.01	0.12	0.53	1.00									
Pb	-0.03	0.03	0.68	0.50	1.00								
As	0.17	0.08	0.30	0.14	0.13	1.00							
Mo	0.06	0.06	0.03	0.04	0.01	0.07	1.00						
Bi	0.04	0.10	0.55	0.34	0.21	0.15	0.05	1.00					
Co	0.47	0.38	0.07	0.12	-0.04	0.04	0.06	0.03	1.00				
Sb	0.06	0.02	0.26	0.10	0.15	0.38	0.02	0.07	-0.02	1.00			
Se	0.06	0.10	0.49	0.37	0.35	0.08	0.04	0.53	0.10	0.06	1.00		
Cr	0.01	-0.04	0.01	-0.05	-0.02	0.09	0.05	-0.01	-0.04	0.06	0.00	1.00	
Hg	0.05	0.07	0.45	0.29	0.31	0.36	0.03	0.10	0.00	0.28	0.06	0.05	1.00

Copper > 0.1%

	Cu	Au	Ag	Zn	Pb	As	Mo	Bi	Co	Sb	Se	Cr	Hg
Cu	1.00												
Au	0.18	1.00											
Ag	0.21	0.23	1.00										
Zn	0.27	0.25	0.60	1.00									
Pb	0.18	0.17	0.72	0.76	1.00								
As	0.27	0.55	0.29	0.31	0.22	1.00							
Mo	0.21	0.24	0.06	0.08	0.03	0.27	1.00						
Bi	0.14	0.10	0.29	0.27	0.14	0.12	0.13	1.00					
Co	0.36	0.15	0.03	0.09	0.01	0.16	0.17	0.07	1.00				
Sb	0.20	0.30	0.42	0.37	0.36	0.44	0.11	0.06	0.07	1.00			
Se	0.15	0.13	0.46	0.35	0.43	0.16	0.05	0.39	0.08	0.18	1.00		
Cr	0.26	0.12	0.02	-0.01	0.00	0.13	0.15	0.03	0.19	0.07	0.04	1.00	
Hg	0.10	0.41	0.21	0.27	0.16	0.43	0.12	0.04	0.06	0.40	0.09	0.08	1.00

Copper < 0.1%

	Cu	Au	Ag	Zn	Pb	As	Mo	Bi	Co	Sb	Se	Cr	Hg
Cu	1.00												
Au	0.68	1.00											
Ag	0.32	0.30	1.00										
Zn	0.02	0.10	0.39	1.00									
Pb	0.00	0.04	0.56	0.48	1.00								
As	0.11	0.11	0.30	0.20	0.24	1.00							
Mo	0.07	0.04	0.03	0.04	0.00	0.08	1.00						
Bi	0.05	0.09	0.32	0.24	0.17	0.10	0.04	1.00					
Co	0.50	0.40	0.22	0.19	-0.02	0.09	0.05	0.03	1.00				
Sb	0.02	0.02	0.31	0.16	0.25	0.25	0.00	0.05	-0.01	1.00			
Se	0.22	0.23	0.42	0.41	0.51	0.16	0.05	0.52	0.27	0.07	1.00		
Cr	0.01	0.01	0.05	-0.02	0.03	0.08	0.02	0.00	-0.06	0.08	0.00	1.00	
Hg	0.03	0.05	0.49	0.34	0.54	0.33	0.02	0.09	0.03	0.34	0.18	0.08	1.00

Chalcopyrite > 1%

	Cu	Au	Ag	Zn	Pb	As	Mo	Bi	Co	Sb	Se	Cr	Hg
Cu	1.00												
Au	0.59	1.00											
Ag	0.33	0.29	1.00										
Zn	0.08	0.19	0.55	1.00									
Pb	0.04	0.10	0.60	0.65	1.00								
As	0.25	0.14	0.43	0.14	0.13	1.00							
Mo	0.12	0.11	0.02	0.02	0.02	0.06	1.00						
Bi	0.18	0.25	0.57	0.50	0.42	0.21	0.02	1.00					
Co	0.43	0.41	0.13	0.12	0.01	0.08	0.09	0.12	1.00				
Sb	0.14	0.06	0.46	0.09	0.08	0.55	0.01	0.18	0.00	1.00			
Se	0.41	0.46	0.37	0.35	0.19	0.18	0.08	0.38	0.55	0.08	1.00		
Cr	-0.08	-0.04	-0.04	-0.06	-0.04	0.01	-0.02	-0.05	0.03	0.00	-0.01	1.00	
Hg	0.19	0.14	0.50	0.26	0.27	0.56	0.06	0.23	0.09	0.57	0.16	-0.01	1.00

Covellite > 1%

Figure 5-22 Correlation coefficients for significant sample populations in Kucing Liar

The chalcopyrite and covellite >1% groups are a subdivision the >1% copper group. Different colours are used to identify individual associations. Red-orange is used to identify copper correlations, blue-cyan are used to identify Pb-Zn associations, and yellow is used to highlight arsenic correlations.

5.2 INTERPRETATION OF METAL ASSAY DATA

The discussion will be divided into two parts, the first will be concerned with interpreting the data supplied in the chapter, in terms of mineralisation packages and the sequence of events. The second section will examine models for processes of metal precipitation from a hydrothermal fluid in light of metal associations found at Kucing Liar.

5.2.1 Defining the mineralisation process through metal associations

The first part of the discussion of results is a summary of the mineralised ore packages, their metal assemblages, and the relationships between them. In some instances, data from this chapter are integrated with the mineral assemblage relationships from Chapter 3 as well as the mineral assemblage distributions from Chapter 5. The assay data provide further definition of the mineralisation process. The differences and similarities between copper mineralisation forms as well as the partitioning of gold between individual ore packages are of particular interest. Kucing Liar mineralisation is dominated by copper and is accompanied by economic gold concentrations. Copper and gold are closely associated with each other and form a core zone that is hosted within a fault jog and along specific stratigraphic contacts adjacent to the fault. Presumably, metal-carrying fluids were channelled into the Idenberg Fault Zone and migrated to complex intersections of fault elements with pre-existing heterogeneities created by a transition from massive sandstone to thinly bedded limestone. Around this Cu-Au core is a zoned complex of Ag-Pb-Zn though in subeconomic concentrations. Small concentrations of Au outside the main zoned system are associated with As-Sb, which appear to be associated with pyrite and base metal (Zn-Pb) mineralisation.

Styles of mineralisation

Ore deposition in the two copper sulphide-bearing assemblages have similar primary metal associations of Cu-Au (Zn-Pb) though they have individual trace element associations as chalcopyrite ores have higher concentrations of Au, Zn, and Co, while covellite ores have higher

Mo, As, Sb and Hg average concentrations. There remains no definitive constraint for the temporal relationship between chalcopyrite-bearing and covellite-bearing ores. The shape of the 1% Cu contour is not related to the individual distributions of chalcopyrite or covellite (Figure 5-23). Gold appears to have three separate associations. It is associated with chalcopyrite and Cu in the lower elevations, but is then strongly associated with pyrite and As before passing to a Au-As-Sb association at the top of the deposit where it is associated with highest Ag-Pb-Zn-(Bi) mineralisation (Figure 5-13 and Figure 5-14), though the association is not strong (Figure 5-21 and Figure 5-22). There is a strong spatial association between covellite and arsenic as well as pyrite and arsenic. Arsenic-rich covellite mineralisation may result from the inclusion of enargite, which is known to occur with covellite (Chapter 3). Arsenic-rich pyrite forms from substitution of As into the crystal lattice of pyrite, which increases its capacity to carry Au (Reich *et al.*, 2005). Due to the time-consuming requirements of the existing research program, no detailed microchemical study of sulphides was performed in this research in order to comprehensively characterise the occurrence of gold (this would make a particularly enlightening study for future researchers). It is expected that gold occurs as inclusions within chalcopyrite or pyrite in the lower zone, but may be refractory where hosted in arsenic pyrite in the upper zone and possibly as substitutions of tennantite-tetrahedrite in the topmost zone.

Zoning patterns

The Cu-Au core comprises both chalcopyrite and covellite-bearing mineralisation, where covellite occupies a central location within the major offset of the Idenberg Fault Zone (Figure 5-23). There is a clear structural relationship between chalcopyrite and covellite-bearing rocks. This structural association also extends to pyrite concentrations, which are also associated with the Idenberg Fault Zone offset. Chapter 3 indicated a general temporal progression of sulphide from chalcopyrite to covellite, then pyrite and lastly galena-sphalerite. A chalcopyrite ± pyrite has precipitated Cu-Au-Co, and was accompanied soon after by a spatially distinct covellite ± pyrite package with similar metal assemblage but with a greater proportion of copper. These styles of mineralisation changed to a pyrite-dominant Au-As ± Ag style of mineralisation. This precious

metal package changed downflow (up elevation) to an Au-Sb-As package, which is suspected to be in the form of tennantite-tetrahedrite. A shell of Pb-Zn formed about the pyrite, chalcopyrite and covellite core in the form of galena-sphalerite.

5.2.2 Metal complexes and ore precipitation

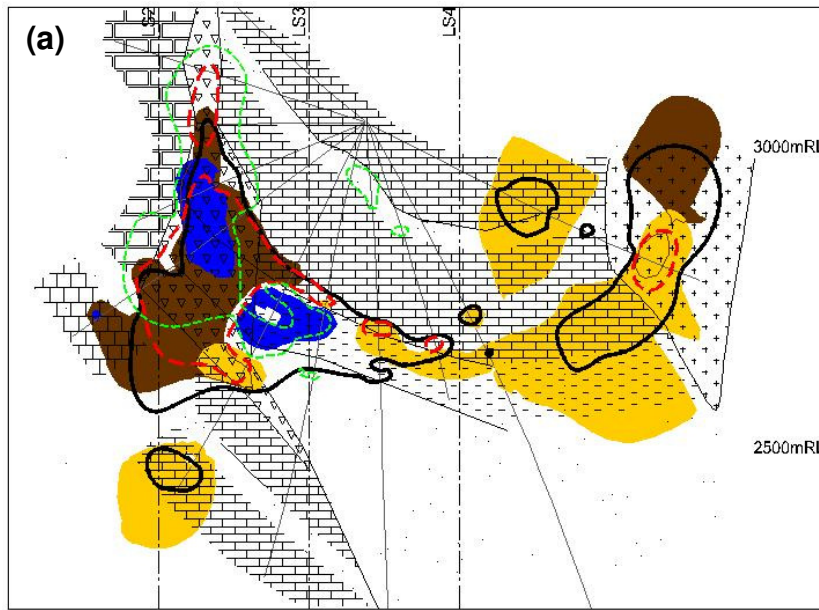
An outward pattern of Cu-Au, and Ag-Zn-Pb may be related to the solubility of these metals in chloride solutions. Published work (Hemley et al., 1992) indicates that at the same temperature, there is a progression of increasing solubility from Fe→Cu→Zn→Pb. The solubility of all of these metals decreases at a steady rate with decreasing temperature. The solubility data neatly predicts the zoning of metal enrichment found at Kucing Liar. This assumes that all metals are carried as a chloride complex and that the solution is saturated with respect to chloride-complexed minerals. It is assumed that gold is carried in an Au-Cl complex although experimental work has suggested that gold may be transported and even sequestered at elevated temperatures and pressures by H₂S ligands rather than chloride (e.g. Loucks and Mavrogenes, 1999). If gold were to be complexed as a bisulphide complex rather than chloride, it would require a different set of changes to the hydrothermal conditions in order for precipitation to take place, as it is known that the factors affecting solubility of Cl-complexes are different, and sometimes opposite to those affecting HS-complexes (Barnes, 1979).

A second form of metal complex is in the form of bisulphide, which may carry Au, As, and Sb in solution (Crerar and Barnes, 1976; Heinrich et al., 1992; Bessinger and Apps, 2003). Some workers have also suggested that Cu is preferentially partitioned into bisulphide solutions, but recent experiments have indicated specific conditions must prevail for bisulphide to be preferred over chloride for copper complexing (Mountain and Seward, 2003). It is significant that Fe is not transported as a bisulphide complex (Crerar and Barnes, 1976) as this implies that the Fe, Cu and possibly Au in the pyrite mineralisation package precipitated from chlorine solutions. Gold is more likely to have been precipitated from bisulphide rather than chloride as experiments by Loucks and Mavrogenes (1999) found that “Au-Cl complexes are not important in pyrite-

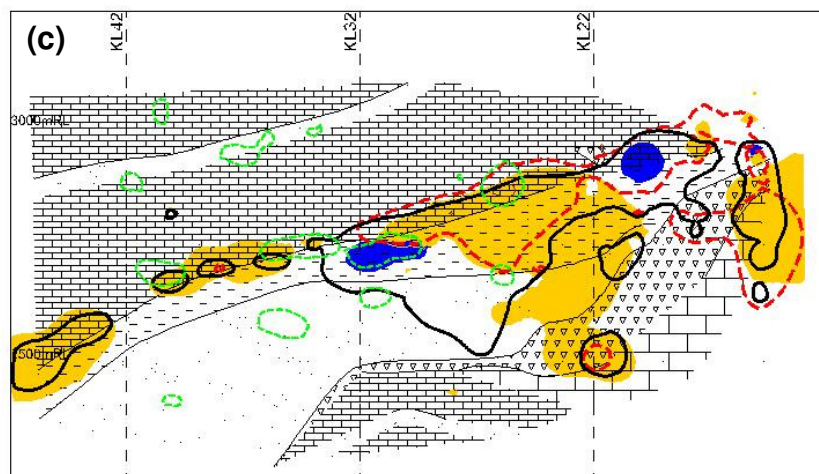
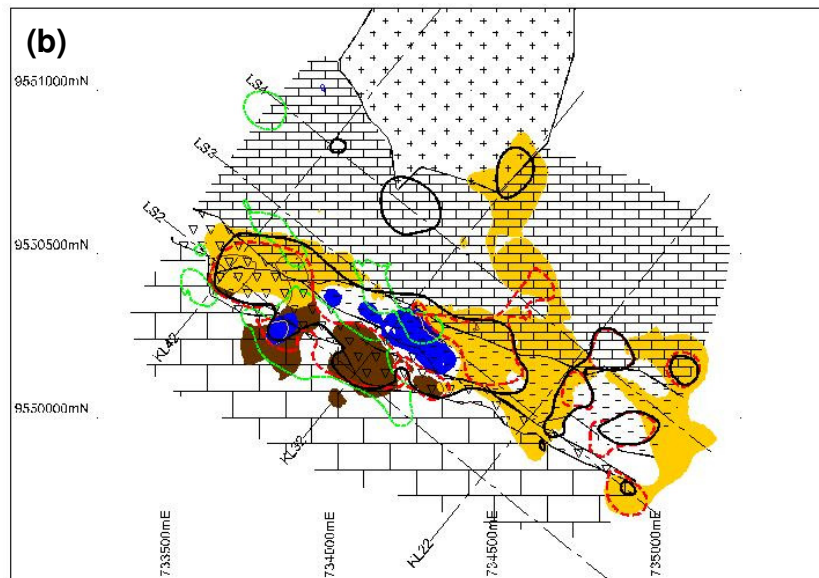
saturated brines”, which these fluids are expected to be given that they have deposited locally abundant pyrite. The change from Cu-Au to precious metals may point to a change in the state of the hydrothermal system as copper transport is more favoured in oxidised conditions whereas gold transport can occur under oxidised or reduced conditions (Rowins, 2000). Finally, the fluids that deposited Au-Sb-As at the upper portions of the base metal zoned system most likely carried the metals as bisulphide complexes (Bessinger and Apps, 2003).

This chapter has shown that the Kucing Liar mineralised zone is a progressively zoned pattern of overlapping base and precious metals. It is presumed that the same fluid has carried the metals from the original source due to the close temporal and spatial relationships of the ore minerals and metal suite. The interpretation provided here implies a change in fluid conditions, from chloride-dominant to bisulphide-dominant, which favours the transport and precipitation of distinct metal assemblages, changing from Cu-Au-Ag-Zn-Pb to Au-As-Sb.

Figure 5-23 Zoning of ore sulphides, pyrite, chalcopyrite and covellite and Cu-Au-As



Comparative cross section (a), plan section (b), and long section (c) showing distributions of ore sulphides and Cu-Au-As. The models indicate an association of chalcopyrite-Cu-Au midway between the IFZ and the GIC, covellite-Cu-As in the Kkel adjacent to the IFZ, as well as pyrite-covellite-Cu-Au-As in the upper sections of the IFZ offset. Some areas of Cu-only appear at the margin of the GIC and are related to low intensity pyrite alteration but no logged Cu-sulphide. An Au-As association, which does not correlate with any modeled sulphides may coincide with galena-sphalerite mineralisation at the highest part of the IFZ in the study area.



- >30% pyrite
- >2% chalcopyrite
- >2% covellite
- >1% Cu
- >1 g/t Au
- >100ppm As

6 Fluid inclusion studies

This section documents the results of fluid inclusion analysis, including thermometric experiments. Fluid inclusion studies yield data relating to the salinity, temperature of mineral formation and, in some cases, the approximate composition of the fluid. Data were collected from a small population of appropriate samples with the aim of identifying fluid populations.

Samples were initially examined petrographically in order to identify key samples as well as the major fluid inclusion types. The distinction between the different types and generations of fluids preserved in Kucing Liar rock samples was resolved by careful microscopic inspection and documentation of the individual inclusion properties as well as the relationships between fluid inclusions. Suitable samples from as many stages of the paragenesis as possible were identified and prepared for inclusion analysis. Cooling and heating experiments were conducted on small wafers of doubly polished thin sections in order to determine the melting temperatures of ice, the melting temperatures of any salt phases present in the inclusions, and the homogenisation temperature of the vapour bubble with the liquid phase of inclusions. Pieces of 3-5mm diameter were broken from doubly polished thin section wafers, suitable inclusions within the chip were identified and a sketch of each visible inclusion in a single field of view was made documenting each inclusion in terms of type and context. The sizes of vapour bubbles relative to the inclusions (degree of fill) were also recorded.

Empirical and theoretical studies of fluid inclusions have identified relationships between thermometric behaviour and fluid composition. The data are converted to salinity and temperature at entrapment by means of published equations. The different types of fluids involved in the development of Kucing Liar alteration and mineralisation can be identified from these data.

6.1 FLUID INCLUSION PETROGRAPHY

6.1.1 Sample location and descriptions

Fluid inclusions have been identified in diopside, andradite, forsterite, humite, quartz, anhydrite and fluorite, however, only quartz and fluorite were found to contain inclusions large enough to study. Samples were preferentially selected from drill station KL32 as drilling from here presents a cross section through the middle of the known strike extent of mineralisation. Some samples were studied from drillholes on other sections due to their particular high quality and abundance of fluid inclusions (Figure 6-1). As quartz is the main host for fluid inclusions, only Groups II and III of the paragenesis were the major foci of the study, although one sample of fluorite represents the Group IV assemblage directly related to mineralisation. The texture, relative timing and spatial relationships of the fluid inclusion host minerals are described below in order of decreasing elevation.

- KL32-1 236.8m – fluid inclusions hosted in idiomorphic crystals from quartz infill in millimetre and centimetre-scale veins (Plate 6-1a, Plate 6-2a). Pyrite, covellite and enargite have infilled vughs along the middle of the veins. It is unclear if the vein is Group II potassic or Group III silica as it is atypical for both stages. The wall rock is intensely altered by quartz, typical of the later silicification assemblage. The sample comes from the Idenberg fault zone and the original lithology and stratigraphical position are unknown.
- KL32-1 254.7m – fluid inclusions hosted by fluorite infill from vughs that are lined with sub-millimetre crystals of Group III quartz (Plate 6-1b, Plate 6-2b). Covellite and pyrite occur as inclusions in fluorite alongside fluid inclusions. Muscovite infill is present within vughs that are lined with Group III quartz. This muscovite has been used as a geochronology sample (see Chapter 3). The sample is from the centre of the Idenberg fault zone and the original lithology is unidentifiable.

-
- KL48-1 100.2m – fluid inclusions hosted by fragments of coarse-grained quartz crystals (Plate 6-1c, Plate 6-2c). The crystal fragments occur in matrix of covellite, chalcocite and pyrite. The quartz is very similar to that in sample KL32-1 236.8m, and both are believed to most likely be coarse varieties from Group III that occur at higher elevations in the system.
 - KL38-5 224.4m – fluid inclusions hosted in a single millimetre-scale quartz crystal as infill in a vugh surrounded by coeval fine-grained Group III quartz alteration that has replaced penetrative diopside alteration in Waripi limestone (Plate 6-1d, Plate 6-2d).
 - KL32-5 339.2m – fluid inclusions hosted in idiomorphic crystals from millimetre-scale Group III quartz veins (Plate 6-1e, Plate 6-2e). The veins are associated with quartz selvedge alteration that has overprinted K-feldspar-muscovite altered Ekmai limestone. Covellite and pyrite have infilled in vughs adjacent to the grains that host fluid inclusions and occur as spots in the fine-grained quartz alteration.
 - KL32-5 376.4m – fluid inclusions are hosted in idiomorphic crystals from a Group II quartz vein (Plate 6-1f, Plate 6-2f). Bornite and chalcopyrite have infilled vughs in the centre of the vein. The veins are hosted in Ekmai limestone that has separate alteration zones comprising magnetite-calcite-chalcopyrite and K-feldspar-biotite-covellite-chalcocite.
 - KL32-3 354.3m – fluid inclusions hosted in subhedral crystals from centimetre-scale quartz veins (Plate 6-1g, Plate 6-2g, also see Plate 6-4). It is not evident whether the veins developed during Group II potassic alteration or Group III silicification, though they appear to be overprinted by Group III grey quartz alteration. Covellite and minor pyrite infill in fractures and vughs crosscut both the quartz vein and wall rock. The host is unclear but believed to be Ekmai limestone.

- KL32-5 706.7m – fluid inclusions hosted in crystals from centimetre-scale quartz veins and in wall rock quartz grains (Plate 6-1h, Plate 6-2h). The veins are either Group II or Group III. Minor covellite and pyrite occur as spots and fracture infill crosscutting both veins and wall rock alteration. The host rock is the upper Waripi sandstone member.

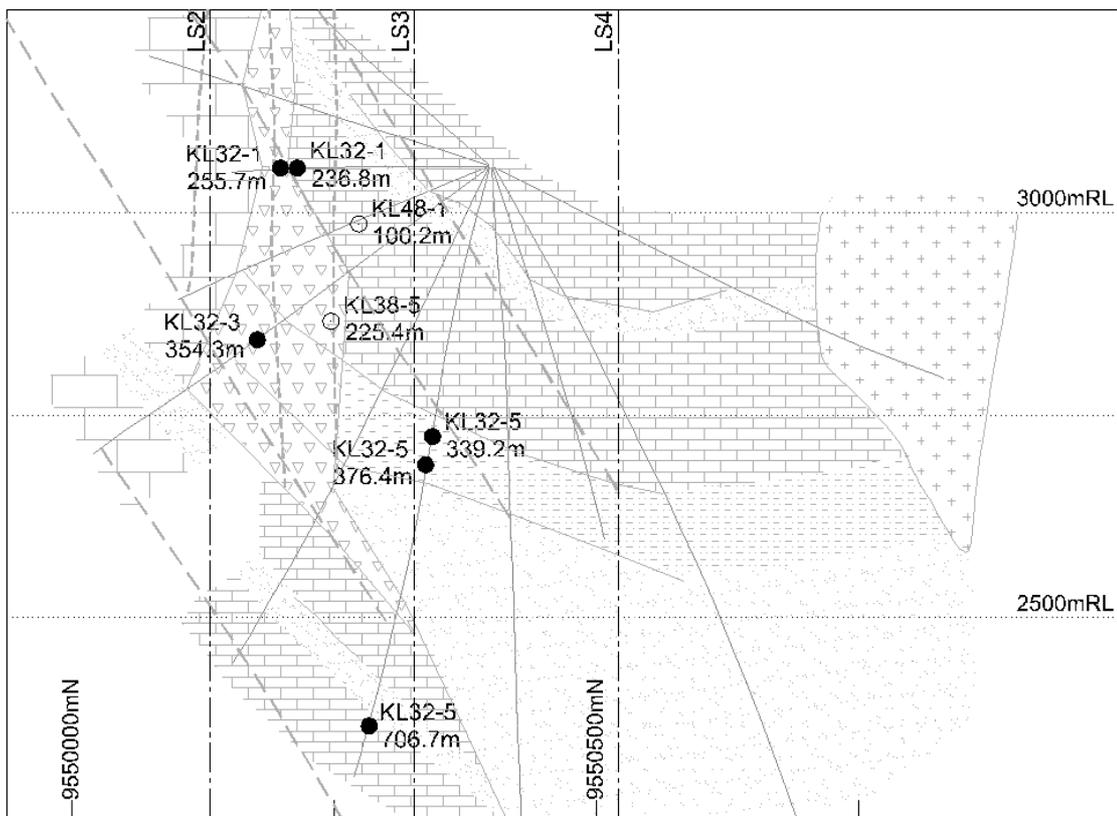
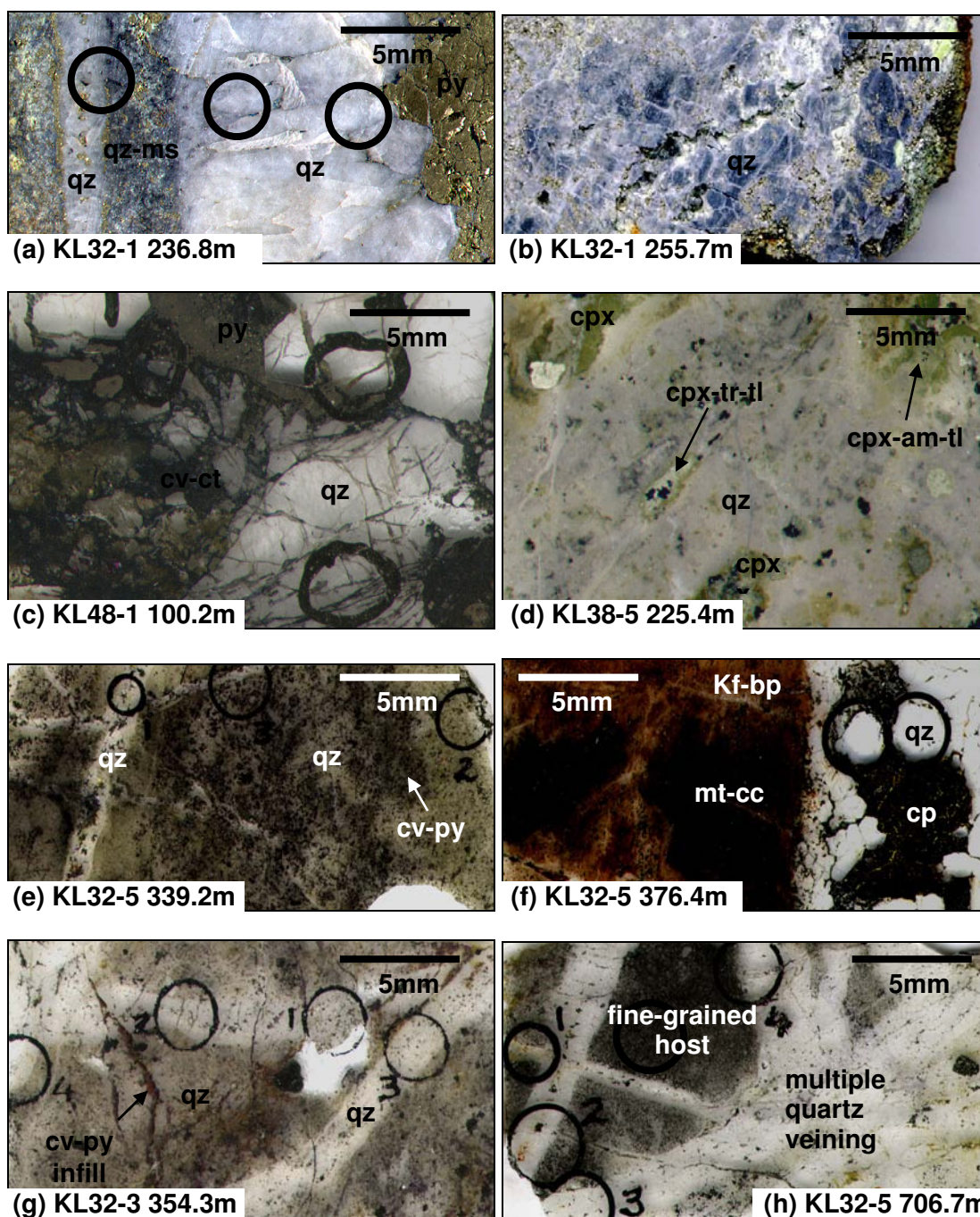


Figure 6-1 Location of fluid inclusion samples

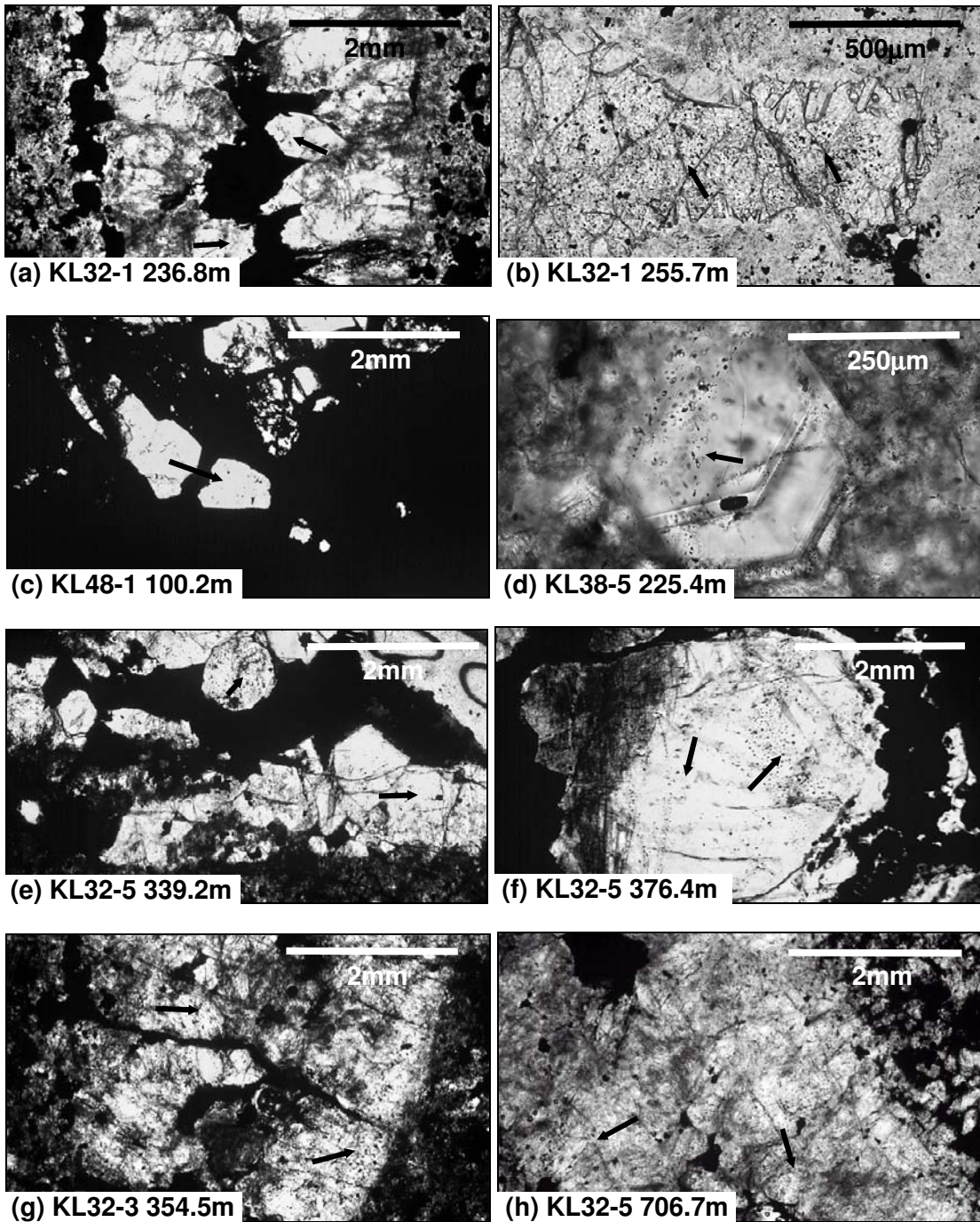
Samples not collected from KL32 drill holes are projected onto section KL32 (see Chapter 3) and marked by an open circle.

Plate 6-1 Photographs of wafers and blocks of fluid inclusion samples



Black circles are drawn around studied fluid inclusion locations. (a) Long quartz crystals protrude into vein centre now filled by coarse pyrite. The quartz is believed to be from Group II and is affected by later quartz-muscovite alteration (b) Fine-grained quartz alteration containing vugs infilled by fluorite and muscovite. (c) Broken quartz crystals in a matrix of pyrite-covellite-chalcocite. The timing of the vein is unknown (d) Fine grained quartz and talc alteration of diopside. (e) Millimetre-scale quartz veins and associated alteration selvages associated with muscovite replacement of feldspar. (f) Potassic-group quartz vein containing pyrite-chalcopyrite-bornite infill. The host rock is K-feldspar + biotite alteration. (g) Quartz veins in quartz alteration crosscut by covellite fracture infill. (h) Crosscutting quartz veins in Group III quartz alteration.

Plate 6-2 Photomicrographs of textural settings of crystals that host fluid inclusions



(a) Vein quartz crystals where the host has also been quartz altered host inclusions as crystal growth zones and annealed fractures (b) Fluorite vugh infill lined with quartz crystals in quartz-muscovite altered rock host inclusions as clearly defined trails (c) Fragments of quartz crystals in sulphide matrix contains many large multi-phase inclusions in close proximity to each other (d) A single crystal infilling a vugh in quartz alteration contains inclusions of similar dimension in banded crystal growth (e) Vein quartz crystals adjacent to mineralisation host many different types of inclusions (f) Individual crystal from a quartz vein hosting chalcopyrite-bornite host inclusions in primary growth zones as well as annealed fracture. (g) A variety of fluid inclusion types are hosted in vein quartz crystals in as well as adjacent wall rock alteration. (h) Inclusions are hosted as trails and clusters in quartz stockwork.

6.1.2 Occurrence and paragenesis

There are five principal different types of inclusions distinguishable on the basis of phases present at room temperature. In decreasing order of abundance they are; SLV (solid-liquid-vapour), LV (liquid-vapour), VL (vapour-liquid), V (vapour) and L (liquid) types (Plate 6-3a). SLV inclusions were identified in quartz and diopside only, VL inclusions are only recognised in quartz, and LV inclusions were identified in all minerals containing inclusions. SLV inclusions typically contain a small vapour bubble and at least one solid phase, typically high relief cubic halite commonly accompanied by low relief round sylvite (Plate 6-3b). Hematite is present in some cases as translucent red-coloured chips or idiomorphic hexagonal crystals (Plate 6-1; *cf.* Nash, 1976). SLV inclusions are rounded, equant and six-sided in cross section. The two-phase inclusions that contain only liquid and vapour are designated as either liquid-vapour (LV) or vapour-liquid (VL) type inclusions depending on degree of fill (e.g. Sheppard *et al.*, 1984). Two-phase inclusions (LV and VL) are commonly irregular although significant numbers of VL and LV inclusions are rounded, equant and six-sided in cross section. Idiomorphic inclusions tend to be much smaller than irregular inclusions and of more regular size. SLV inclusions and two-phase inclusions may occur in clusters that display a large range in size. Monophase liquid-only (L) and vapour-only (V) inclusions were not closely scrutinised, as they do not undergo any observable changes during experiments. In one sample (KL32-1 255.7), fluid inclusions were found in close proximity to and seemingly coeval with sulphide inclusions in fluorite including pyrite and covellite.

Fluid inclusions are considered to be primary, pseudosecondary or secondary depending on their mode of occurrence. Primary inclusions form from the same fluid as the surrounding crystal and are recognisable as they commonly are found along planes parallel to the crystal shape (*cf.* Sheppard *et al.*, 1984; Wilkins, 1990). Pseudosecondary inclusions form before the host crystal has annealed so may appear non-parallel to crystal boundaries, but can be distinguished from secondary inclusions as they do not cross crystal boundaries. Secondary inclusions form after the crystal has annealed, implying a separate fluid source to that which the host mineral precipitated

from. Secondary inclusions generally form in distinct fractures which may cross the boundaries between individual host crystals. Fluid inclusions from Kucing Liar samples occur in a variety of settings, including curvilinear trails, random clusters or as isolated inclusions (Plate 6-4). SLV, LV and VL-type inclusions all form trails, though SLV and LV types are the most common. Trails and clusters of SLV and VL inclusions tend to be consistent in size while LV inclusions are more variable. Trails generally comprise a single inclusion type and may be related to growth planes (primary) or visible fractures (secondary) within a crystal (Plate 6-5a, b). SLV inclusions are hosted in regular-shaped voids and tend to be concentrated within the core of crystal shapes and in some examples exhibit layering parallel to crystal boundaries. Clusters of SLV inclusions typically lie in the centre or the apex of quartz crystals (primary or pseudosecondary), whereas the margins of quartz crystals are inclusion free. LV inclusions generally form trails and may be associated with visible fracturing in the crystal, though this is not always the case. The setting of LV inclusions varies from trails constrained within crystal boundaries (pseudosecondary) to less common examples where trails clearly cross crystal boundaries (secondary). LV inclusions are not restricted to fractures and commonly occur as trails that are not continuous across domains within the quartz grain (pseudosecondary) (Plate 6-6b). Large VL inclusions are occasionally hosted in regular voids but do not show any real association with location inside a crystal shape, though they do locally form trails. In many cases it was not always possible to establish primary from pseudosecondary or pseudosecondary from secondary, though secondary was commonly easy to distinguish. SLV inclusions in Kucing Liar are generally primary, related to crystal growth while LV inclusions may be either, primary, pseudosecondary or secondary. SLV and VL inclusion trails are both intersected by fractures which host LV inclusions, indicating the LV-type formed after both SLV and VL-type inclusions. Earlier inclusions are commonly destroyed near the intersection. (Plate 6-6a). LV inclusions were found to be both pseudosecondary and secondary while the VL inclusions may be primary, pseudosecondary or secondary (Plate 6-6a). VL inclusions are the most difficult to assess as they have a number of textural settings and commonly occur as randomly distributed populations (Plate 6-4).

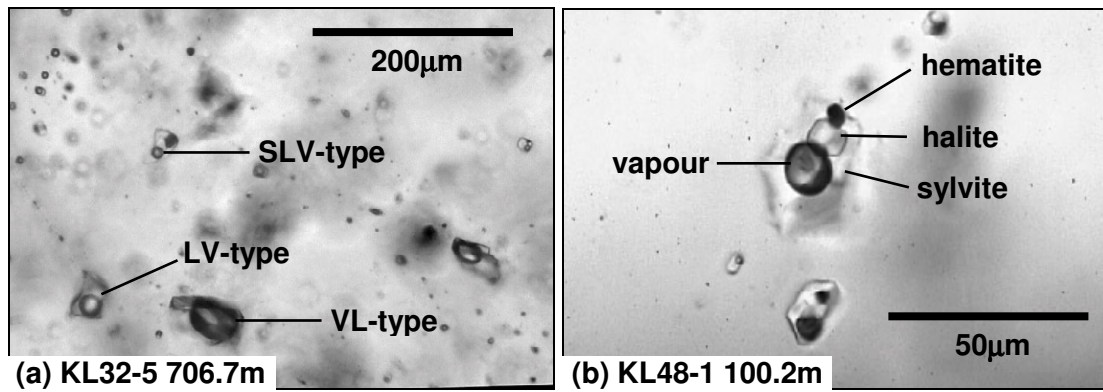


Plate 6-3 Fluid inclusion types in quartz

(a) VL-type inclusions are commonly the largest and occur within irregular or idiomorphic spaces in quartz. LV-type inclusions vary from irregular to regular shapes but are generally not idiomorphic. (b) SLV-type inclusions contain at least one and commonly two salt crystals, a vapour bubble and occasionally, opaque crystals. The low relief of sylvite makes it difficult to observe during melting but the final melt temperature is usually indicated by sudden movement of coexisting phases. Inclusions hosted in quartz.

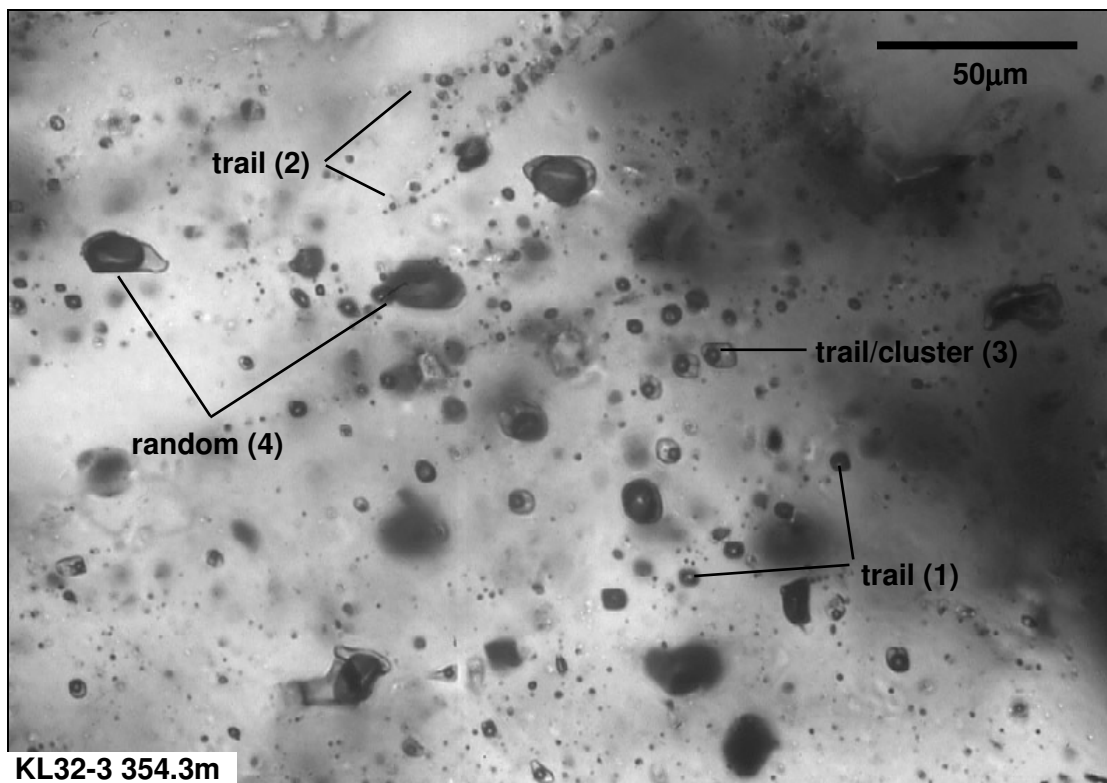


Plate 6-4 Fluid inclusion occurrences in quartz

A photomicrograph of showing possible primary inclusions as trails of uniform-sized VL inclusions (1), pseudosecondary or secondary trails of variable-sized LV inclusions associated with crystal fractures (2), primary or pseudosecondary linear arrays of SLV inclusions (3) and random single VL inclusions that may be primary, pseudosecondary or secondary (4). The parallel nature of SLV and VL trails in examples (1) and (3) suggest formation in a similar setting. While LV trails in (2) are suggestive of overprinting an adjacent VL-type inclusion there are no clear temporal relationships between SLV and VL inclusion trails.

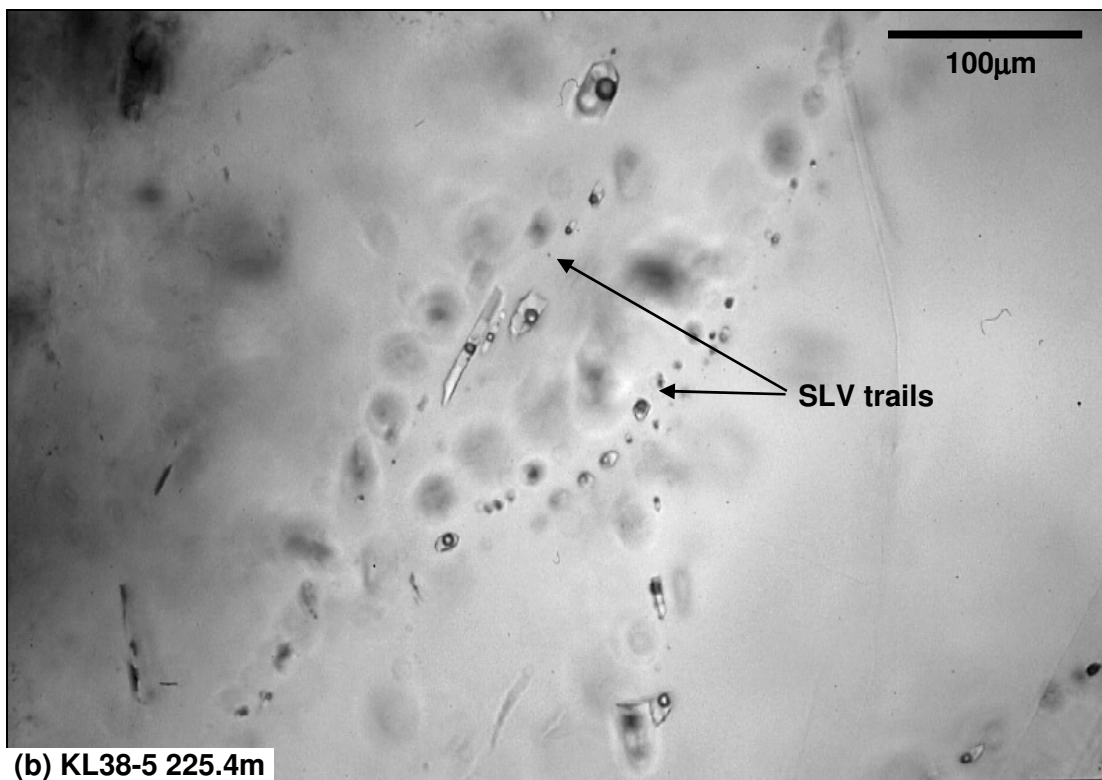
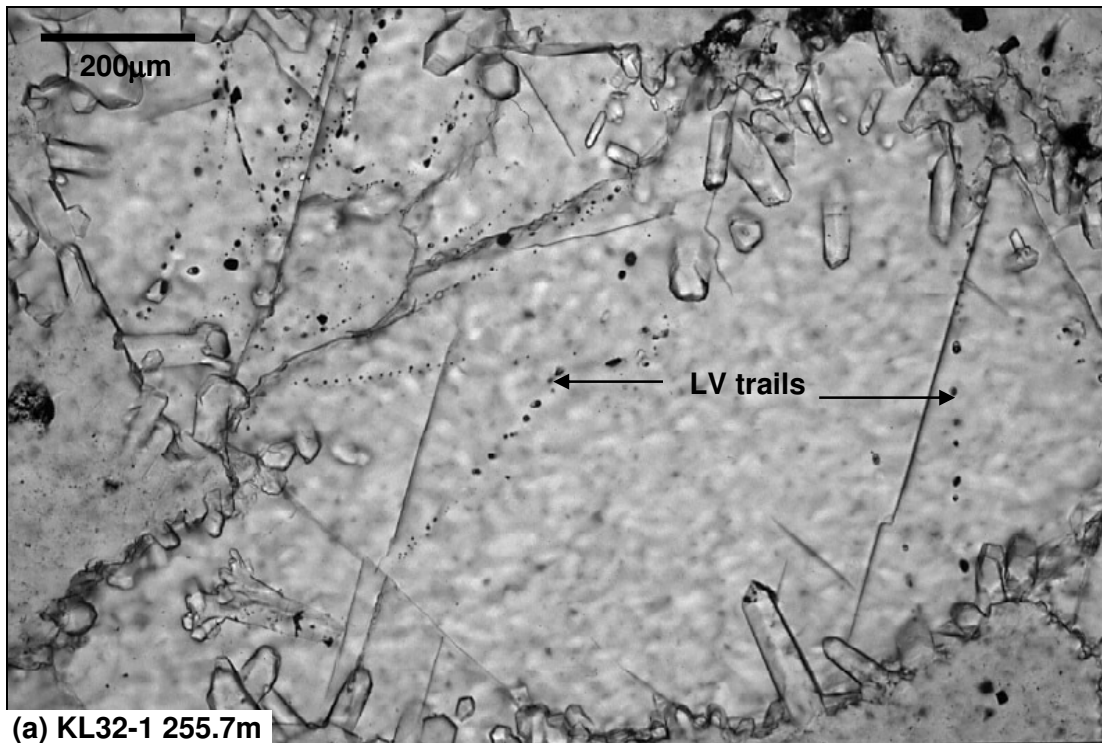


Plate 6-5 Examples of fluid inclusion trails

(a) LV inclusions as single trails across a grain of fluorite. It is unclear if the inclusions are pseudosecondary or secondary. (b) Trails of SLV inclusions in a crystal of quartz. Changing the depth of focus in this sample indicated that single trails form planes through the quartz crystal. The inclusions are considered to be pseudosecondary as they are trapped in curved trails which do not parallel observed crystal faces at low magnification but appear restricted to the quartz grain (see Plate 6-2d).

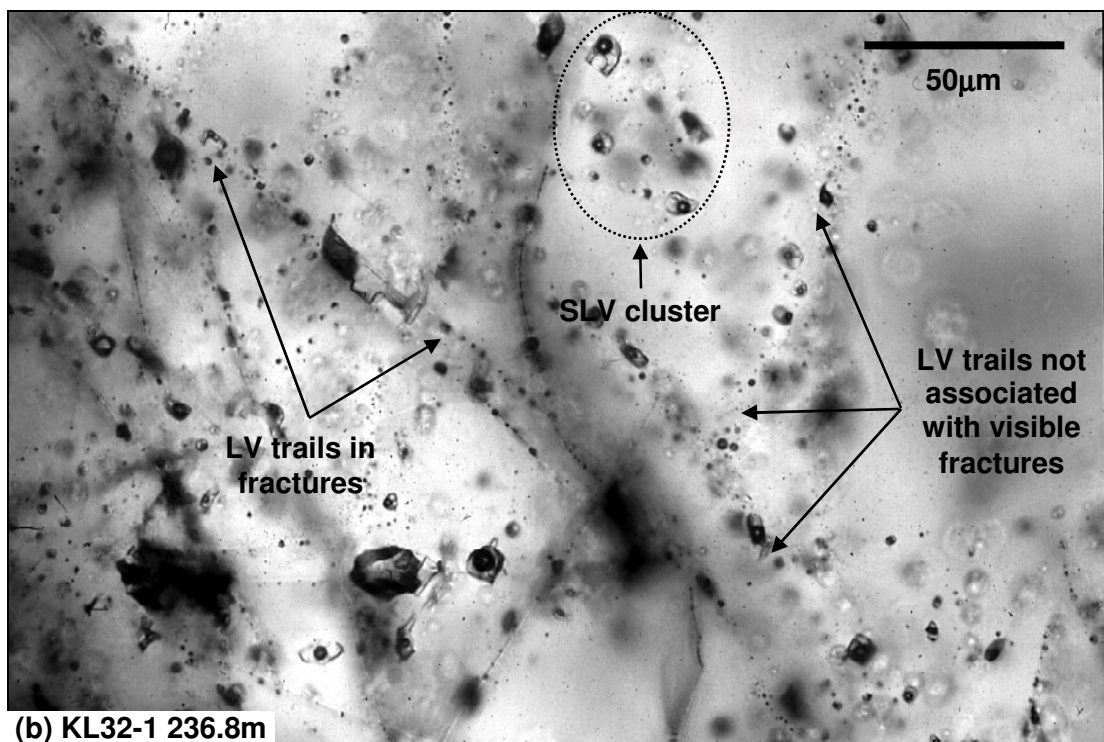
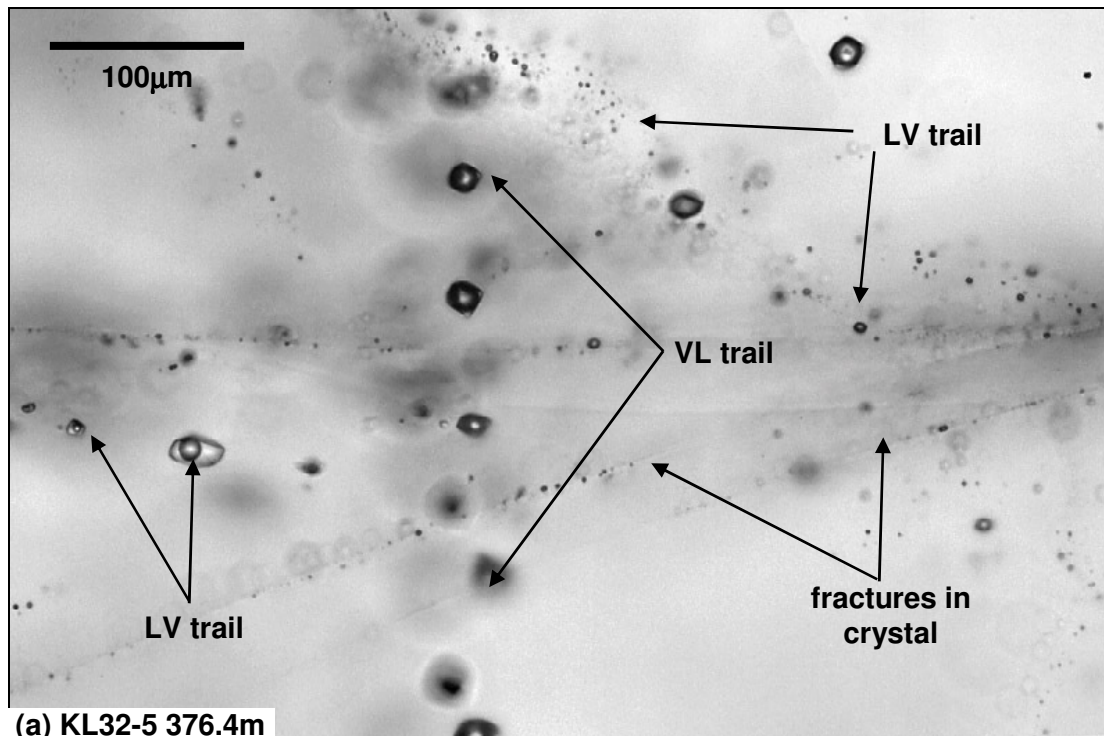


Plate 6-6 Crosscutting fluid inclusion relationships

(a) A trail of LV inclusions that crosscuts trail of VL inclusions in a quartz crystal. The VL inclusions are consistent in size whereas the LV inclusions are highly variable. Both sets of inclusions may represent secondary inclusions, or the earlier VL inclusions may be pseudosecondary. (b) A cluster of variable-sized SLV inclusions (primary or pseudosecondary) is surrounded by variably-sized LV inclusions which are most likely pseudosecondary. Inclusion hosted in clear fractures running top left to centre are either pseudosecondary or secondary and appear to truncate trails of pseudosecondary LV inclusions.

6.2 THERMOMETRIC EXPERIMENTS

The behaviour of the phases within fluid inclusions was observed at 400x magnification and video surveillance in the -200°C to 670°C temperature range (Appendix VI). The chip temperature was monitored to an accuracy of 0.1°C using a slender gauge that also held the chip in place within the sample viewing stage. The temperature of the rock wafer was reduced using gas pumped from a liquid nitrogen vessel and raised by air heated by an electrical element being pumped through the sample stage. The level and rate of heat increase was controlled by a resistance switch. A switch that also cut power to the heating element preserved the temperature at which particular fluid inclusion behaviour was observed. Equipment accuracy of $\pm 2^{\circ}\text{C}$ was established in trial heating experiments on synthetic standards with established homogenisation temperatures of -10.5°C , 190°C & 376.5°C . Freezing experiments were usually conducted prior to heating as a precaution against decrepitation. However, condensation required that apparatus be heated to moderate temperatures ($<250^{\circ}\text{C}$) between multiple freezing behaviour measurements to remove vapour before more freezing experiments could be conducted.

6.2.1 Results of freezing and heating

Various features were investigated including:

- first melting (eutectic temperature) of completely frozen inclusion
- final melting of high relief phases (hydrohalite and antarticite)
- colour and final melting of ice
- final melting of salt phases
- homogenisation of vapour and liquid phases

High relief phase melting, ice melting and vapour-liquid homogenisation temperatures were all difficult to establish for LV-type and VL-type inclusions due to combinations of low visibility and high vapour volumes. Some inclusions hosted in cavities that could not be viewed due to depth of focus were also problematical.

Solid phase melting temperatures

During freezing, 78 of the total 206 inclusions examined turned brown. There were 25 measurements obtained from 14 SLV, 9 LV and 2 VL inclusions for first melting of a non-ice phase, though due to uncertainties in observation and limitations of the equipment the values are only approximate. Thirteen of these eutectic temperatures were measured at or about -52°C , seven between -45 to -49°C , three between -35 to -38°C and two at -26.5°C (Figure 6-2a). In general, SLV inclusions have lower eutectic temperatures than LV and VL inclusions. There were 18 recorded instances where a high relief phase, hydrohalite or antarticite, was identified but only in SLV-type inclusions. The high relief phase hydrohalite was commonly observed to develop in SLV inclusions after first melting but was not consistently identified. Likewise, antarticite, a phase that melts above 0°C , was occasionally recognised in SLV inclusions but not consistently measured. Melting of these high relief phases occurred at different temperatures, which in order of increasing temperature included; nine instances throughout the interval -26 to -34°C , a single instance at -14°C , and six instances between $+10$ and $+50^{\circ}\text{C}$. Distinct populations exist for ice melting (T_{mICE}) observed in LV inclusions. A small group has the lowest (T_{mICE}) between -28 to -24°C and then a steady increase in numbers to a maximum with ice melt temperature between -4 and 0°C (Figure 6-2). The majority of VL inclusions underwent ice melting from -12 to -0°C , and have maxima from -12 and -8°C (Figure 6-2b). Halite (NaCl) melting temperatures were recorded for 71 SLV inclusions, 40 of which also have sylvite (KCl) melting records. Sylvite melt temperatures are generally lower than halite melt temperatures (Figure 6-3a). There is a general correlation of sylvite (T_{mSYLVITE}) and halite (T_{mHALITE}) melting temperatures (Figure 6-3b). The halite melting temperatures are separated into a smaller low temperature (124 - 175°C) and larger high temperature (250 - 450°C) populations (Figure 6-3a). The higher temperature population has an apparent bimodal distribution, the two internal groups distributed symmetrically about maxima at 300 - 325°C and 374 - 400°C (Figure 6-3a).

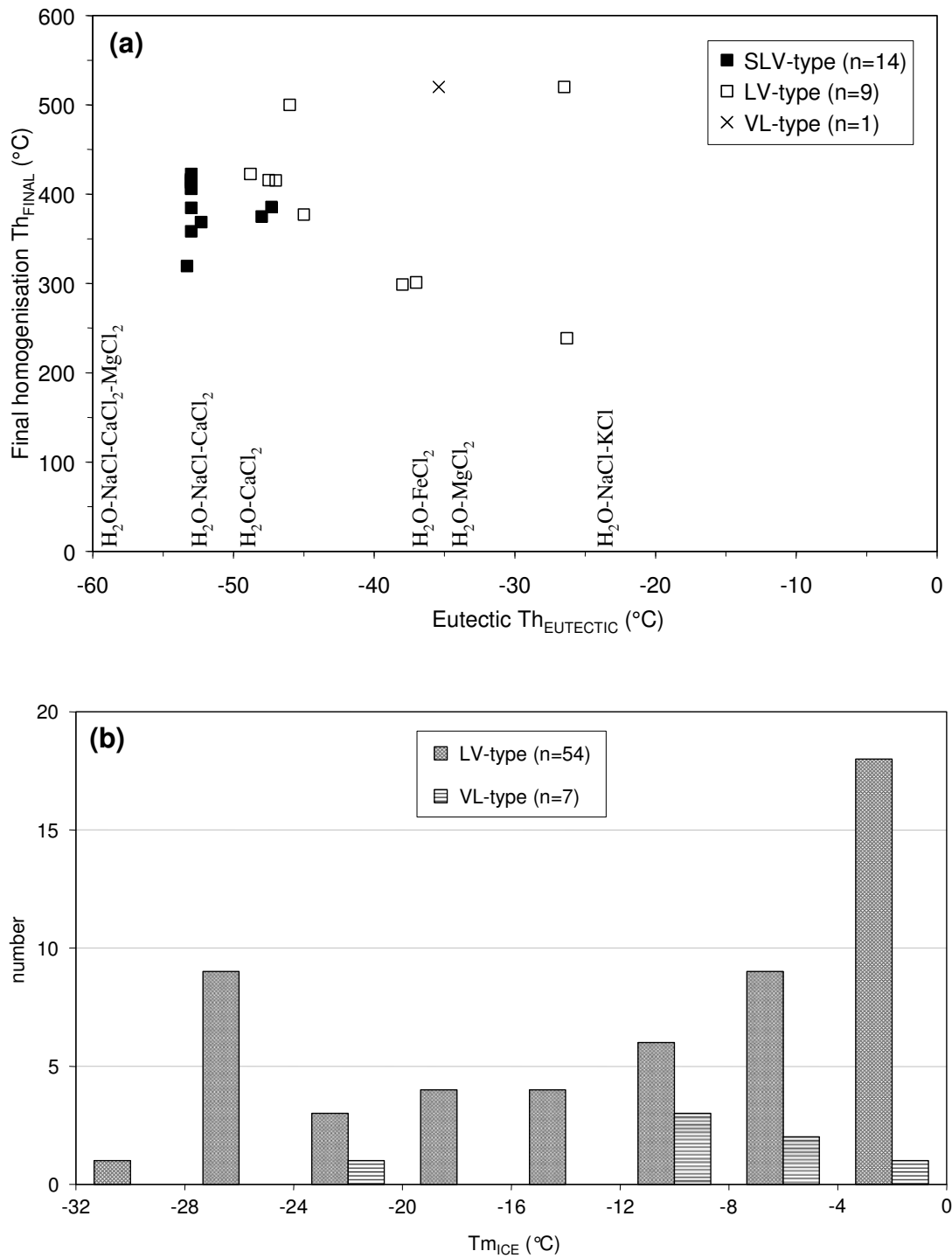


Figure 6-2 First melt (eutectic) and final melting temperatures of ice in frozen inclusions

(a) Eutectic temperatures cluster about $-50^{\circ}C$. These data have uses in determining fluid compositions (see section of fluid compositions). (b) Final ice melting temperatures display a primary maximum near $0^{\circ}C$ as well as a secondary maximum at $-27^{\circ}C$. The bin ranges are plotted along x-axis.

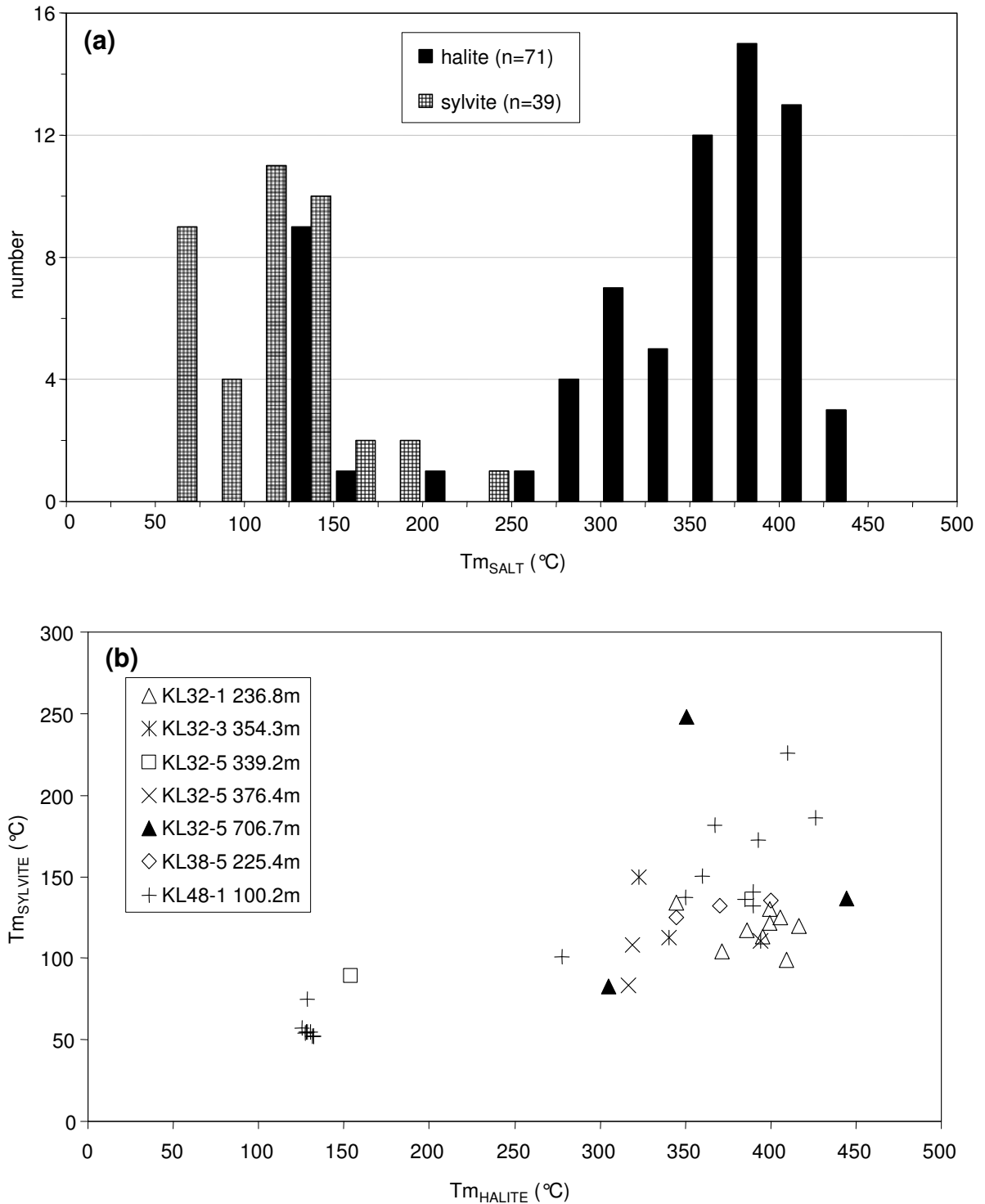


Figure 6-3 Final melting temperatures of halite and sylvite in fluid inclusions

(a) Frequency distribution histogram of halite and sylvite melting temperatures. The data indicate three populations of halite data, one centred on 124-150 °C, a second on 300-325 °C and a third, comprising the most inclusions, centred on 374-400 °C. Bin ranges are 25 °C (b) Relationship between halite and sylvite melting temperatures indicates a broad positive correlation.

Vapour homogenisation

The vapour phase in an inclusion either homogenises ($T_{h_{\text{VAPOUR}}}$) to liquid ($T_{h_{(L-V)L}}$) or vapour ($T_{h_{(L-V)V}}$). In general, vapour-rich inclusions homogenised to vapour and liquid-rich inclusions homogenised to liquid. As with salt melting, homogenisation occurred gradually, the vapour bubble either became smaller, and vibrated more rapidly with increasing temperature until it disappeared completely, or slowly expanded until the entire inclusion became vapour. Vapour homogenisation, whether to liquid or vapour, was recorded in 194 inclusions. There is a broad trend of increasing vapour homogenisation temperatures with decreasing ice-melting temperatures (Figure 6-4a). There are also indications that there may be more than one fluid represented in individual samples (Figure 6-4).

The majority of SLV-type inclusions have halite melting temperatures similar to or greater than $T_{h_{\text{VAPOUR}}}$, while two smaller populations respectively have low and high halite melting temperatures compared with $T_{h_{\text{VAPOUR}}}$ (Figure 6-5). Low halite melting temperatures were observed mainly in a single sample (KL48-2 100.2m), while a group of higher $T_{m_{\text{HALITE}}}$ are derived from inclusions hosted in a number of different samples. Different relationships between halite and vapour occur in cases where $T_{h_{\text{VAPOUR}}}$ and $T_{m_{\text{HALITE}}}$ are similar, as exemplified by KL32-1 236.8m and KL32-5 706.7m. In the former $T_{h_{\text{VAPOUR}}}$ varies over a large range whereas in KL32-5 706.7m $T_{m_{\text{HALITE}}}$ displays the greater variation (Figure 6-4b). In contrast, the small number of inclusions from KL38-5 224-4m display a consistent relationship of $T_{m_{\text{HALITE}}}$ similar to $T_{h_{\text{VAPOUR}}}$ (Figure 6-5).

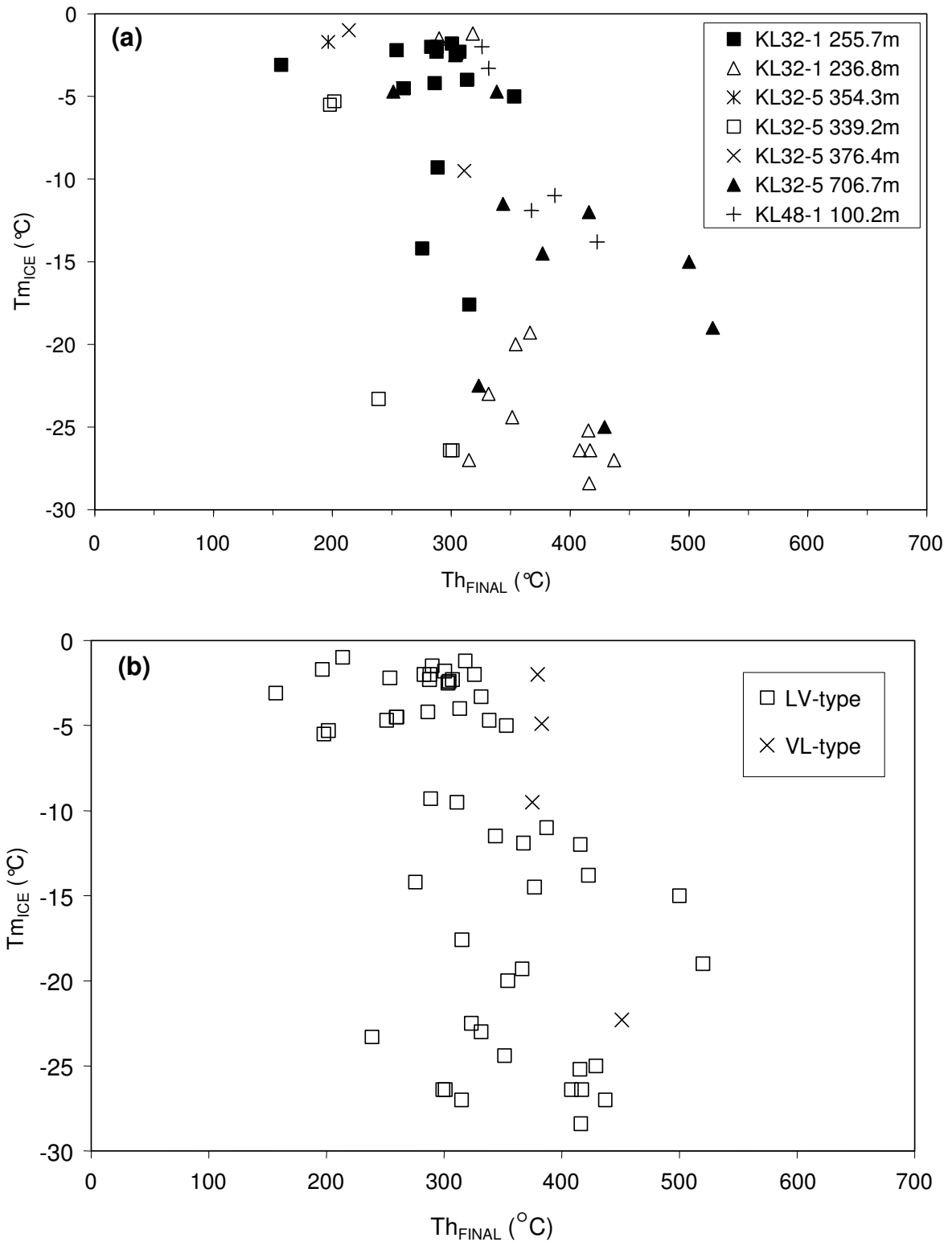


Figure 6-4 Final homogenisation temperature versus ice melting temperatures

(a) The term final homogenisation is used as graph includes LV and VL-type inclusions. A very broad correlation between temperature and ice melting temperature for individual samples is apparent. (b) Only a small number of VL-type inclusions have estimated salinities. LV-type inclusions homogenise to liquid ($T_{h(L-V)L}$), while VL-type inclusions homogenise to vapour ($T_{h(L-V)V}$).

Final homogenisation temperatures (T_{FINAL}), whether to vapour, liquid or salt were recorded in 194 fluid inclusions including 81 SLV, 96 LV and 17 VL inclusions. Final homogenisation temperatures have generally symmetric distributions about discrete maxima (Figure 6-6). Each of these includes different proportions of the three types of inclusions. The low temperature population is represented by LV-type inclusions ($T_{\text{(L-V)L}}$) only and is centred at 174-200°C. The lower of the moderate temperature groups is centred at 300-325°C and dominated by LV-type inclusions ($T_{\text{(L-V)L}}$) but also contains some SLV (T_{VAPOUR} or T_{HALITE}) and VL-type inclusions ($T_{\text{L-V(V)}}$) (Figure 6-6). Conversely, the higher of the moderate temperature groups is centred at 400-425°C dominated by SLV-type inclusions but also contains some LV and VL-type inclusions. The high temperature population include temperatures in excess of 650°C and comprises only VL and SLV-type inclusions. These inclusions had not homogenised at the upper equipment capability limit of 670°C, and so their real homogenisation temperatures may be somewhat higher. These temperatures were mainly derived from SLV inclusions and a single VL inclusion in sample KL32-5 376.4m as well as a single SLV inclusion from KL32-1 236.8m. The inclusions in sample KL32-5 376.4m were of similar appearance (shape, size) and grouped together in trails within an overgrowth on a well-defined quartz crystal. As such these very high measurements are not considered to be due to heterogeneous trapping or necking. Harrison (2000) measured homogenisation temperatures with similarly very high values from inclusions sampled from Grasberg.

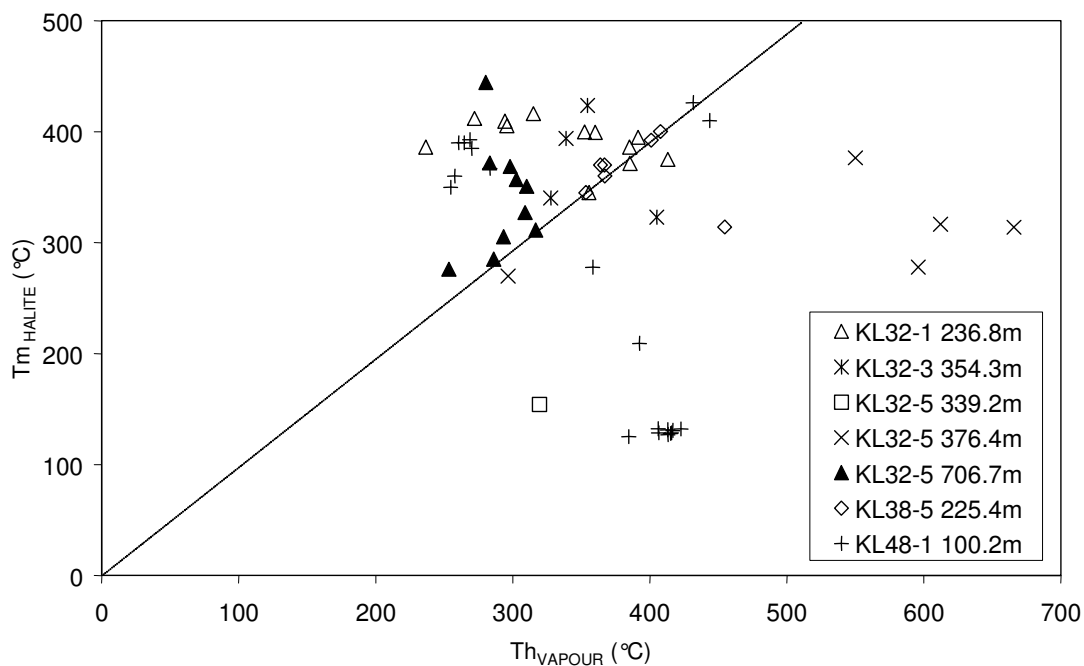


Figure 6-5 Vapour homogenisation versus salt melting temperatures in SLV-type inclusions

A line has been drawn for $Th_{VAPOUR} = Tm_{HALITE}$. It is also apparent that while inclusions from individual samples form clusters, most samples have more than one cluster, possibly indicating the presence of multiple fluids in a single sample

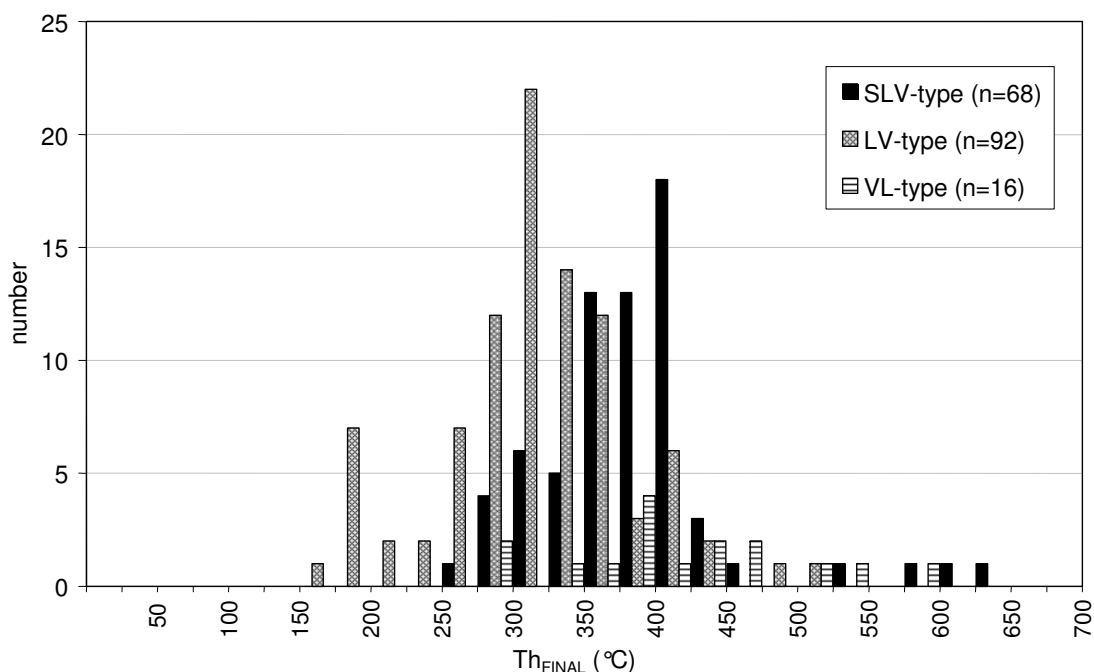


Figure 6-6 Final homogenisation temperatures of fluid inclusions

There were 13 SLV and 5 VL inclusions which did not homogenise at temperatures $< 650^{\circ}\text{C}$. LV-type inclusions homogenise to liquid ($Th_{(L-V)L}$), VL-type inclusions homogenise to vapour ($Th_{(L-V)V}$), while SLV-type inclusions homogenise to liquid either by salt (Tm_{HALITE}) or vapour (Th_{VAPOUR}).

6.2.2 Determination of fluid composition

Salt system

Eutectic temperatures ($T_{m_{EUTECTIC}}$) cluster into groups equivalent to the temperatures for compositions of four different systems. Inclusions with the lowest measured eutectic temperatures have small ranges of $T_{h_{FINAL}}$ but those with higher $T_{m_{EUTECTIC}}$ display a larger range of $T_{h_{FINAL}}$. So, while fluids resembling the systems H_2O -NaCl- $CaCl_2$ and H_2O - $CaCl_2$ have restricted variation of final homogenisation temperatures, those that resemble H_2O - $FeCl_2$ and H_2O -NaCl-KCl systems have a greater range of $T_{h_{FINAL}}$. The change of ice colour to brown is indicative of the presence of calcium as $CaCl_2$ (Brown, 1998). Of the 25 inclusions where a eutectic temperature was measured, 21 were brown ice, suggesting that the fluid inclusions in this group that have H_2O - $FeCl_2$ and H_2O -NaCl-KCl as suggested by $T_{m_{EUTECTIC}}$ also contained $CaCl_2$. The presence of hematite as solid phases in inclusions indicates the presence of abundant Fe in some fluids. Based on the solid phases present in inclusions and melting temperatures of ice, compositions of fluids are most likely to be in the system H_2O -NaCl ($\pm KCl \pm FeCl_2 \pm CaCl_2$) (Table 6-1). SLV inclusions generally resemble the system H_2O -NaCl-KCl- $CaCl_2$ while LV inclusions are H_2O -NaCl- $CaCl_2$.

Table 6-1 First melt temperatures of selected water-salt systems

System	Eutectic ($^{\circ}C$)
H_2O -NaCl- $CaCl_2$ - $MgCl_2$	-57
H_2O -NaCl- $CaCl_2$	-52
H_2O - $CaCl_2$	-49.5
H_2O - $FeCl_2$	-35
H_2O - $MgCl_2$	-33.6
H_2O -NaCl-KCl	-23
H_2O -NaCl	-21.2
H_2O -KCl	-10.6

Data reproduced from various sources compiled by Brown (1998).

Salinity calculations

NaCl equivalent fluid inclusion salinities have been calculated from (e.g. Brown, 1998).

$$\text{LV- and VL} \quad (-1.78 * T_m) - (0.0442 * T_m^2) - (0.000557 * T_m^3)$$

$$\text{SLV} \quad 26.242 + (0.4928 * T_d) + (1.42 * T_d^2) - (0.223 * T_d^3) + (0.04129 * T_d^4) + \\ (0.006295 * T_d^5) - (0.001967 * T_d^6) + (0.00011112 * T_d^7)$$

Where T_m = melting temperature of ice and T_d = (halite dissolution temperature) /100. Fluid inclusions from individual samples cluster in terms of their temperature-salinity relationships (Figure 6-7). High salinity inclusions include moderate (250-450°C) and high temperature groups (>600°C). Low salinity inclusions generally have lower T_{FINAL} .

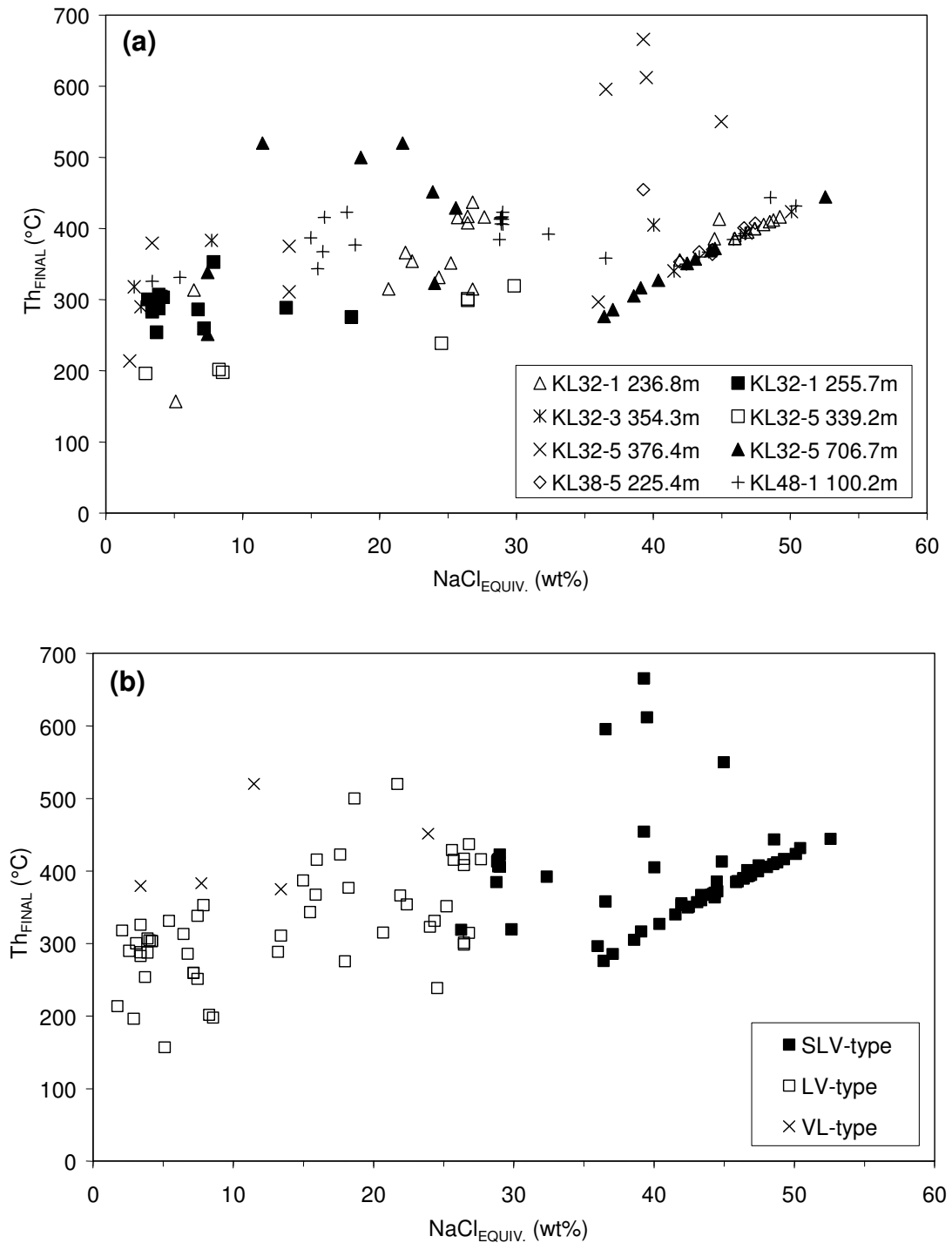


Figure 6-7 Homogenisation temperature versus calculated salinities of fluid inclusions

(a) Results plotted using subdivision by sample. All inclusions are hosted within quartz except for those in sample KL32-1 254-7m which are hosted in fluorite. The linear trend exhibited by the high salinity, moderate temperature group is an artefact of the salinity calculation, and represents inclusions that homogenise by halite dissolution. (b) The same salinity measurements divided by inclusions type (LV, VL and SLV). The term Th_{FINAL} is used as LV-type inclusions homogenise to liquid ($Th_{(L-V)L}$), VL-type inclusions homogenise to vapour ($Th_{(L-V)V}$), while SLV-type inclusions homogenise to liquid either by salt (Tm_{HALITE}) or vapour (Th_{VAPOUR}).

6.3 INTERPRETATION OF FLUID INCLUSION DATA

Experimental data from fluid inclusion analysis indicate that a variety of fluids were involved in the Kucing Liar hydrothermal evolution. The fluids show a distinct populations of high temperature, high salinity brines, more moderate temperatures brines, medium density liquids and finally low density-low salinity water. The last of these is directly related to covellite mineralisation. Low-density phases, characterised as vapour inclusions at room temperature, are found in the same samples and have the same homogenisation temperatures ($T_{h_{V-L(V)}}$) as high and moderate temperature brines ($T_{m_{HALITE}}$ or $T_{h_{VAPOUR}}$). The fluids show little or no graduations between inclusion groupings. The data may suggest temperature shifts and phase changes occurred between the paragenetic stages established in Chapter 3. High temperature fluids are associated with potassic-stage quartz veining while later phyllic-stage quartz alteration host moderate temperature brines (SLV) as well as medium (LV) and low density (VL) phases. While there are no definitive data, many observations point to a phase separation event after silicification which is possibly related to covellite mineralisation.

6.3.1 Fluid populations

Kucing Liar fluids can be divided into discrete populations based on homogenisation temperatures (Figure 6-8a). The data are divided here into four distinct groups; one group (A) having temperatures above 550°C (including many above 670°C), another population at ~420°C (B), a third centred at 300°C (C) and a fourth at 175°C (D). The high temperature group (A) is dominated by brine (SLV) inclusions but also contains a number of vapour (VL) inclusions. The two moderate temperature groups having temperatures around 300°C and ~420°C are more complex and contain variable amounts of all three types of inclusions. Moderate temperature inclusions can be split into two distinct groups based on composition. A higher temperature group at ~420°C (B) is dominated by SLV inclusions while a lower temperature group at ~300°C (C) is dominated by LV inclusions. This second group is associated with covellite mineralisation. The low temperature group (D) is populated by LV-type inclusions only, many of which appeared to

be of secondary origin.

The high and low temperature groups show no real continuity with moderate temperature populations when plotted on a scatter diagram with salinity (Figure 6-7), but there does appear to be a general trend of decreasing temperatures between samples when arranged in a simple plot of inclusion temperatures for each sample (Figure 6-8b). When arranged in this manner it appears that fluids within a single sample exhibit a $\sim 150^{\circ}\text{C}$ temperature range.

6.3.2 Fluid phase development

There are three main types of inclusions found in Kucing Liar samples, namely, SLV (solid-liquid-vapour), LV (liquid-vapour) and VL (vapour-liquid). Hydrothermal fluids derived from magmas may have a range of salinities based on the depth of exsolution (Figure 6-9). Regional and district studies (Chapter 1, Section 1.1.2) of igneous intrusions in the Ertzberg Mining District indicate depth of emplacement as 2km or less. With a pressure of 0.5-1.0 kbar, fluids generated from these magmas will have a salt concentration less than 10 wt.% NaCl (Figure 6-9). Figure 6-9 also indicates that fluids exsolved from magmas up to 1kbar (4km depth) will have gradually increasing salinity after initial water saturation, salinity rising sharply in the last 10% of crystallisation. Note that in much deeper intrusions (2kb \approx 8km), water saturation occurs at a higher crystallisation point and initial fluids have a very high salinity, while later exsolved fluids have sharply decreasing salinity with increasing crystallisation. For a model of a continuously exsolving fluid to produce the observed fluid types at Kucing Liar would require that the earliest fluids have the lowest salinity and the latest fluids have the highest salinity. While stringent primary, pseudosecondary and secondary distinction has not been possible for Kucing Liar fluid inclusions, general convention where SLV-type inclusions are primary or pseudosecondary while LV-type inclusions are pseudosecondary or secondary. This infers that earliest fluids at Kucing Liar are high density and progress to lower density with time. It is also apparent from thermometric data that SLV-type inclusions are higher temperature than LV-type inclusions. This precludes that the Kucing Liar fluids derived from a continuously exsolving shallowly emplaced

magma.

A second process by which fluids of highly variable salinity may occur together locally is by phase separation, perhaps through the processes of rapid decompression which probably occur when magmatic fluids are released into the surrounding environment (Burnham, 1979). IN this process a rising supercritical fluids intersects its solvus (two-phase field) and separates into high and low density fractions (Figure 6-10). The depth at which this phase separation occurs is dependent upon the temperature of the rising fluid and has an effect of the range in salinity of the resultant high and low density phases (Figure 6-10). The contemporary development of a vapour and brine will develop distinctive fluid inclusion assemblages whereby high and low density type inclusion coexist in a single trail and have similar homogenisation temperatures (e.g. Nash, 1976; Sheppard *et al.*, 1984). Studies of Kucing Liar fluid inclusions do not indicate any instances where this boiling assemblage occurs, however, there are brines and vapours co-existing in samples (see Plate 6-4) that do have similar homogenisation temperatures (Figure 6-4 and also Figure 6-8).

A third and final option is that the various fluid populations are developed from different magmas which underwent fluid saturation at different depths (Figure 6-9). For this model to apply at Kucing Liar, late medium density (LV-type), low salinity fluids would have exsolved from a shallowly emplaced magma overprinting fluids from an early more deeply emplaced intrusion which exsolved high salinity fluids. This process is not discounted though no data has been collected to substantiate depth of emplacement of magmas coeval with Kucing Liar hydrothermal fluids.

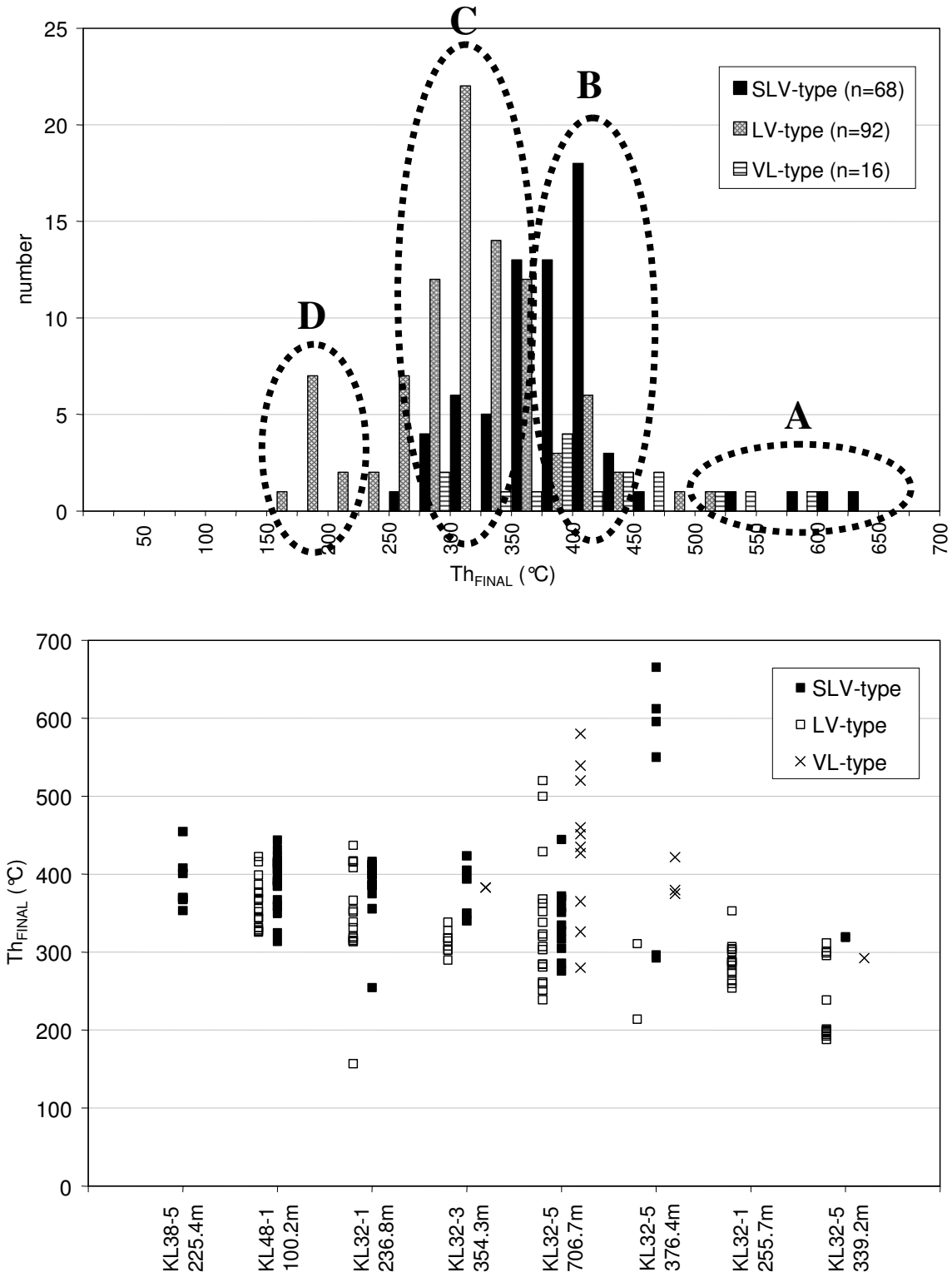


Figure 6-8 Homogenisation temperatures of fluid inclusions

Separation of fluid inclusions into the host samples demonstrates local ranges of homogenisation temperatures. The term Th_{FINAL} is used as LV-type inclusions homogenise to liquid ($Th_{(L-V)L}$), VL-type inclusions homogenise to vapour ($Th_{(L-V)V}$), while SLV-type inclusions homogenise to liquid either by salt (Tm_{HALITE}) or vapour (Th_{VAPOUR}).

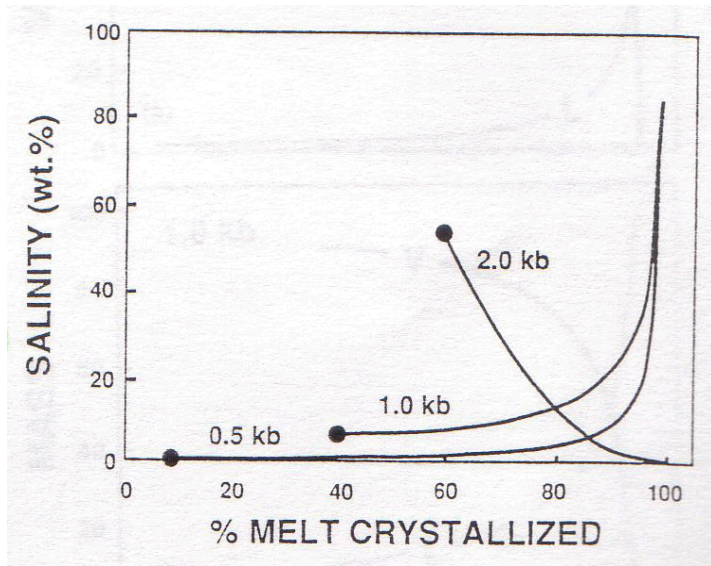


Figure 6-9 Bulk salinity of magmatic fluids exsolved from water saturated magmas

The graph indicates the salinity paths taken by fluid exsolved from magmas at various pressures with increasing crystallisation. The dot represents the point in salinity-crystallisation space at which the magma is saturated with water based on an initial concentration of 2.5 wt.%. Figure reproduced from Cline & Bodnar (1981).

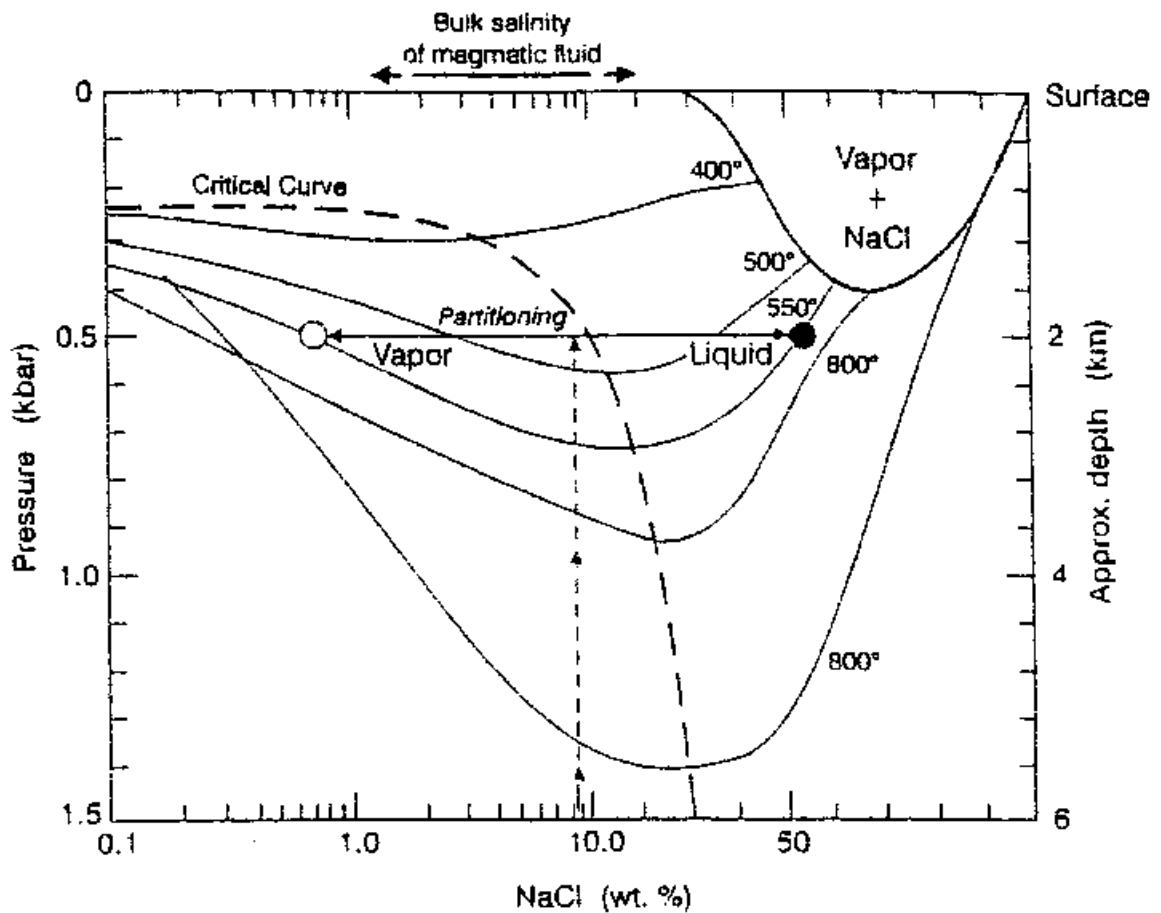


Figure 6-10 Phase separation of critical magmatic fluid (from Meinert, 1998)

The linework indicates that a magmatic fluid of bulk salinity of 8.5wt.%NaCl at 800°C which has cooled to 550°C before ascent can rise to depths equivalent to 0.5kbar before it will undergo separation to high and low density fractions.